ASTROBIOLOGY
Volume 14, Number 2, 2014
© Mary Ann Liebert, Inc.
DOI: 10.1089/ast.2013.1079

Science Applications of a Multispectral Microscopic Imager for the Astrobiological Exploration of Mars

Jorge I. Núñez,[1,*] Jack D. Farmer,[1] R. Glenn Sellar,[2] Gregg A. Swayze,[3] and Diana L. Blaney[2]

Abstract

Future astrobiological missions to Mars are likely to emphasize the use of rovers with *in situ* petrologic capabilities for selecting the best samples at a site for *in situ* analysis with onboard lab instruments or for caching for potential return to Earth. Such observations are central to an understanding of the potential for past habitable conditions at a site and for identifying samples most likely to harbor fossil biosignatures. The Multispectral Microscopic Imager (MMI) provides multispectral reflectance images of geological samples at the microscale, where each image pixel is composed of a visible/shortwave infrared spectrum ranging from 0.46 to 1.73 μm. This spectral range enables the discrimination of a wide variety of rock-forming minerals, especially Fe-bearing phases, and the detection of hydrated minerals. The MMI advances beyond the capabilities of current microimagers on Mars by extending the spectral range into the infrared and increasing the number of spectral bands. The design employs multispectral light-emitting diodes and an uncooled indium gallium arsenide focal plane array to achieve a very low mass and high reliability. To better understand and demonstrate the capabilities of the MMI for future surface missions to Mars, we analyzed samples from Mars-relevant analog environments with the MMI. Results indicate that the MMI images faithfully resolve the fine-scale microtextural features of samples and provide important information to help constrain mineral composition. The use of spectral endmember mapping reveals the distribution of Fe-bearing minerals (including silicates and oxides) with high fidelity, along with the presence of hydrated minerals. MMI-based petrogenetic interpretations compare favorably with laboratory-based analyses, revealing the value of the MMI for future *in situ* rover-mediated astrobiological exploration of Mars. Key Words: Mars—Microscopic imager—Multispectral imaging—Spectroscopy—Habitability—Arm instrument. Astrobiology 14, 132–169.

1. Introduction

An immediate objective in the exploration of Mars is the discovery of past or present habitable environments that could have supported microbial life and provided conditions favorable for the capture and preservation of biosignatures (*e.g.,* Farmer and Des Marais, 1999; National Research Council, 2007, 2011; Des Marais *et al.,* 2008; MEPAG, 2010; Mustard *et al.,* 2013). Imaging at the microscale—in the form of a geologist's hand lens—has long been an essential tool of the field geologist. The microtexture of a rock or soil consists of the microspatial interrelationships between constituent mineral grains, pore spaces, and secondary (authigenic) phases (*e.g.,* cements). In the analysis of aqueously formed sedimentary rocks, which are primary targets for astrobiological exploration, spatially correlated microscale texture and mineralogy are essential data for interpreting the primary formational processes (petrogenesis) of rocks as well as the secondary (diagenetic) processes that have affected a rock after its formation. Such observations are also key for assessing past habitability and the potential of a rock to preserve fossil biosignatures.

Microscopic imaging first entered Mars exploration with the Microscopic Imagers (MIs), flown on the Mars Exploration Rovers (MERs; Herkenhoff *et al.,* 2003, 2004, 2006, 2008). The MI provided black-and-white images, with a field of view of several centimeters, resolved to several tens of microns. Some color information was provided by merging MI images with coarser-resolution color images from the MER Panoramic Camera (Pancam; Bell *et al.,* 2003; Herkenhoff *et al.,* 2004; Weitz *et al.,* 2010). This was followed by the Robotic Arm Camera (RAC; Keller *et al.,*

---

[1] School of Earth and Space Exploration, Arizona State University, Tempe, Arizona.
[2] Jet Propulsion Laboratory, California Institute of Technology, Pasadena, California.
[3] U.S. Geological Survey, Denver, Colorado.
*Present address: Johns Hopkins University Applied Physics Laboratory, Laurel, Maryland.

2008) and the Optical Microscope (OM) within the Microscopy, Electrochemistry, and Conductivity Analyzer (MECA) instrument (Hecht *et al.,* 2008) on board the Phoenix lander (Smith *et al.,* 2008). The RAC and OM instruments provided visible-color imaging through the use of red, green, and blue light-emitting diodes (LEDs), with a CCD focal plane array (Hecht *et al.,* 2008; Keller *et al.,* 2008). This presented the first opportunity for the imaging of soils and small clasts in color at the microscale on Mars. The Mars Hand Lens Imager (MAHLI) on the Mars Science Laboratory (MSL) also provides visible-color imaging at the microscale using an RGB Bayer-pattern filter on a CCD detector (Edgett *et al.,* 2009). White light LEDs provide additional lighting under dark conditions, while long-wave ultraviolet LEDs are used to search for fluorescent materials (Edgett *et al.,* 2009). MAHLI represents the latest state-of-the-art microimagers currently exploring the surface of Mars. These instruments have contributed so much to the success of these missions that microimagers are now recognized as essential tools for Mars surface missions (*e.g.,* National Research Council, 2007; MEPAG ND-SAG, 2008; MEPAG MRR-SAG, 2009; Beaty *et al.,* 2012; Mustard *et al.,* 2013).

This paper provides an overview of the Multispectral Microscopic Imager (MMI), which has been designed to create multispectral, microscale reflectance images of geological samples, where each image pixel is composed of a visible/shortwave infrared (VSWIR) spectrum. This enables the discrimination and microscale mapping of a variety of rock-forming minerals—fundamental data for interpreting the processes that formed the rock. The MMI advances beyond the capabilities of current microimagers on Mars, such as the MER-MI and MSL-MAHLI, by extending the spectral range into the infrared and increasing the number of spectral bands. We employed the MMI to investigate a broad range of well-characterized igneous and sedimentary rock samples that included representative geological materials we expect to encounter on Mars. Particularly well represented in the suite of test samples are lithotypes that record sedimentary processes and environments favorable for the preservation of biosignatures, including vesicular igneous rocks, aqueously altered volcanic materials, detrital and chemical sedimentary rocks, and hydrothermal sinters. At critical stages in the development of the MMI, we used these data sets to evaluate instrument performance. This information was then used to guide improvements to the design. In this paper, the samples were first analyzed with the MMI before being fully characterized by a variety of conventional compositional and mineralogical laboratory techniques to provide a more objective assessment of the performance of the instrument.

The MMI has been developed over several years and realized in a series of breadboard and field instruments of steadily improved capability and technological maturity (Sellar *et al.,* 2006, 2008; Nuñez *et al.,* 2009a, 2009b). A recent model in this series was used to acquire the data sets presented in this paper (see next section). We have been particularly interested in improving the capability of the MMI to map discrete phases, or phase assemblages, at a spatial and spectral resolution useful for defining paragenetic relationships (the relative timing of emplacement of microtextural elements or phases within samples). This allows an assessment of the diagenetic history and how conditions changed over the history of the rock. This approach provides the basis for a more detailed assessment of habitable environments and how they changed over geological history. It also provides a basis for better assessing the potential for preserving fossil biosignatures and for prioritizing samples for analysis with onboard laboratory instruments or for caching samples for potential return to Earth.

2. Instrument Description

2.1. Development of the MMI

The first version of the MMI demonstrated the advantages of multispectral imaging versus panchromatic imaging to bring out subtle color variations in samples, as well as employing isotropic versus heterotropic illumination (*i.e.,* same versus different incident angle of illumination for each band) for reducing spectral artifacts (Sellar *et al.,* 2006). Subsequent versions of the MMI incorporated changes to the camera, such as replacing the CCD with an indium gallium arsenide (InGaAs) focal plane array (FPA), and various improvements to the illumination system, including the addition of LEDs emitting in the shortwave infrared (SWIR; Sellar *et al.,* 2008; Nuñez *et al.,* 2009a, 2009b). These improvements extended the detection range of the MMI from the visible and near-infrared (VNIR) to include the SWIR and increased the number of spectral bands to enable the discrimination and mapping of a wider variety of rock-forming minerals. The system discussed here is field-portable, tripod-mounted, and employs an InGaAs FPA and a 21-channel multiwavelength LED illumination array to generate multispectral, microscale, reflectance images of geological samples, where each pixel of an image consists of a reflectance spectrum ranging from the visible (0.46 μm) to the SWIR (1.73 μm) (Fig. 1). The characteristics of the major components of the instrument are described in the following subsections.

2.2. Camera head and optics

The version of the MMI discussed here uses a commercial infrared camera made by the Goodrich Corporation. (Use of commercial names is for descriptive purposes only and does not imply endorsement by the authors.) The InGaAs detector is sensitive over the spectral range of 0.4–1.8 μm with a quantum efficiency $>65\%$ from 1.0 to 1.6 μm. Unlike standard InGaAs detectors, which are sensitive from 0.9 to 1.7 μm, the MMI FPA range extends to 0.45 μm to enable the imaging of materials in natural color, thus eliminating the need to use two FPAs to cover the VNIR and SWIR. The format of the FPA is 640×512 pixels, with a square-shaped pixel pitch of 25 μm in the image plane.

A custom microimaging lens with a spectral range of 0.4 to 1.8 μm was designed and fabricated specifically for the MMI. The lens was designed with a slow focal ratio (F/10) to provide a $\sim$5 mm depth of field, suitable for imaging natural surfaces (Sellar *et al.,* 2006; Nuñez *et al.,* 2009a, 2009b). The working distance is 63 mm from the front of the lens to the object focal plane, the field of view (FOV) is 40×32 mm, and the spatial sampling is 62.5 μm/pixel in the object plane. This spatial sampling is a tradeoff between the desire to resolve small microtextural features, such as mineral grains of fine sand, versus the need for adequate depth of field and a FOV large enough to allow accurate

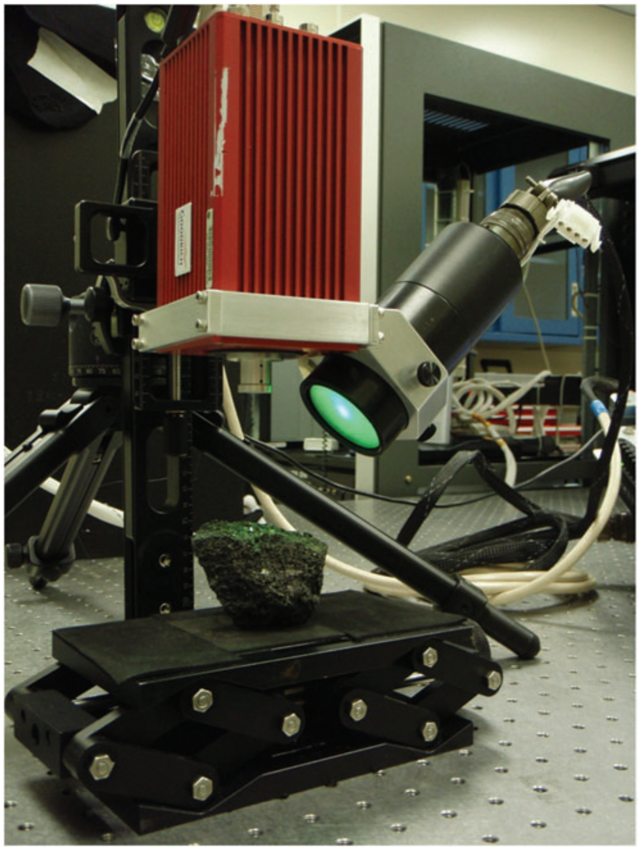

FIG. 1. Image of the Multispectral Microscopic Imager (MMI). MMI shown with field-portable, tripod-mounted, uncooled InGaAs FPA camera (red) and illumination device (black), *i.e.,* illuminator, containing 21-channel multiwavelength LED illumination array. Color images available online at www.liebertonline.com/ast

placement of MMI images within the larger context images obtained by a mast-mounted camera, such as Pancam on MER (Bell *et al.,* 2003). The value and importance of imagery at this scale has been established by the long heritage of hand lens–scale (10–20× magnification) petrologic investigations by field geologists over the last century. Continuing development of the MMI includes improving the spatial sampling from the current 62.5 μm/pixel to $<40\ \mu$m/pixel (see the Future Work section), which reflects an empirically established optimum obtained by imaging microtextures of a wide variety of lithotypes to explore the full range of MMI applications for interpreting petrogenesis in the field.

2.3. Illumination system

The MMI breadboard (Sellar *et al.,* 2006), the RAC (Keller *et al.,* 2008) and MECA Optical Microscope (MECA-OM; Hecht *et al.,* 2008) instruments on board the Mars Phoenix lander mission (Smith *et al.,* 2008), as well as the Rosetta Lander Imaging System (ROLIS; Mottola *et al.,* 2007) on board the Rosetta mission to comet 67P/Churyumov-Gerasimenko, have all demonstrated the capabilities of LED illumination systems in providing color images without the need for a filter wheel mechanism, multiple FPAs, or patterned filters.

TABLE 1. MMI LED BAND CENTERS AND FULL WIDTH AT HALF MAXIMUM (FWHM)

Wavelength center (nm)	*FWHM (nm)*
463	27
522	45
603	19
641	22
667	23
700	25
741	28
756	28
811	32
842	46
884	45
908	63
935	49
970	44
1050	57
1224	63
1290	96
1430	118
1521	145
1660	150
1735	92

The MMI illuminator (Fig. 1) employs commercial-off-the-shelf LEDs to illuminate the sample in 21 different wavelengths, ranging from the visible to the SWIR, that is, 0.46–1.73 μm. Effective spectral band centers and spectral bandwidths (full width at half maximum, FWHM) for this configuration of the MMI are given in Table 1. A plot of normalized MMI LED spectral bands is shown in Fig. 2. The wavelength positions of the LEDs were chosen to target key spectral features (*e.g.,* mineral absorptions) within the MMI wavelength range to maximize differences between different mineral types and enable mineral identification when compared to reference library spectra (See Section 4.2 for more information). By extending the spectral range into the SWIR and increasing the number of spectral bands, this configuration advances the capabilities of the MMI beyond those of previous versions (Sellar *et al.,* 2006, 2008; Nuñez *et al.,* 2009a, 2009b) as well as those of current flight microimagers (see Table 2) and mast-mounted multispectral imagers (see Table 3).

The MMI illuminates the target at an incidence angle of 45° to limit specular reflections and provide topographical information about surface roughness. Experiments with the breadboard in various configurations (Sellar *et al.,* 2006, 2008) and with point microspectrometers (Mouroulis *et al.,* 2008) demonstrated that this configuration (equivalent to ''dark-field illumination'' in transmittance microscopy) minimizes spurious effects of specular reflections and produces spectra that correspond most closely to those sensed remotely by multispectral imagers and imaging spectrometers on aircraft and orbiting spacecraft. While locating LEDs in a ring around the camera lens (referred to in transmittance microscopy as ''bright-field illumination'') may be acceptable for imaging, this arrangement is non-optimal for reflectance spectroscopy. LED wavelengths are activated individually in sequence, as successive images are acquired, thus providing reflectance spectra for every pixel in the FOV.

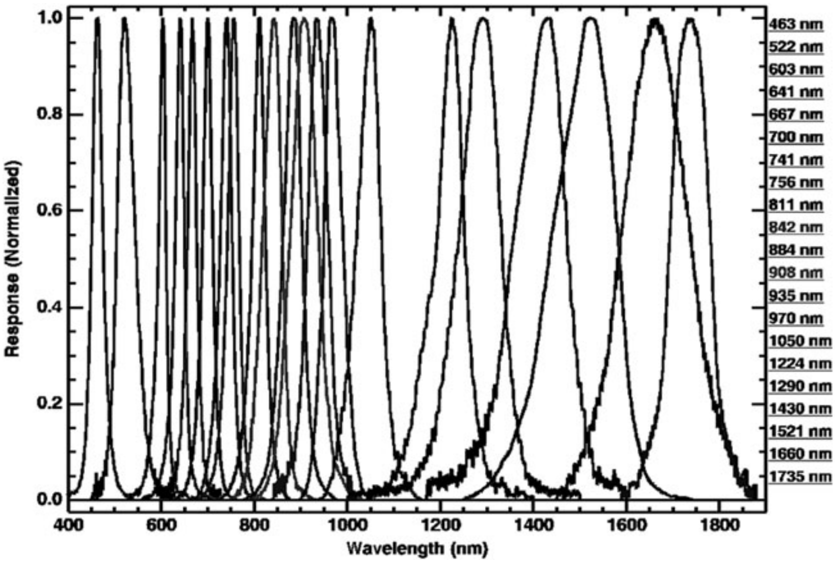

FIG. 2. Plot of normalized MMI LED wavelength distribution profiles. The labels on the right correspond to the effective wavelength center position. Channel center and bandpass values are provided in Table 1. In the rest of the text, the channel wavelength positions are presented in micrometers (μm) instead of nanometers (nm) to be consistent with library spectra.

3. Measurement Protocol and Calibration

3.1. Data acquisition

The MMI acquires a series of background images (*i.e.,* with the LED turned off), along with LED-illuminated images for each wavelength. Multiple frames are acquired and averaged (both for background and illuminated images) to improve the signal-to-noise ratios. The averaged background image is then subtracted from the averaged illuminated image to generate a final background-subtracted image for each wavelength. The procedure is automatically repeated for every wavelength, resulting in 21 separate background-subtracted images. This process lasts less than 2 min.

3.2. Data calibration and generation of image datacubes

Multispectral Microscopic Imager–generated background-subtracted images are obtained from the sample (target) of interest as well as from a National Institute of Standards and Technology (NIST) traceable diffuse Spectralon reflectance standard (by Labsphere, Inc.). Multiple calibrations are acquired with the position of the standard shifted between each calibration, and the results are averaged to remove the effects of microscale non-uniformity of the standard. The data from ''bad'' pixels in the image (*e.g.,* saturated pixels) are replaced with the mean of data from adjacent pixels, weighted by the distance of the nearby pixel to the bad pixel (Herkenhoff *et al.,* 2004). Each background-subtracted image is converted from raw digital numbers to reflectance on a per-pixel basis by dividing the image with the corresponding image of the reflectance standard. Reflectance values are then converted to absolute reflectance by using the manufacturer-supplied spectrum of the reflectance standard. The calibrated images form an image ''datacube'' with a reflectance value for each pixel as a function of two spatial coordinates (row and column) and one spectral coordinate (wavelength). Thus, each pixel has a reflectance spectrum of 21 channels ranging from the visible (0.46 μm) to the SWIR (1.73 μm). Generation of higher-level data products such as band ratios and translated-color images, and endmember maps, are described in Section 4.

4. Methods

4.1. Suite of samples used for test

A suite of igneous and sedimentary rock samples was used to test and validate the performance of the MMI. These samples were selected to provide a broad range of

TABLE 2. COMPARISON OF MMI TO CURRENT MICROSCOPIC IMAGERS

Item	*MER MI*[a]	*Phoenix RAC*[a,b]	*MSL MAHLI*[a,b]	*MMI*
Detector type	CCD	CCD	CCD	InGaAs
Array size (pixels)	1024×1024	512×256	1600×1200	640×512
FOV (mm)	31×31	11.2×5.6 (15.5×7.8)	23.2×17.4 (48×36)	40×32
Depth of field (mm)	3	1.4 (2.3)	0.9 (∼4)	5
Spatial resolution (μm/pixel)	30	23 (30)	14.5 (30)	62.5
Detection range (nm)	400–1000	400–700	400–700	400–1800
Number of bands	2 (includes dust cover)	3	4 (includes UV LED)	21
Illumination	Ambient	LED (RGB)	LED (white)	LED (multispectral)
Color information	Gray scale	RGB	RGB	Multispectral

[a] Sources: Herkenhoff *et al.* (2003), Keller *et al.* (2008), Edgett *et al.* (2009).
[b] Data for highest spatial resolution and same spatial resolution as MER MI in parentheses.

Table 3. Comparison of MMI to Current Multispectral Imagers

Mars Pathfinder IMP[a]		*MER Pancam*[a]		*Phoenix SSI*[a]		*MSL Mastcam*[a]		*MMI*	
λ (nm)	*FWHM*	*λ (nm)*	*FWHM*	*λ (nm)*	*FWHM*	*λ (nm)*	*FWHM*	*λ (nm)*	*FWHM*
		432	32						
445	26	436	37	445	23	445	10	463	27
480	27	482	30	485	23	495	37		
530	30	535	20	533	28	527	7	522	45
						554	38		
600	21	601	17	604	16	590	88	603	19
						640	44	641	22
670	20	673	16	672	18	676	10	667	23
								700	25
750	19	753	20	753	19	751	10	741	28
								756	28
800	21	803	20	802	21	805	10	811	32
								842	46
860	34	864	17	860	36	867	10		
		880	20			880	10	884	45
900	41	904	26	900	44	908	11	908	63
930	27	934	25	932	27	937	11	935	49
970	31			966	31			970	44
1005	29	1009	38	1000	27	1012	21	1050	57
								1224	63
								1290	96
								1430	118
								1521	145
								1660	150
								1735	92

[a] Smith *et al.* (1997, 2001, 2008), Bell *et al.* (2003, 2012), Malin *et al.* (2010).

IMP, Imager for Mars Pathfinder; Pancam, Panoramic Camera; SSI, Surface Stereo Imager; Mastcam, Mast Camera.

microtextural types and grain sizes, with simple to complex mineralogies that typically show spectral features more easily detected over the wavelength range provided by the MMI. Results with these test samples were used to further improve the design and development of the instrument and to maximize scientific return by improving data-interpretation methods. Targets included a set of approximately 15 × 15 mm square subsamples of naturally occurring rocks (*e.g.,* silicates, oxides, carbonates, and evaporites) ground to a surface roughness comparable to that generated by the Rock Abrasion Tool (RAT) on MER (Gorevan *et al.,* 2003). Many of the geological samples showed diagnostic spectral features within the MMI's detection range, while others contained fine-scale microtextures and grain sizes that challenged the MMI's spatial resolution limits. A number of unprepared natural samples were also used to test the MMI's depth of field and capabilities for investigating unprepared surfaces.

Multispectral Microscopic Imager test samples were in large part selected to represent geological materials either known to occur on Mars or that could be reasonably expected to occur there. Over half the study samples are of particular interest for astrobiology in possessing microtextures and aqueous mineral compositions indicative of past habitable environments. An example mosaic of MMI natural-color composite images of some of the rock targets used is shown in Fig. 3.

Samples were also characterized in detail by using a variety of conventional compositional and mineralogical laboratory techniques, including high-resolution visible/infrared spectroscopy, X-ray powder diffraction, and thin section petrography. These characterizations were done following analyses with the MMI and provided validation data for assessing the performance of the MMI in detecting minerals and reliably locating them within a microtextural context. In Section 5, a subset of the MMI test samples is described in more detail to demonstrate the capabilities of the instrument for conducting petrologic investigations.

4.2. Visible to shortwave infrared spectroscopy

To provide an independent assessment of mineralogy and for judging the quality of spectra obtained with the MMI, we used an ASD, Inc., Fieldspec Spectrometer over the wavelength range from 0.35 to 2.5 μm, using a halogen lamp for illumination and Spectralon panel for reference at the U.S. Geological Survey (USGS) Spectroscopy Lab to analyze the samples. The ASD spectrometer has 5 nm spectral resolution from 0.35 to 1.0 μm, 12 nm spectral resolution from 1.0 to 1.8 μm, and 11 nm spectral resolution from 1.8 to 2.5 μm. Wavelength positions are accurate to < 1 nm based on annual ASD, Inc., calibrations independently verified by measurements of well-characterized sharp spectral features in a Corning REE-doped glass, a clear Mylar sheet, and a NIST wavelength standard.

Depending on microtextural diversity, two to four spots representing different regions of interest on the sample surface were analyzed. Each ASD spectrum represents

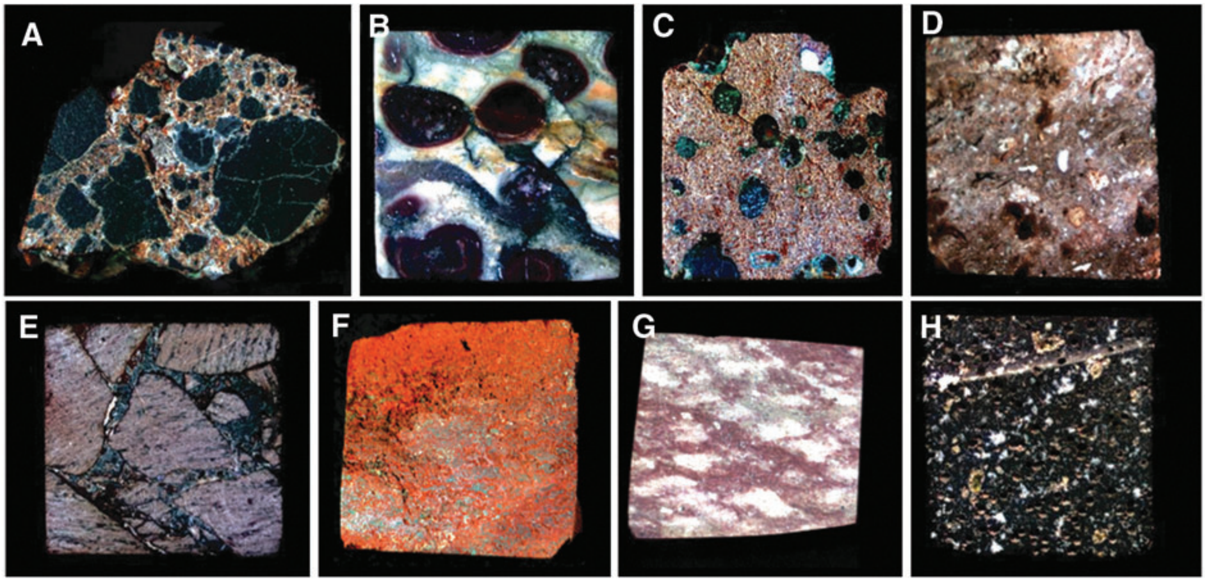

FIG. 3. MMI images of selected sample rock targets used in this study to develop and test the performance of the MMI. The RGB images are composed of bands 641, 522, and 463 nm, respectively, to simulate natural color and are linearly stretched. The rock targets are approximately 15 × 15 mm in size. Samples include (**A**) basaltic volcanic breccia, (**B**) oolitic limestone, (**C**) hydrothermally altered basalt with infilled vesicles, (**D**) siliceous sinter, (**E**) silicic volcanic breccia, (**F**) Fe-rich siliceous sinter, (**G**) gypsum-rich evaporite, (**H**) vesicular basalt. Due to space limitations, a subset of the sample rock targets is highlighted in detail in this report (samples A, E, and H).

integration over a 6 mm diameter spot size. For each spot analyzed, 20 spectra were acquired and averaged. Offsets between the three internal spectrometers were corrected and spectra converted to absolute reflectance by using a modified NIST traceable reflectance spectrum supplied with the Spectralon panel. Corrected spectra were imported into ENVI (Environment for Visualizing Images, a commercial software package sold by Exelis) and compared to spectra from the USGS spectral library (Clark *et al.,* 2007) for mineral identification. Additional spectra from the Keck/NASA Reflectance Experiment Laboratory (RELAB; Pieters and Hiroi, 2004) and NASA/JAXA Advanced Spaceborne Thermal Emission and Reflection Radiometer (ASTER; Baldridge *et al.,* 2009) spectral libraries were used to supplement the USGS spectral library.

Visible/shortwave infrared reflectance spectroscopy is well suited for the detection of a variety of crystalline and amorphous materials and is particularly useful for samples containing amorphous Fe oxides and hydrated phases, which are not easily identified with X-ray diffraction (XRD). Within the range from 0.35 to 2.5 μm, diagnostic absorption features associated with electronic and vibrational processes enable the identification of a wide range of igneous and alteration minerals (Fig. 4). These include mafic igneous minerals (such as olivine and pyroxene; *e.g.,* Hunt and Salisbury, 1970; Adams, 1974; Cloutis *et al.,* 1986; Clark, 1999), metal oxides (such as hematite and goethite; *e.g.,* Sherman *et al.,* 1982; Morris *et al.,* 1985, 1993; Bell *et al.,* 1990; Cornell and Schwertmann, 1996; Clark, 1999; Bell *et al.,* 2000; Morris *et al.,* 2000), hydrated silicates (such as montmorillonite and opal; *e.g.,* Hunt *et al.,* 1973; Clark *et al.,* 1990; Bishop *et al.,* 1994, 2002a, 2002b; Clark, 1999; Cloutis *et al.,* 2002; Swayze *et al.,* 2003; Goryniuk *et al.,* 2004; Milliken *et al.,* 2008) and sulfates (such as gypsum and kieserite; *e.g.,* Hunt *et al.,* 1971; Clark *et al.,* 1990; Clark, 1999; Cloutis *et al.,* 2006), and carbonates (such as calcite and dolomite; *e.g.,* Hunt and Salisbury, 1971; Gaffey, 1987; Clark *et al.,* 1990; Clark, 1999; Swayze *et al.,* 2003).

4.3. X-ray diffraction

X-ray powder diffraction was used to determine the bulk mineralogy of each sample and to assess the accuracy of the spectral analyses. X-ray diffractograms were obtained with a Siemens D-5000 diffractometer with a 7.58° wide position-sensitive detector. The incident beam was Cu-Kα radiation (40 kV, 30 mA), with a 1.0 mm antiscatter slit. A nickel foil was used to limit the beta lines for copper. Powders for bulk analysis were initially crushed and ground in 100% ethanol with an agate mortar and pestle. The dried sample was then passed through a 150 μm mesh sieve. The <150 micron size fraction was mixed with 100% ethanol and precipitated on a zero-background silicon slide. Samples were run over a 2θ range of 5–65°, at 0.02° step intervals and a step time of 2 s. This method was used to increase signal-to-noise ratio and bring out the diffraction peaks of ordered phases above any background generated by amorphous phases, such as volcanic glass, or nanophase Fe oxides, which were present in many of the samples. Major mineral phases were identified with the analytical software, Jade (developed by Materials Data, Inc.), by matching diffractograms to the International Centre for Diffraction Data (ICDD) library database.

4.4. Thin section petrography

Petrographic thin sections were prepared by Spectrum Petrographics, Inc. (Vancouver, WA) by using the matching slab surfaces from each sample. Thin sections were standard

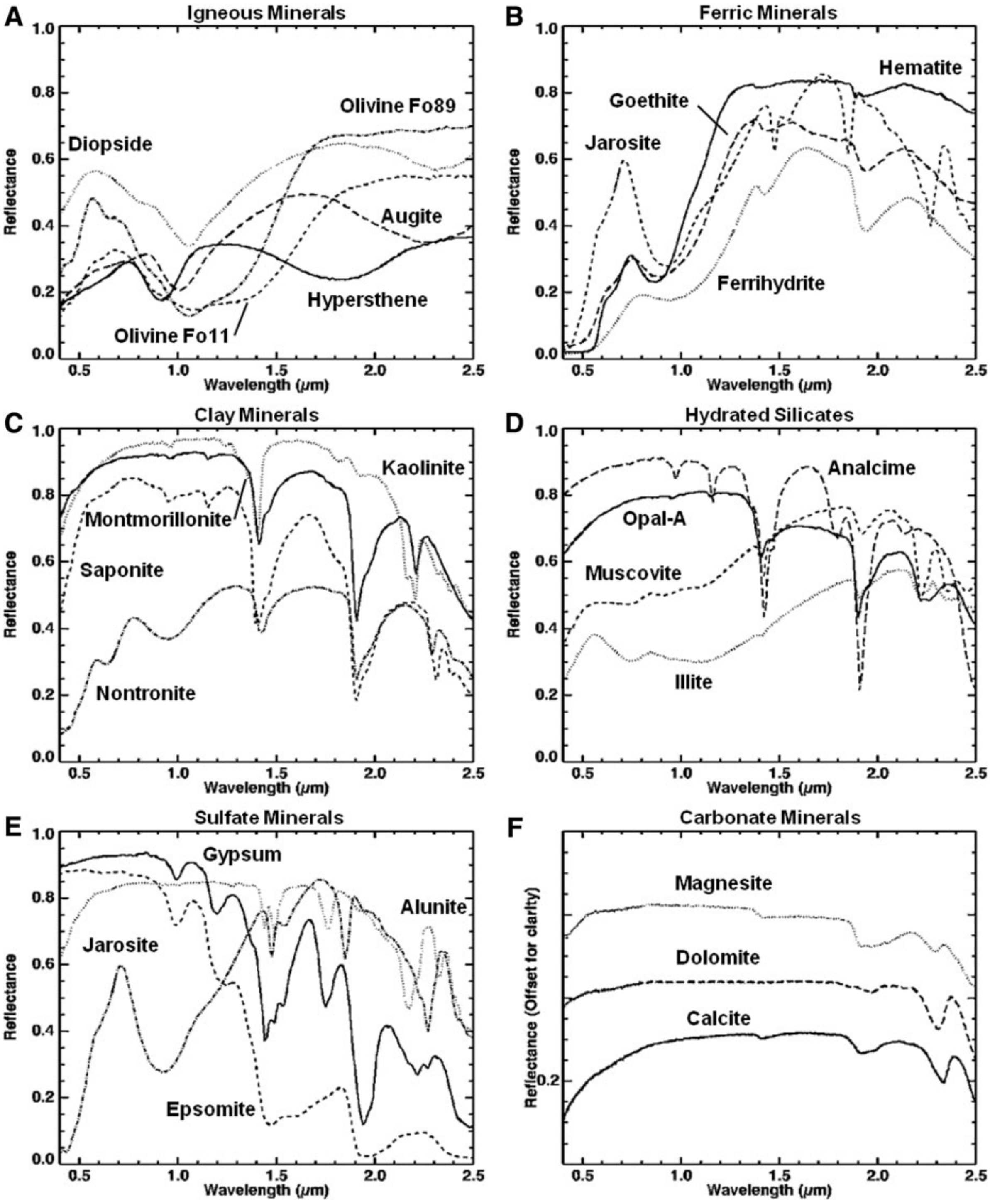

FIG. 4. Example library spectra of minerals identified with an ASD visible/shortwave infrared spectrometer.

size (27 × 46 mm) and thickness (30 μm), ground to standard polish and left unstained and uncovered. The thin sections were studied with a Nikon SMZ-U Stereozoom microscope with cross-polarizing filters and a Nikon Eclipse E600 polarizing microscope, under reflected and transmitted light illumination, plain and crossed-polarized light, and in some cases, with the use of a gypsum plate to enhance some fabric elements in thin section. The latter system included a high-precision rotating mechanical stage to enable the capability to return to specific spots in the section. To provide an integrated view of the microtexture, mineralogy, and paragenetic history of each sample, images were obtained over a range of magnifications (10–500 ×), with the highest (1000 ×) obtained under an immersion oil–mounted cover slip. Thin section petrography provided a particularly useful context for interpreting the results of X-ray powder diffraction and VSWIR reflectance spectra, each of which gives information about bulk composition over large areas of the sample, but without fine spatial context. Minor mineral components identified by XRD or spectral reflectance methods could, in most cases, be located within thin sections and properly placed with the paragenetic history of the sample.

4.5. Image processing and spectral analysis

Applying techniques originally developed for remote mineral mapping of planetary surfaces with instruments on board flyby and orbiting spacecraft, MMI multispectral microimages were processed in ENVI to produce compositional endmember maps. Three-band RGB color composites simulating natural color (*e.g.,* 0.64, 0.52, and 0.46 μm) were displayed for each sample, while composites of other bands (*e.g.,* 1.43, 0.91, and 0.52 μm) were used to generate the VSWIR RGB color composite images. Images employed a linear stretch to enhance color differences, and subtle color differences were revealed by applying a decorrelation stretch to the bands (*e.g.,* Gillespie *et al.,* 1986; Farrand *et al.,* 2006, 2007; Weitz *et al.,* 2010).

A variety of methods were used to identify regions of interest (ROIs) from which representative spectra, that is, ''spectral endmembers,'' could be extracted. These spectral endmembers, or spectra from ''image endmembers,'' are averages of spectra from multiple pixels extracted from the image that represent specific microtextural and compositional domains with typical spectral signatures in the image datacube. Mapped spectral endmembers consisted of averages of 100 to >1000 pixels of specific domains, which in some instances were spread over different areas of the sample. In some cases, endmembers represented single mineral phases, but more often they consisted of mixed-phase assemblages (where grain sizes were too fine to resolve at the MMI pixel scale). Endmembers were mapped to the sample, revealing spatial relationships that helped define the paragenesis (*i.e.,* the relative temporal ordering of phases and microfabrics) of the rock. The ROIs were selected through the combined use of decorrelation stretches of color composite images; band ratios targeting specific absorptions associated with the presence of Fe^{2+}, Fe^{3+}, and OH/H_2O; and the Minimum Noise Fraction Transformation (MNF) function (Green *et al.,* 1988) and Pixel Purity Index (PPI) algorithm (Kruse *et al.,* 1993; Rowan *et al.,* 2004) provided with ENVI, which revealed groups of unique endmember pixels.

The pixels identified through MNF and PPI methods, along with those identified through decorrelation stretches and band ratios, were selected as ROIs from the representative spectral classes (endmembers). These spectral endmembers generated from the ROIs were then used to produce maps that show the distribution of spectral signatures in the sample by using the Spectral Angle Mapper classification method in ENVI (Kruse *et al.,* 1993). The classification resulted in a spectral ''endmember map'' that shows the distribution of spectral endmembers in the sample.

The spectrum from each spectral endmember was then compared to library spectra from the USGS (Clark *et al.,* 2007), RELAB (Pieters and Hiroi, 2004), and ASTER (Baldridge *et al.,* 2009) spectral libraries, convolved to the MMI bandpasses (Table 1), to identify best-fit minerals (or rocks) for each spectral endmember (Fig. 5). Normal and continuum-removed (*i.e.,* Clark and Roush, 1984; Clark *et al.,* 2003) endmember spectra were compared and matched to convolved library spectra, ranked in order of best to worst match, by using the Spectral Angle Mapper and Spectral Feature Fitting methods (Kruse *et al.,* 1993; Rowan *et al.*, 2004) within the Spectral Analyst tool in ENVI.

Spectra of the suggested spectral library matches and spectral endmembers were visually compared to identify the best-fit spectra, including mineral(s), mineral group(s), assemblages, or whole rocks. Care was taken to make sure that the suggested mineral matches ''made sense'' in relationship to the rock origin inferred from the geological context, microtexture, and general composition obtained with the MMI (see the Results section).

5. Results

This section provides an overview of results obtained with the MMI and conventional laboratory techniques in the analysis of Mars analog samples. Reflectance spectra obtained with the MMI are compared with library spectra convolved to the MMI bandpasses to identify best-fit mineral/rock matches. Interpretations are then compared to spectra obtained with the ASD spectrometer, mineralogy based on XRD, and petrographic observations from thin sections. Results from conventional laboratory techniques were used to validate interpretations of petrogenesis based on MMI data and assess the performance of the MMI (see Section 6 for discussion).

5.1. Vesicular basalt (Sample 17)

Sample 17 was collected (by J.D.F.) from a lava flow located along the southeastern coast of Hawaii, near South Point. Laboratory analysis revealed the sample to be a fine-grained vesicular basalt containing phenocrysts of plagioclase feldspar, pyroxene, and minor amounts of olivine (see Section 5.1.3 for observations from laboratory techniques). This sample is highly relevant, as basalts are widespread lithotypes of Mars (*e.g.,* Christensen *et al.,* 2000; McSween *et al.,* 2003, 2006a, 2006b; Hamilton and Christensen, 2005; Haskin *et al.,* 2005).

5.1.1. MMI images and spectra with comparison to convolved library spectra

MMI-generated color composite images of sample 17, along with a corresponding spectral endmember map, are shown in Fig. 6. Figure 7 shows plots for the endmember spectra, along with matching library spectra, convolved to the MMI bandpasses (see Table 1). Table 4 shows a summary of spectral features and absorptions, along with rock/mineral matches. For a list of specific library spectra used for rock/mineral identification, see Appendix Table A1.

A comparison of MMI images shows that the sample contains white and olive-green phenocrysts (in visible color image) scattered through a vesicular, dark-colored, aphanitic matrix (*i.e.,* groundmass). The bright diagonal line on the left side of the sample is a saw mark. The white phenocrysts range in size from approximately 125–1250 μm, while the olive-green phenocrysts range from 125 to 1875 μm. Vesicles have a mean diameter of 438 μm and range in size from 190 to 780 μm.

Analysis of the MMI images suggests the presence of five spectral endmembers (as shown in Figs. 6D and 7A). Three

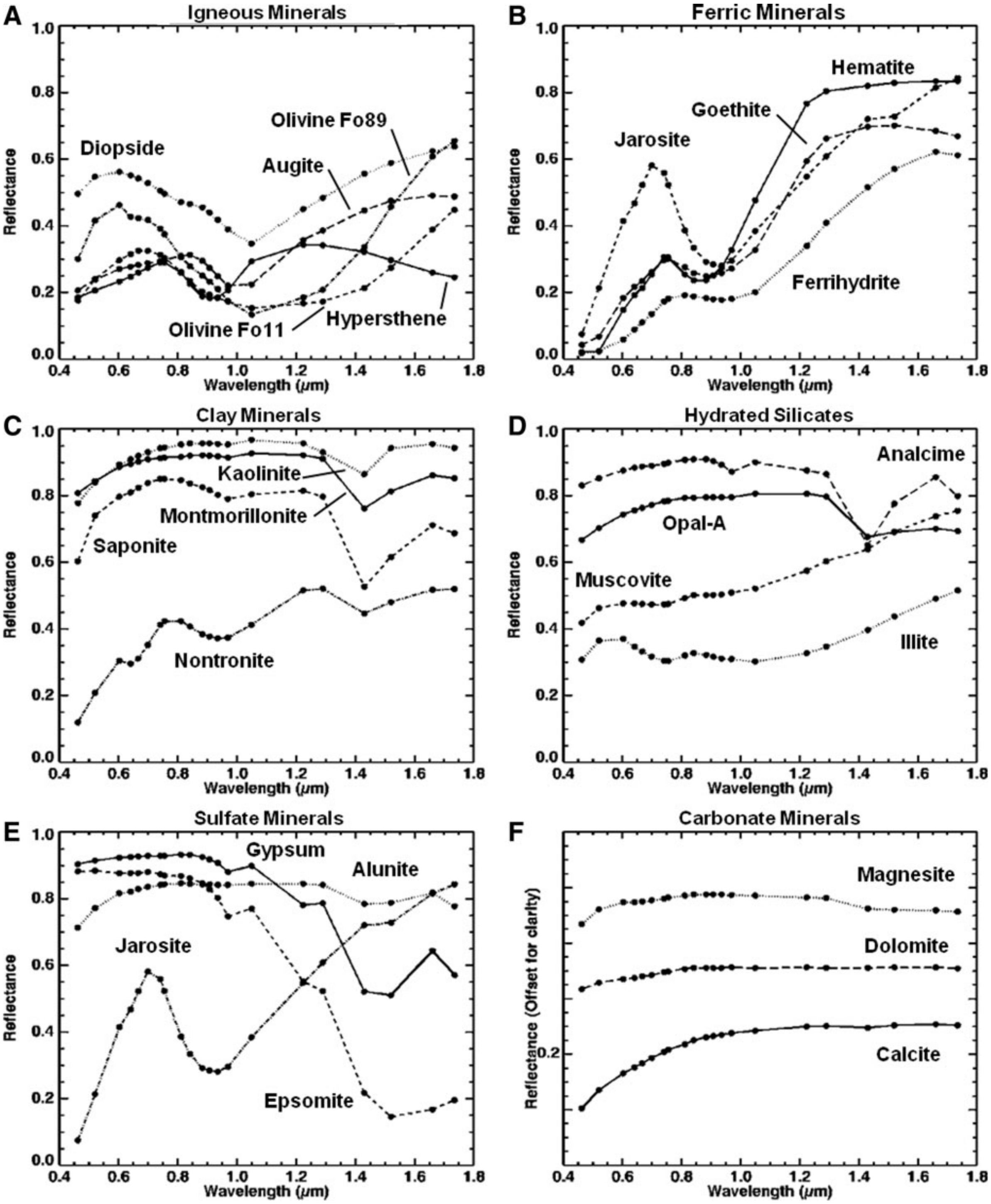

FIG. 5. Example laboratory library spectra of minerals presented in Fig. 4 convolved to the MMI wavelength centers and bandpasses (black spots) listed in Table 1.

of these spectral endmembers are associated with the olive-green phenocrysts.

The spectral endmember mapped as blue is associated with the dark, fine-grained matrix. The spectrum has a low reflectance and exhibits a flat spectrum with a shallow absorption at the 1.05 μm channel. The spectrum matches the library spectrum for basalt. The weak absorption at 1.05 μm may be due to the presence of either fine-grained high-Ca clinopyroxene (such as diopside) or olivine in the matrix. (Note: Unless stated otherwise, the position for a mineral absorption cited in the text coincides with an MMI channel; thus the absorption is presented by using the MMI channels.)

The spectral endmember mapped as magenta is associated with the white-colored phenocrysts. The spectrum has a sinusoidal shape and a broad, shallow absorption centered at 1.22 μm. The absorption at 1.22 μm is consistent with the

TABLE 4. ENDMEMBER SPECTRA AND MINERAL/ROCK MATCHES, BY SAMPLE NUMBER

Endmember	*Textural element*	*Key features and absorptions (μm)*	*Rock or mineral(s) library match*
Vesicular basalt (sample 17)			
Blue	Dark matrix	Low reflectance, flat shape; absorption at 1.05	Basalt with pyroxene
Magenta	White phenocryst	Relative high reflectance, sinusoidal shape; absorption at 1.22	Plagioclase feldspar
Green	Green phenocryst	Broad V-shape; absorption at 1.05	Diopside
Red	Green phenocryst	Broad U-shape; absorption at 1.05	Olivine
Orange	Green phenocryst	Broad U-shape; absorption at 1.05	Olivine
Silicic volcanic breccia (sample 14)			
Magenta	Red cement	Absorption edge at 0.52, peak at 0.76; absorption at 0.94	Fe oxyhydroxide (goethite or lepidocrocite)
Red	Red cement	Absorption edge at 0.52, peak at 0.74; absorption at 0.88	Hematite
Blue	Gray cement	Shallow sinusoidal shape; no absorptions present	Unknown (no diagnostic absorption)
Green	White cement	High reflectance, steep positive slope in viz; absorptions at 0.97 and 1.43	Hydrated mineral (clay, opal-A, or zeolite)
Yellow	Light groundmass in clasts	High reflectance, positive slope; absorptions at 0.88, 0.97, and 1.43	Mix of unknown with hematite and hydrated mineral (clay, opal-A, or zeolite)
Purple	Gray wispy laminations in clasts	Positive slope in viz; absorptions at 0.97 and 1.43	Mix of unknown with hydrated mineral (clay, opal-A, or zeolite)
Basaltic volcanic breccia (sample 10)			
Blue	Dark groundmass in clasts	Low reflectance, flat shape; absorption at 1.05	Basalt with pyroxene
Purple	Gray rind on central clast	Broad V-shape; absorption between 0.97 and 1.05	Augite
Magenta	Light gray cement around clasts	Positive slope in viz and negative slope in IR; absorptions between 0.97 and 1.05, 1.43 and 1.52	Mix of pyroxene and hydrated mineral (zeolite or sulfate)
Brown	Light gray/white cement	Steep positive slope in viz and negative slope in IR; absorptions between 0.97 and 1.05, 1.43, and 1.52	Mix of pyroxene and hydrated mineral (zeolite or sulfate)
Green	White cement	Steep positive slope in viz and negative slope in IR; absorptions at 0.97 and 1.43	Hydrated mineral (clay, opal-A, or zeolite)
Light blue	White cement	Steep positive slope in viz and negative slope in IR; absorptions at 0.97, 1.22, 1.43, and 1.52	Hydrated mineral (zeolite or sulfate)
Red	Orange cement	Positive slope; absorption edge at 0.52; peak at 0.81; absorptions at 0.64, 0.94, and 1.43	Nontronite (minor Fe oxide)
Orange	Orange cement	Positive slope; absorption edge at 0.52; peak at 0.81; absorptions at 0.64, 0.97, 1.05, 1.43, and 1.52	Mix of nontronite, pyroxene, and hydrated mineral (zeolite)

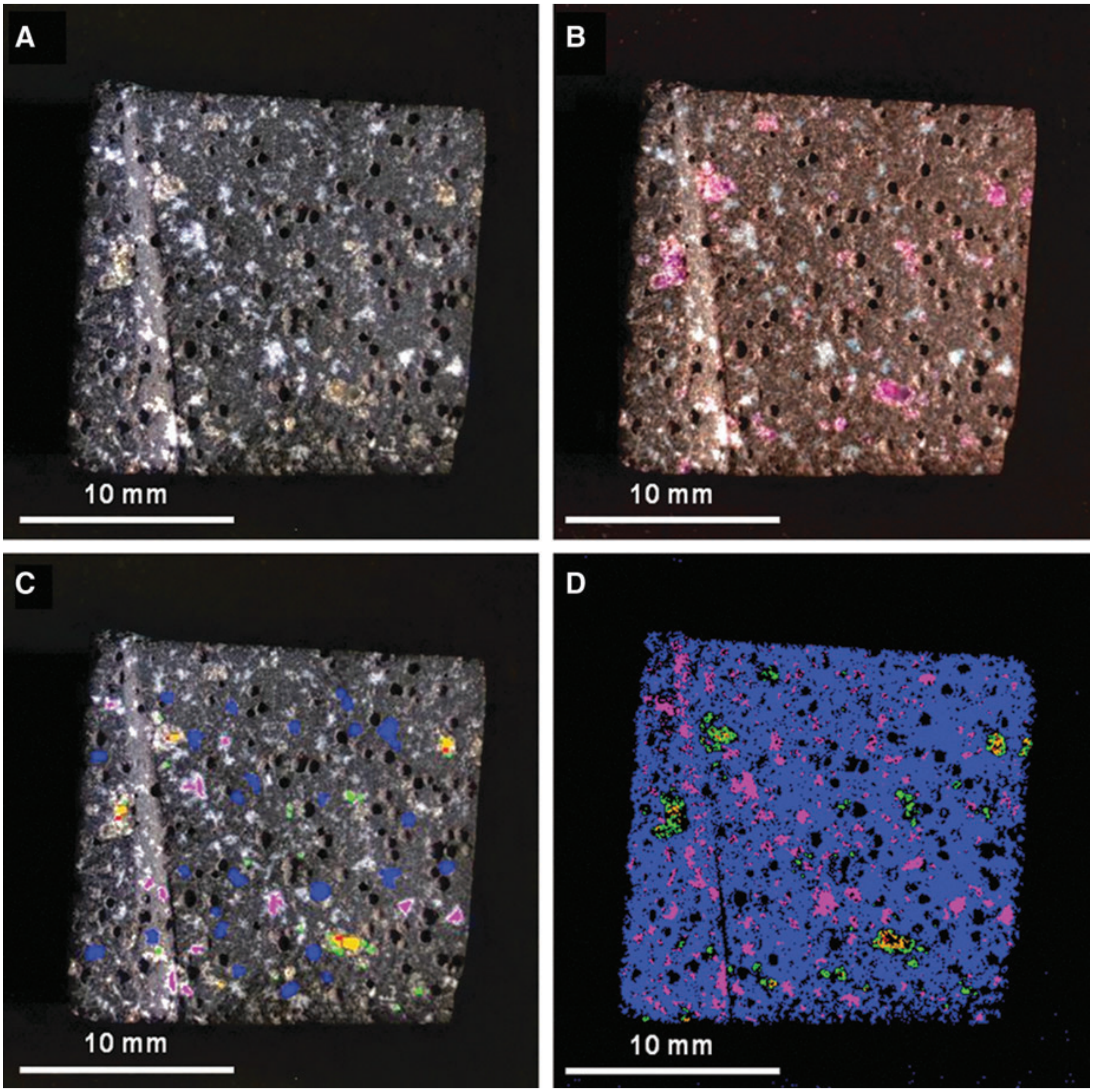

FIG. 6. MMI-generated color composite images and endmember map of sample 17. (**A**) Visible-color RGB composite image composed of MMI bands 0.64, 0.52, and 0.46 μm, respectively, to simulate natural color. (**B**) False-color RGB composite image composed of MMI bands 1.52, 0.88, and 0.64 μm, respectively, to bring out subtle color differences in materials due to variations in composition. (**C**) Visible-color RGB composite similar to (A) with ROIs used to generate endmember map (D) and corresponding endmember spectra (Fig. 7A and 7B). (**D**) Endmember map generated in ENVI by using supervised classification with ROIs as input parameter to map endmember distribution. Each MMI subframe image size is 25×25 mm at 62.5 μm/pixel. (A–C) are linear stretched.

convolved library spectrum for plagioclase feldspar (best match to Ca-rich plagioclase feldspar, anorthite). The broad, shallow absorption in the VNIR range at 1.2–1.3 μm is most likely due to Fe^{2+} substituting for Ca^{2+} at coordinated sites within the plagioclase structure (Burns, 1993).

The spectral endmember mapped as green in the endmember map is associated with the smaller, olive-green phenocrysts and also lines the edges of the larger olive-green phenocrysts. The spectrum includes a V-shaped absorption at 1.05 μm. This spectrum is consistent with the library spectrum for high-Ca clinopyroxene, with a best match to diopside. Unlike olivine, which exhibits a U-shaped absorption at 1.05 μm, diopside exhibits a characteristic V-shaped absorption at 1.05 μm. On this basis, it is concluded that the best match is with diopside.

The spectral endmembers mapped in red and orange correspond to the large olive-green phenocrysts, most visible in the large phenocryst toward the bottom right side of the sample as shown in Fig. 6. The red endmember is associated with the interior of the phenocryst, while the orange endmember lies between the red and green endmembers (Fig. 6D). The spectra have a U-shaped absorption centered at 1.05 μm. The orange endmember spectrum has a lower reflectance than the red endmember. Both endmembers match to the library spectra for olivine, with closest correspondence being to Fe-rich olivine or possibly

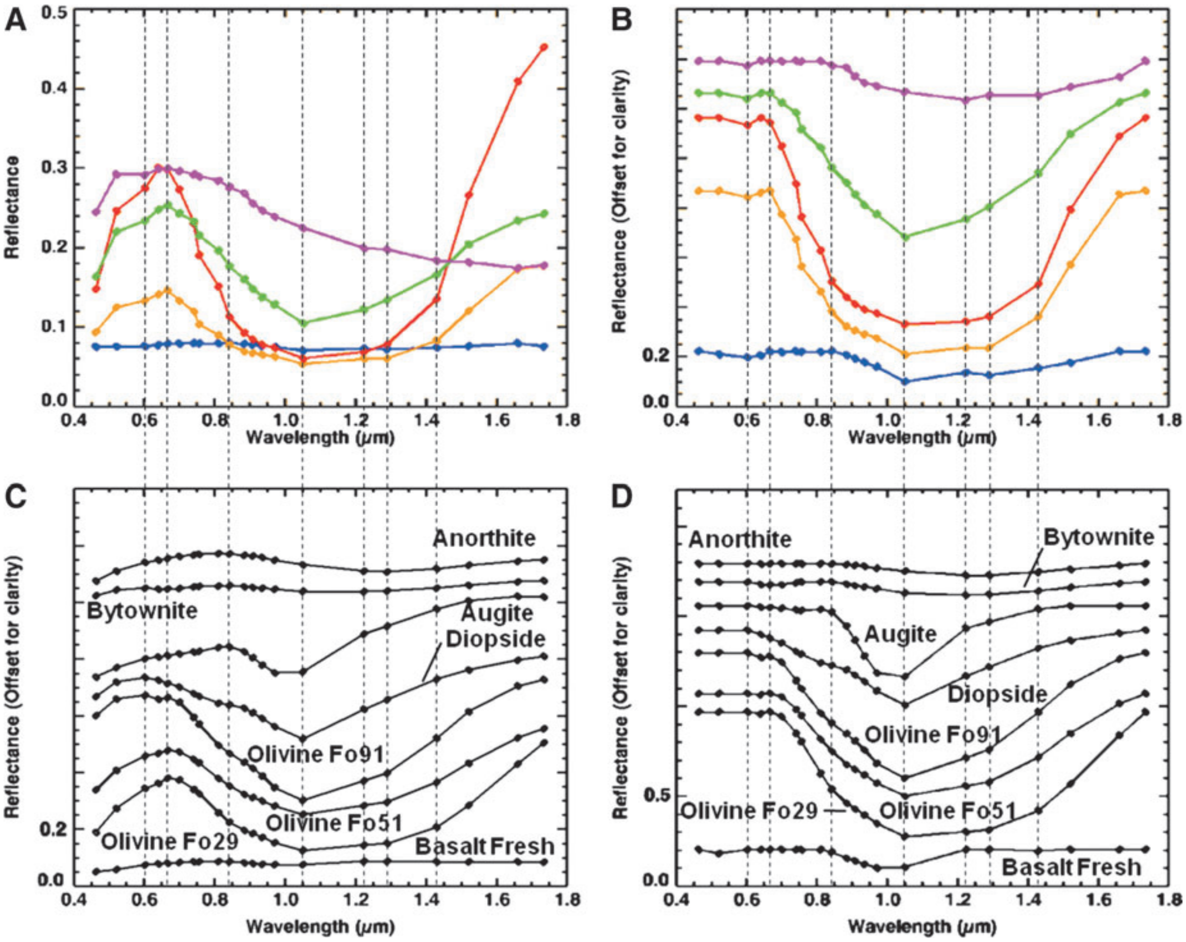

FIG. 7. Comparison of MMI-generated spectra of endmembers (**A** and **B**) from sample 17 (Fig. 6) and representative matching library spectra convolved to MMI bandpasses in Table 1 (**C** and **D**). Vertical lines correspond to MMI channels 0.6, 0.67, 0.84, 1.05, 1.22, 1.29, and 1.43 μm. See text for details on features and discussion. Spectra on the left are normal, while spectra on the right are continuum-removed. Continuum-removed and library spectra are offset for clarity. For details on library spectra used, see Appendix A.

an intermediate Fe-Mg composition. The difference between the two endmember spectra may be attributed to grain size effects (*e.g.,* Hapke, 1993; Clark, 1999), which affect the overall reflectance and depth of absorptions. Since the exact position and width of the 1.05 μm absorption in olivine depends on the Mg/Fe ratio (Burns, 1970; King and Ridley, 1987; Sunshine and Pieters, 1998; Isaacson and Pieters, 2010), the shift and width can be used to further distinguish between Fe-rich and Mg-rich olivine. Within the MMI channels, Fe-rich olivine (fayalite) exhibits a broader-shaped absorption at 1.05 μm compared to Mg-rich olivine (forsterite) (see Figs. 5A and 7). In addition, the position of the 0.60 μm peak shifts from 0.60 μm for Mg-rich to 0.67 μm for an intermediate to Fe-rich composition (Figs. 5A and 7). Therefore, the peak position at 0.67 μm, along with the broad, U-shaped absorption at 1.05 μm, compares best with an olivine of intermediate to Fe-rich composition.

5.1.2. Interpretation of MMI results

MMI images and associated spectra of sample 17 suggest that the sample is a vesicular basalt with scattered plagioclase feldspar and clinopyroxene phenocrysts, as well as a few pyroxene-rimmed olivine phenocrysts. The fine-grained groundmass and vesicular texture are consistent with rapid cooling of a volatile-rich lava.

5.1.3. Laboratory observations of sample 17

5.1.3.1. Visible to shortwave infrared spectroscopy. Visible/shortwave infrared spectra were collected from three locations (A–C, Fig. 8) on sample 17, targeting the major mineralogical and microtextural components of the sample. Figure 9 displays the spectra acquired for the range 0.35–2.50 μm, along with corresponding library spectra (See Table A1 for specific library spectra). Each spot was centered on a major component of interest, but due to the 6 mm spot size, it also included portions of other microtextural and compositional domains.

Spot A (Fig. 9A and 9B) was centered on a large olive-green phenocryst but incorporated a small amount of the surrounding matrix and white phenocrysts. The spectrum shows a broad absorption centered at 1.07 μm (1.08 for continuum-removed) as well as minor features at 0.86 and 1.28 μm (0.87 and 1.29 μm for continuum-removed). Compared to library spectra, this spectrum is consistent with Fe-rich olivine. Typically, Mg-rich endmembers (*i.e.,* forsterite)

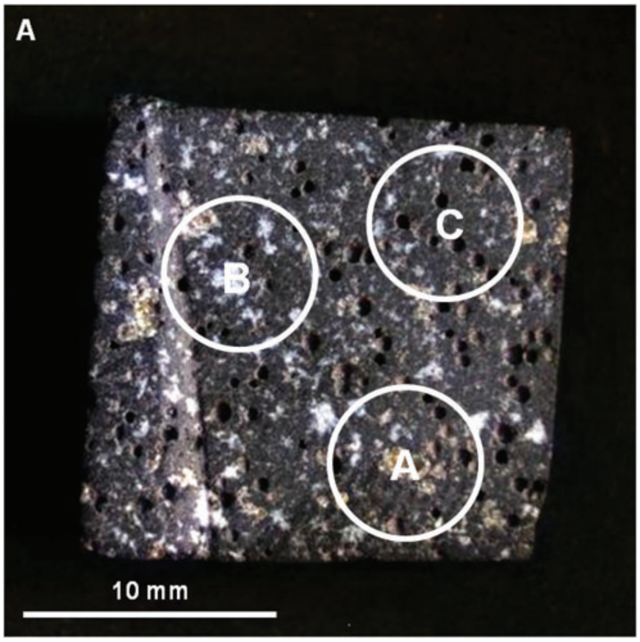

FIG. 8. Areas on sample 17 analyzed with VSWIR spectrometer. Visible-color, subframe image of sample 17 acquired by the MMI composed of bands RGB = 0.64, 0.52, 0.46 μm, respectively, to simulate natural color, with white circles (A–C) marking areas analyzed by the laboratory spectrometer (spectra are shown in Fig. 9). Image size is 25×25 mm at 62.5 μm/pixel. Spot size diameter is ~ 6 mm. Color images available online at www.liebertonline.com/ast

exhibit an absorption between 1.03 and 1.05 μm, while Fe-rich endmembers (*i.e.,* fayalite) exhibit an absorption between 1.05 and 1.08 μm (Sunshine and Pieters, 1998; Isaacson and Pieters, 2010).

Spot B (Fig. 9A and 9B) was centered on a large white phenocryst but also includes some of the surrounding matrix. The spectrum has a relatively flat reflectance curve, with a decreasing slope toward longer wavelengths and two absorptions at 1.03 and 1.28 μm (1.04 and 1.29 μm, respectively, for continuum-removed). Additional weak absorptions are present at 2.22 and 2.29 μm. Compared with library spectra, the 1.03 absorption is attributed to high-Ca clinopyroxene (best match to augite) and the 1.28 μm absorption to olivine present in the surrounding fine matrix. Although Ca-rich plagioclase feldspar may exhibit an absorption in the VNIR range about 1.2–1.3 μm due to Fe^{2+} substituting Ca^{2+} in plagioclase feldspar (Burns, 1993), this absorption in feldspars is pretty weak and would likely be swamped by stronger absorptions in similar positions from olivine or pyroxene. Thus, the 1.28 μm absorption is more consistent with the shoulder absorption in olivine. The weak absorptions at 2.22 and 2.29 μm are consistent with a clay mineral (as Al,Fe-smectite), which likely formed from minor weathering of the plagioclase feldspar or surrounding matrix.

Spot C (Fig. 9A and 9B) was centered on the dark-toned matrix but incorporates a few white phenocrysts. The spectrum has a low reflectance with an absorption at 1.03 μm and shoulder at 1.28 μm. A weak absorption is also present at 2.22 μm. Compared to library spectra, the spectrum is consistent with ''basalt.'' Similar to spot B, the absorption at 1.03 μm is due to the presence of high-Ca clinopyroxene, while the 1.28 μm feature is most likely contributed by smaller concentrations of olivine in the matrix. Given the fine-grained nature of this region of the sample, the pyroxene and olivine features are most likely contributed by microlites (microphenocrysts) in the basalt matrix. The weak absorption at 2.22 μm is consistent with minor hydroxylation of the basaltic glass (Milliken *et al.,* 2008) or, similar to spot B, consistent with a clay mineral (Al-smectite).

5.1.3.2. X-ray diffraction. X-ray diffraction analysis was carried out on representative bulk, powdered materials from sample 17 to provide additional ''ground truth'' for the MMI. The resulting X-ray diffractogram (Fig. 10) contains maximum 2θ peaks indicative of Ca-rich plagioclase feldspar at 27.87°, pyroxene (best fit with high-Ca clinopyroxene) at 29.8°, and olivine at 36.37°. Significant background intensity in the diffractogram is related to iron associated with volcanic glass in the sample matrix. The 2θ peaks are consistent with primary basaltic minerals (*e.g.,* pyroxene, plagioclase feldspar, and olivine), with no evidence for secondary alteration minerals within the instrument's detection limit of 4%.

5.1.3.3. Thin section petrography. Petrographic thin sections of sample 17 were analyzed to constrain mineral paragenesis and provide a microtextural context for interpreting VSWIR and XRD results. Observations under plain and cross-polarized light revealed the presence of clinopyroxene, olivine, and plagioclase feldspar phenocrysts, as well as small orthopyroxene crystals embedded in a vesicular matrix (*i.e.,* groundmass) dominated by basaltic glass and microlites of pyroxene and plagioclase feldspar (Fig. 11). These minerals were distinguished by their crystal habit and optical properties. In thin section, the plagioclase feldspar crystals exhibited characteristic polysynthetic twinning and actually consisted of clumps of multiple smaller crystals instead of single large phenocrysts as they appeared in hand sample. The mineralogy and texture of the sample is consistent with a vesicular basalt.

5.2. Silicic volcanic breccia (Sample 14)

Sample 14 was collected (by J.D.F.) from the Owen's Gorge area, south of Long Valley caldera and southeast of Mammoth Lakes, California. Analysis in which laboratory techniques were used (see Section 5.2.3) identified the sample to be a silicic volcanic breccia composed of angular clasts of a fine-grained, flow-banded rhyolite, cemented by calcite, ferric oxide/oxyhydroxide, and hydrated mineral cements.

5.2.1. MMI images and spectra with comparison to convolved library spectra

Figure 12 shows MMI-generated color composite images of sample 14 composed of visible and infrared bands, along with a spectral endmember map based on individual ROIs. Corresponding endmember spectra are shown in Fig. 13, along with matching library spectra. See Table 4 for a summary of endmember spectra features and absorptions, along with rock/mineral matches. For a list of specific library spectra used for rock/mineral identification see Table A1.

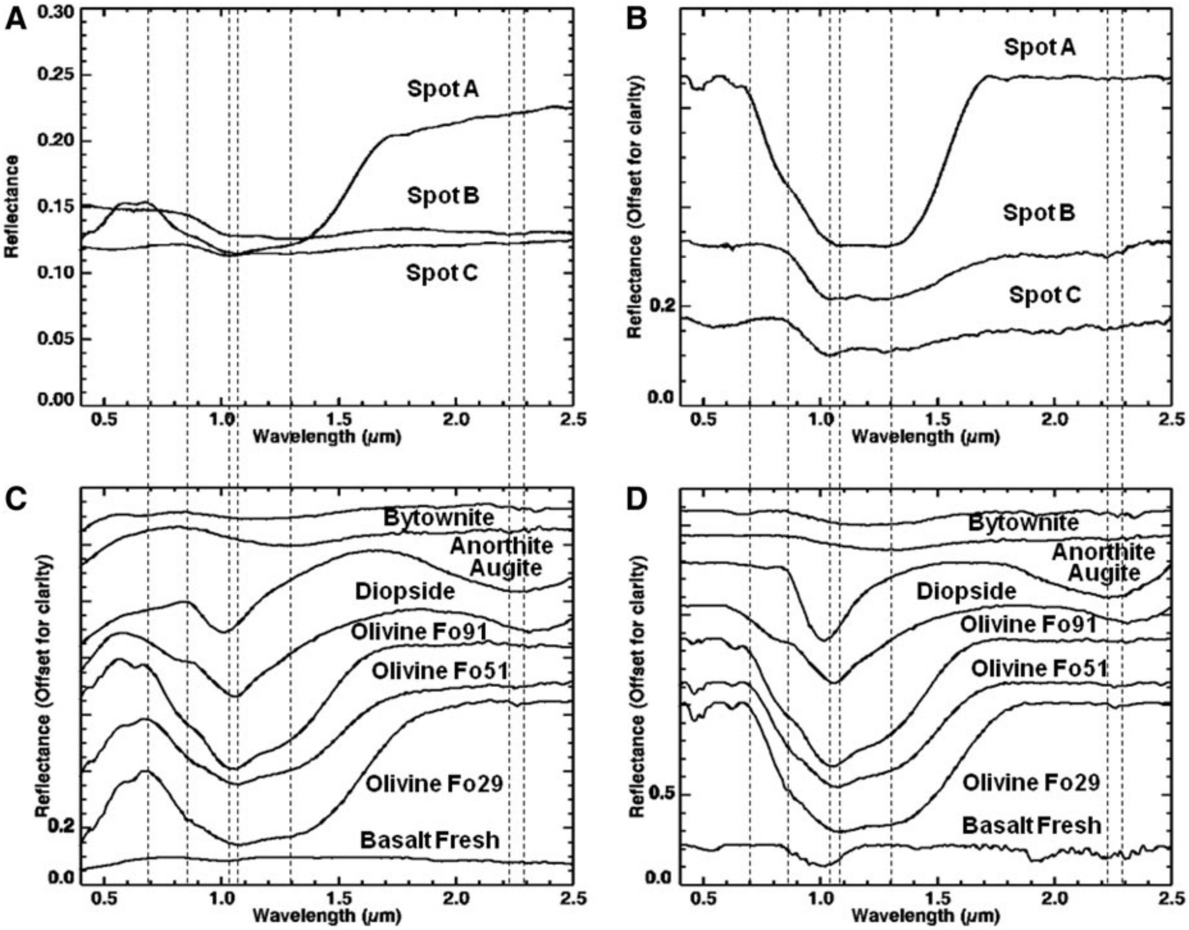

FIG. 9. Comparison of VSWIR spectra (**A** and **B**) collected from spots (A–C) on sample 17 (Fig. 8) with laboratory spectrometer and representative matching library spectra (**C** and **D**). Vertical lines correspond to features at 0.67, 0.86, 1.03, 1.07, 1.28, and 2.22, and 2.29 μm. See text for details on features and discussion. Spectra on the left are normal, while spectra on the right are continuum-removed. Continuum-removed and library spectra are offset for clarity. For details on library spectra used, see Appendix A.

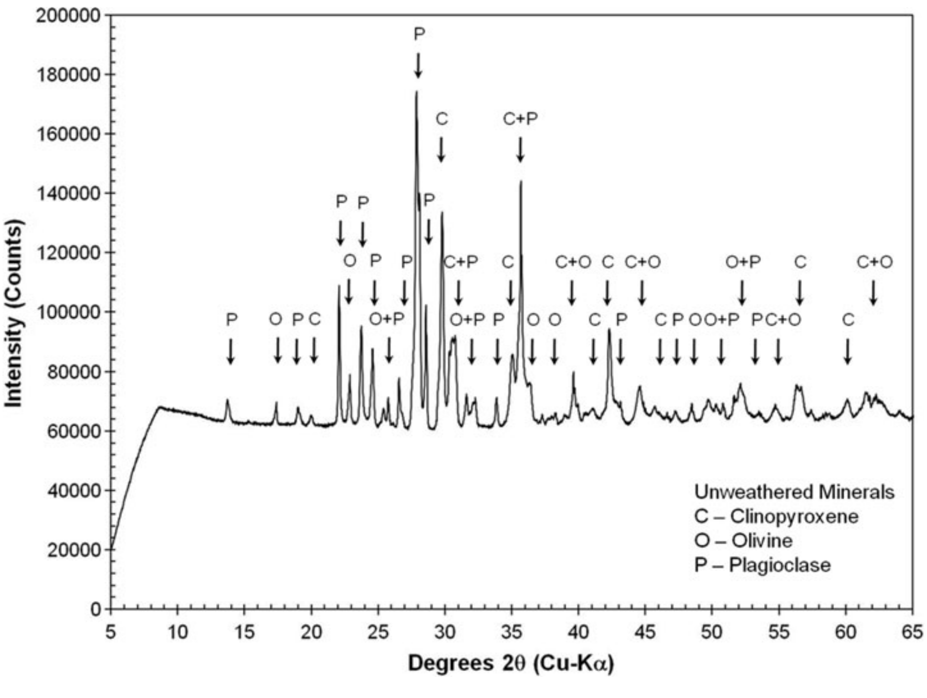

FIG. 10. X-ray powder diffractogram of bulk powder of sample 17. Mineral symbols on the peaks are clinopyroxene (C), olivine (O), and plagioclase feldspar (P). Significant background intensity is related to fluorescence of iron in Fe-bearing minerals and amorphous glass.

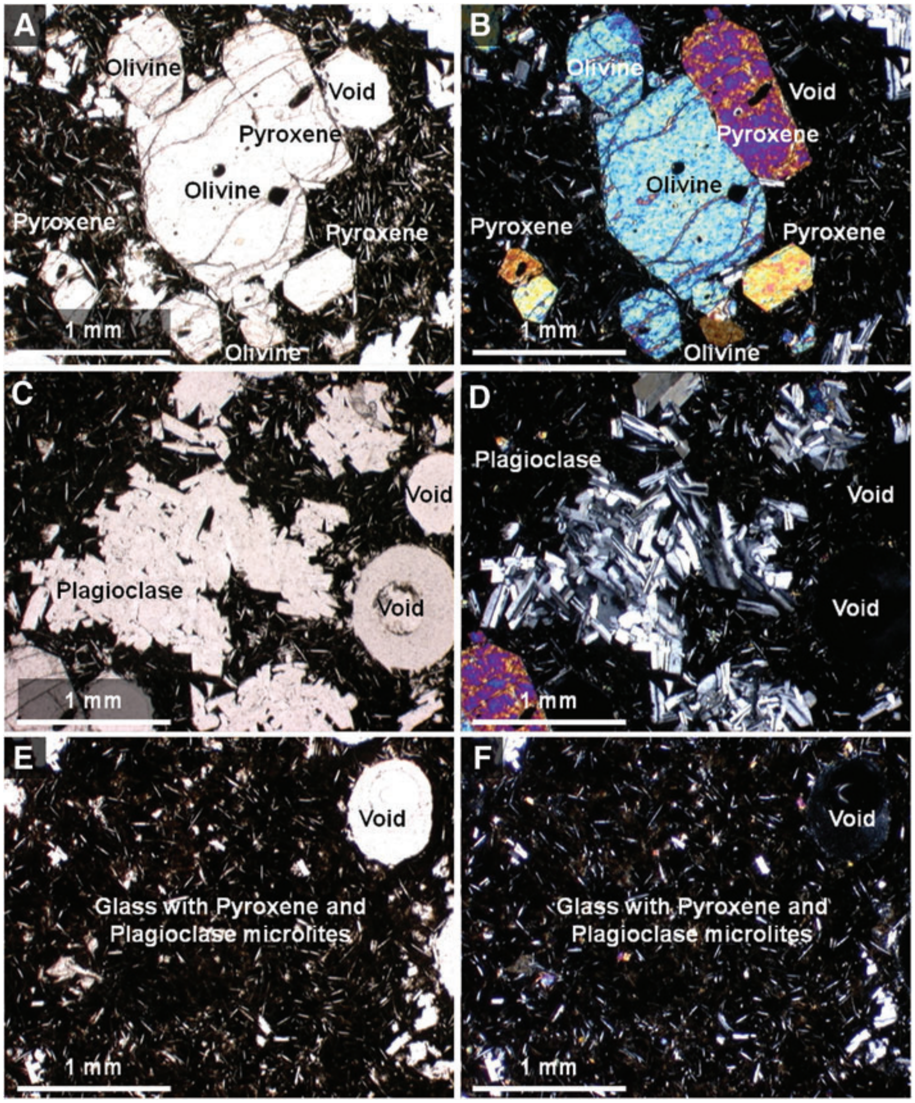

FIG. 11. Plain light (left) and crossed-polarized light (right) images of magnified areas of thin section of sample 17 obtained with a Nikon Eclipse E600 polarizing microscope targeting main elements with components labeled. These include pyroxene and olivine grains (**A** and **B**), plagioclase feldspar grains (**C** and **D**), and basalt matrix with pyroxene and plagioclase feldspar microlites (**E** and **F**). Color images available online at www.liebertonline.com/ast

Analysis of MMI images showed the sample to be a breccia consisting of tan-colored, angular to subangular clasts, with roundness values ranging from 0.5 to 0.7 (see Powers, 1953). The rock exhibits a poorly sorted, clast-supported fabric; some clasts appear to have been broken in place. The breccia was secondarily cemented by dark red and gray-colored authigenic minerals (seen in visible color image, Fig. 12A). Clasts show a very fine-grained internal fabric, with wispy, dark gray internal laminations. Overall, clasts are similar in composition (*i.e.,* monolithologic) and range from medium sand (0.25 mm) to pebble-sized clasts, with granules (~5 mm), and medium (~2 cm) pebbles dominating. The cement components are very fine-grained (below MMI spatial resolution) and fill what were originally irregular pore spaces between clasts. In the MMI images, the dark red cement appears first in its paragenetic sequence because it lines the pore walls. The gray cement appears later in the paragenetic sequence, mostly filling the central interiors of original pore spaces. In addition to the early dark red cement, there is a second, less abundant pore-lining cement that is white in color. This white-colored cement is visible in Fig. 12A and 12B and appears to be contemporaneous, or possibly post-dates slightly, the more abundant red cement. Both the red and white cements are also present as small patches within clasts and in that context could also be alteration products.

Spectral analysis of MMI data indicated the presence of at least six spectral endmembers (as shown in Figs. 12D and 13A). Four of these are associated with the different cement phases in the sample.

The red and magenta endmembers are associated with the dark red cement in Fig. 12. The red endmember spectrum has an absorption edge at 0.52 μm, a peak at 0.74 μm, and absorption at 0.88 μm. The spectrum is consistent with the library spectrum for hematite. Hematite has a diagnostic absorption centered at 0.88 μm when convolved to the MMI bandpasses (Fig. 13). In contrast, goethite has a wider absorption (compared to hematite), centered at 0.91 μm (0.94 and 0.97 μm for continuum-removed). The position of the absorption feature, however, can shift slightly, depending on particle size and crystallinity (*e.g.,* Morris *et al.,* 1985; Clark, 1999).

The magenta endmember differs from the red spectral endmember in having an absorption edge at 0.52 μm, a peak at 0.76 μm, and absorption centered at 0.94 μm (0.97 μm for

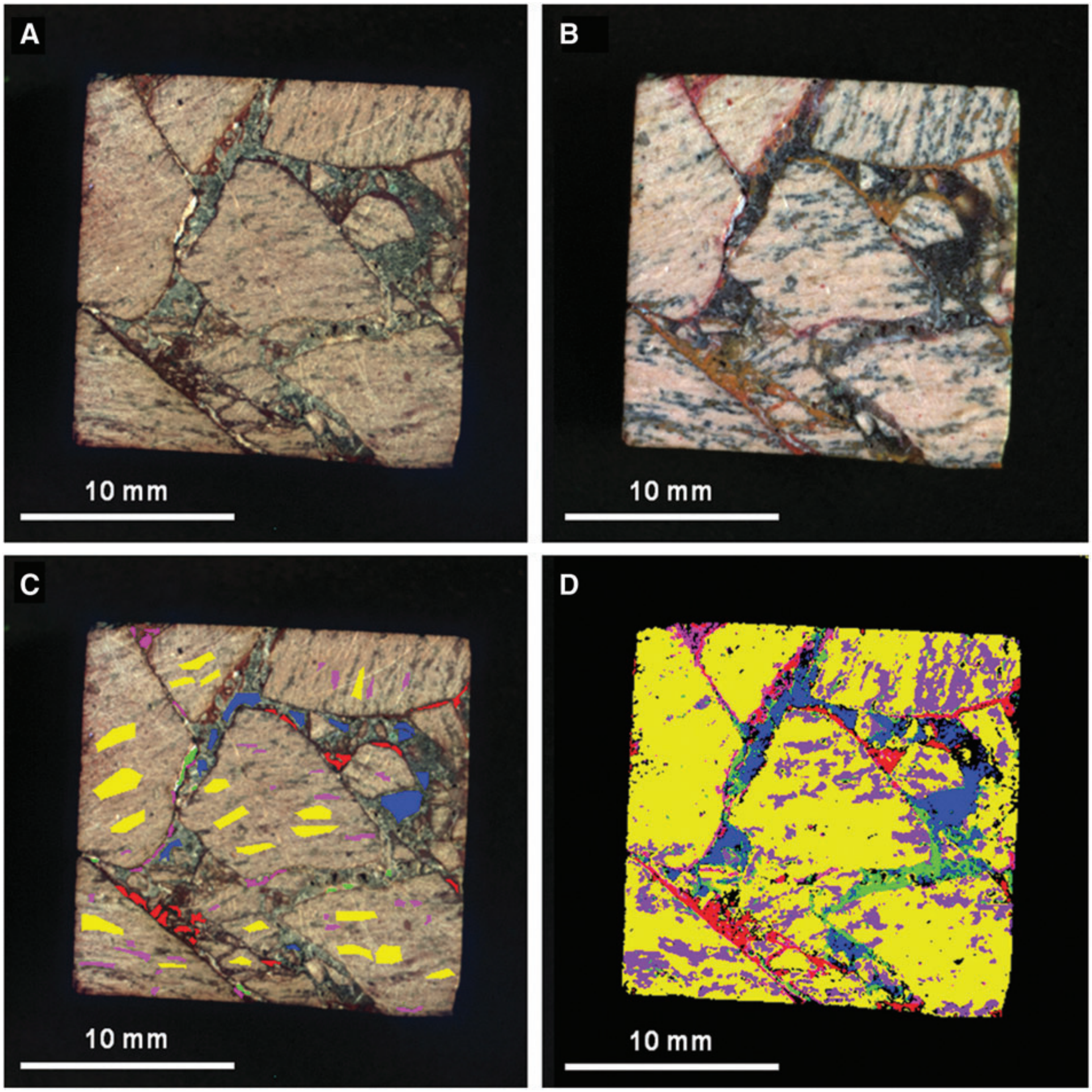

FIG. 12. MMI-generated color composite images and endmember map of sample 14. (**A**) Visible-color RGB composite image composed of MMI bands 0.64, 0.52, and 0.46 μm, respectively, to simulate natural color. (**B**) False-color RGB composite image composed of MMI bands 1.43, 1.05, and 0.74 μm, respectively, to bring out subtle color differences in materials due to variations in composition. (**C**) Visible-color RGB composite similar to (A) with ROIs used to generate endmember map (D) and corresponding endmember spectra (Fig. 13A and 13B). (**D**) Endmember map generated in ENVI by using supervised classification with ROIs as input parameter to map endmember distribution. Each MMI subframe image size is 25×25 mm at 62.5 μm/pixel. (A–C) are linear stretched.

continuum-removed). The endmember is consistent with the library spectrum for an iron oxyhydroxide, such as goethite (α-FeO(OH)), lepidocrocite (γ-FeO(OH)), or ferrihydrite ($\sim 5Fe_2O_3 \cdot 9H_2O$). Ferrihydrite has a broad absorption at 0.94 μm (centered at 0.97 and 1.05 μm for continuum-removed) and a peak at 0.81 μm, while lepidocrocite has a narrower, more symmetrical absorption (compared to ferrihydrite) at 0.94 μm (0.97 μm for continuum-removed) and a peak at 0.76 μm (Fig. 13). The peak at 0.76 μm and absorption centered at 0.97 μm (continuum-removed) suggest the best match is with lepidocrocite. However, it is important to note that, as a result of particle size effects, goethite can have a similar absorption (*e.g.,* Morris *et al.,* 1985; Clark, 1999), and spectrally distinguishing between these two phases in the present case is not possible.

The blue endmember is associated with the dark gray, pore-filling cement in Fig. 12. Figure 13 shows that, spectrally, this endmember has a low reflectance (relative to other portions of the sample) and exhibits a predominantly flat spectrum with a very shallow sinusoidal shape. No diagnostic absorptions are present within the MMI channels that can be attributed to a particular mineral or mineral class.

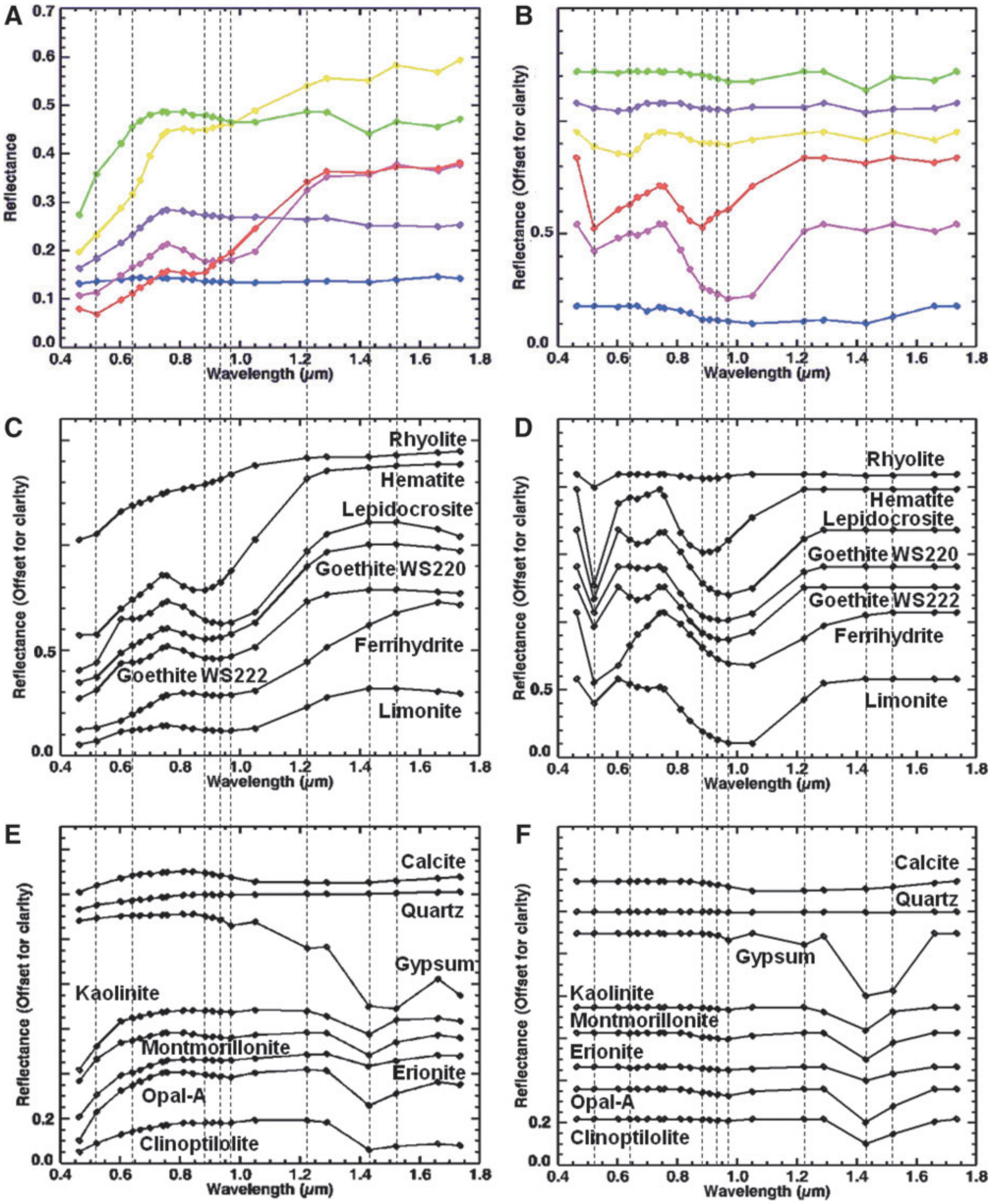

FIG. 13. Comparison of MMI-generated spectra of endmembers (**A** and **B**) from sample 14 (Fig. 12) and representative matching library spectra convolved to MMI bandpasses in Table 1 (**C–F**). Vertical lines correspond to MMI channels 0.52, 0.64, 0.88, 0.94, 0.97, 1.22, 1.43, and 1.52 μm. See text for details on features and discussion. Spectra on the left are normal, while spectra on the right are continuum-removed. Continuum-removed and library spectra are offset for clarity. For details on library spectra used, see Appendix A.

The green endmember in Fig. 12 is associated with the patchy, white-colored phase that coats the clasts in a few areas of the MMI image. In Fig. 13, its spectrum has a high reflectance (relative to other portions of the sample), with an absorption centered between 0.97 and 1.05 μm, and a strong absorption at 1.43 μm. Small patches of both the red and white cements occur within the interiors of a few clasts, suggesting they may be, in part, alteration phases. The spectrum is consistent with the presence of a hydrated clay mineral (*e.g.,* montmorillonite or kaolinite), opaline silica, or certain zeolites (*i.e.,* clinoptilolite or erionite). At the MMI spectral resolution, all these minerals have a strong absorption centered at 1.43 μm (Figs. 5 and 13). In contrast, zeolites like natrolite or hydrated sulfates like gypsum and kieserite have a broader absorption that encompasses both the 1.43 and 1.52 μm channels. This difference suggests that a match with a hydrated sulfate or zeolite, like natrolite, is less likely.

The purple endmember is associated with the dark gray, thin, wispy laminations within the angular clasts as shown in Fig. 12. The spectrum has absorptions at 0.94 and 1.43 μm. Unlike the yellow endmember, which is associated with the light-toned groundmass of the clasts and exhibits an overall positive slope in its spectrum from 0.76 to 1.73 μm, the purple endmember exhibits a slightly negative slope over the same range. The 0.94 μm absorption is consistent with an Fe oxyhydroxide, while the absorption at 1.43 μm is consistent with the presence of a hydrated mineral. Similar to the yellow endmember spectrum, the iron and hydrated mineral features in the purple spectrum would be consistent with hydration and oxidative weathering of a rhyolitic groundmass. The negative slope in the spectrum from 0.76 to 1.73 μm may result from elevated abundances of the hydrated mineral component or Rayleigh scattering of devitrifying glass in the surrounding groundmass (*e.g.,* Clark, 1999).

5.2.2. Interpretation of MMI results

The MMI images and associated spectra reveal that sample 14 is a breccia composed of fine-grained, light-colored angular clasts that exhibit a linear fabric consistent with flow banding. The light color of the clasts and lack of absorptions associated with mafic composition suggest a silicic composition. The clasts are cemented by a predominant, late paragenetic pore-filling cement that appears dark gray in MMI images. This late, dark gray cement postdates less abundant, dark red iron oxide and oxyhydroxide cements (as hematite and lepidocrocite/goethite) and a low-abundance, patchy hydrated mineral cement (as a zeolite or phyllosilicate) that appears white in color. The monolithologic composition of the clasts and their poor-sorting and angular shapes indicate minimal transport from the source area. These compositional and textural features are consistent with an origin as an autobrecciated silicic lava flow or possibly a near-vent pyroclastic (lapilli-tuff) deposit. The cements indicate that fluids of differing composition percolated through open pore spaces in the rock during its postburial history, cementing the rock early, before significant compaction. The presence of Fe oxides/oxyhydroxides and hydrated silica as early cement phases is consistent with early diagenetic fluids that were oxidizing, with a neutral to alkaline pH.

5.2.3. Laboratory observations of sample 14

5.2.3.1. Visible to shortwave infrared spectroscopy. Visible/shortwave infrared laboratory spectra were collected from three locations (A–C) on the surface of sample 14, targeting compositional and microtextural components (Fig. 14). Figure 15 displays the spectra acquired over the range 0.35 to 2.50 μm, along with corresponding library spectra. Figure 16 displays a close-up of the spectral region, 1.8–2.5 μm, from Fig. 15, along with corresponding library spectra (see Table A1 for specific library spectra). As with sample 17, because the ASD spot size is ~6 mm in diameter, spectra usually included more than one phase or fabric element.

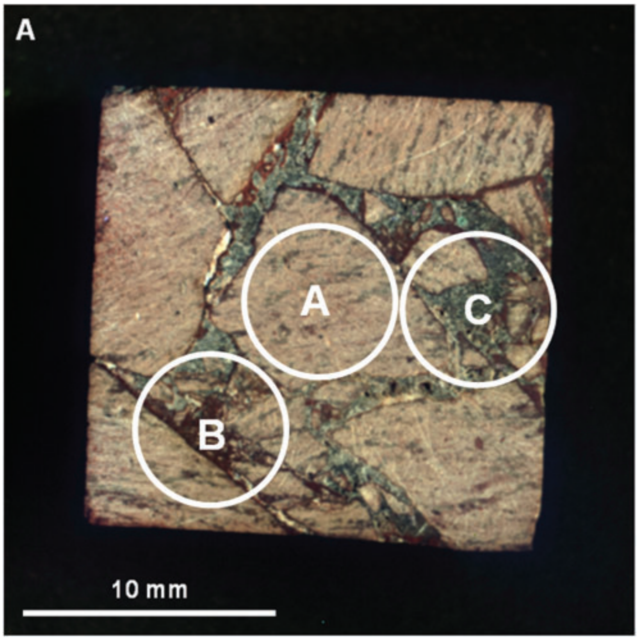

FIG. 14. Areas on sample 14 analyzed with VSWIR spectrometer. Visible-color, subframe image of sample 14 acquired by the MMI composed of bands RGB = 0.64, 0.52, 0.46 μm, respectively, to simulate natural color, with white circles (A–C) marking areas analyzed by the laboratory spectrometer (spectra are shown in Fig. 15). Image size is 25 × 25 mm at 62.5 μm/pixel. Spot size diameter is ~6 mm. Color images available online at www.liebertonline.com/ast

Spot A on sample 14 (Figs. 15A and 15B, 16A and 16B) was collected from the center of the large volcanic clast in the middle of the sample (Fig. 14). The resulting spectrum has a broad absorption at 0.87 μm (0.91 μm for continuum-removed); strong absorptions at 1.43, 1.91, 2.30, and 2.35 μm; and a weak absorption at 2.26 μm. Compared to library spectra, the absorption at 0.87 μm can be attributed to hematite. The remaining absorptions appear to be consistent with a mixture of an intermediate Fe-Mg smectite and the chlorite group mineral, clinochlore ($(\text{Mg,Fe}^{2+})5\ \text{Al(AlSi}_3)\text{O}_{10}(\text{OH})_8$) with a higher Fe/Mg ratio, where the 1.43, 1.91, and 2.30 μm absorptions are due to the Fe-Mg smectite, while the 2.26 and 2.35 μm absorptions are due to clinochlore. The absorption at 2.33–2.35 μm in clinochlore results from a combination of overtones of Mg-OH and shifts to longer wavelengths as the proportion of iron relative to magnesium increases (King and Clark, 1989; Bishop *et al.,* 2008; Ehlmann *et al.,* 2009).

Spot B on sample 14 (Figs. 15A and 15B, 16A and 16B) is centered on the red- colored cement but also incorporates some smaller volcanic clasts (Fig. 14). The spectrum is similar in shape to the spectrum for spot A but has a lower reflectance and different absorptions in the 2.0–2.5 μm range. The spectrum exhibits a broad absorption at 0.87 μm (0.91 μm with continuum-removed); absorptions at 1.42, 1.91, and 2.30 μm; and additional weak absorptions at 2.19, 2.22, 2.26, 2.35, and 2.37 μm. Compared to library spectra,

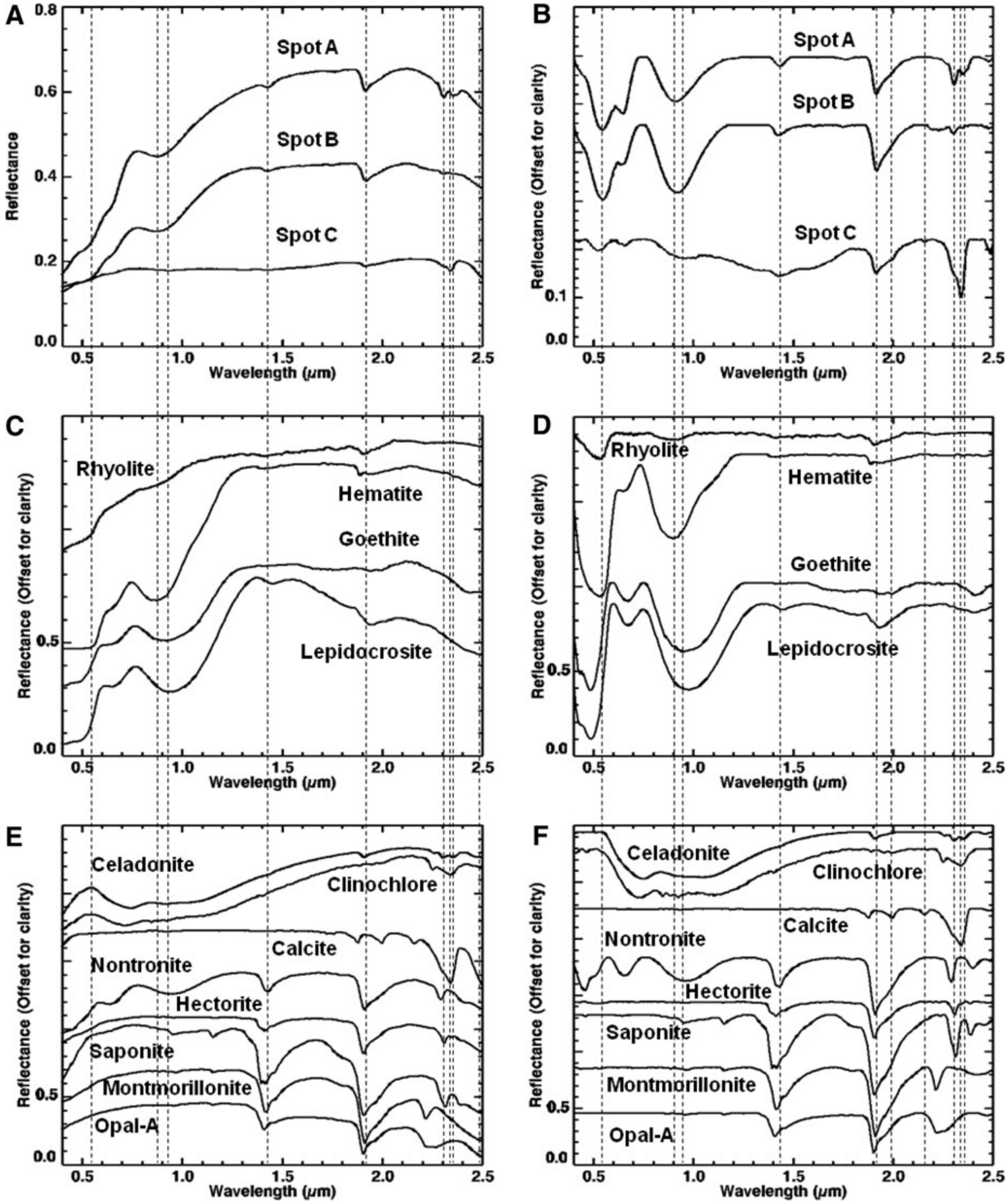

FIG. 15. Comparison of VSWIR spectra (**A** and **B**) collected from spots (A–C) on sample 14 (Fig. 14) with laboratory spectrometer and representative matching library spectra (**C–F**). Vertical lines correspond to features at 0.53, 0.87, 0.93, 1.42, 1.91, 2.3, 2.34, 2.35, and 2.5 μm. See text for details on features and discussion. Spectra on the left are normal, while spectra on the right are continuum-removed. Continuum-removed and library spectra are offset for clarity. Close-up of region 1.8–2.5 μm is shown in Fig. 16. For details on library spectra used, see Appendix A.

the absorption at 0.87 μm is consistent with hematite. The absorptions at 1.42, 1.91, 2.19, 2.22, 2.26, 2.30, 2.35, and 2.37 μm are consistent with a mixture of different hydrated minerals. Similar to spot A, the absorptions at 1.42, 1.91, and 2.30 μm are consistent with an Fe-Mg smectite, while the absorptions at 2.26 and 2.35 μm are consistent with clinochlore. The weak absorptions at 2.22 and 2.26 μm also suggest the presence of opaline silica (*i.e.,* opal-A). The weak 2.19 μm absorption may be due to hydrated volcanic glass (Milliken *et al.,* 2008). The 2.37 μm absorption is more difficult to associate with a particular mineral but may be from another phyllosilicate.

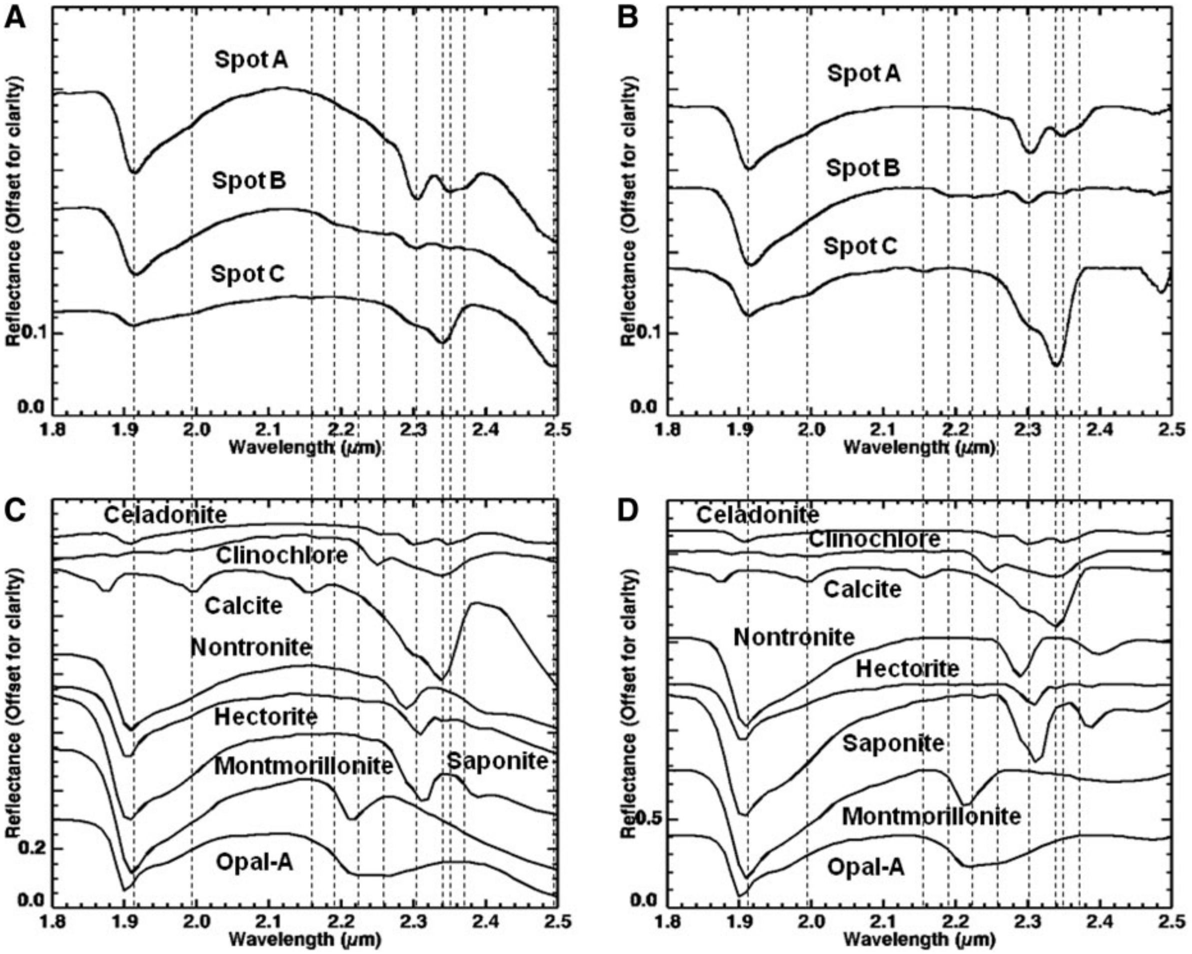

FIG. 16. Close-up of spectral region 1.8–2.5 μm from Fig. 15, where VSWIR spectra (**A** and **B**) collected from spots (A–C) on sample 14 (Fig. 14) with laboratory spectrometer are compared with representative matching library spectra (**C** and **D**). Vertical lines correspond to features at 1.91, 1.99, 2.16, 2.19, 2.22, 2.26, 2.3, 2.34, 2.35, 2.37, and 2.5 μm. See text for details on features and discussion. Spectra on the left are normal, while spectra on the right are continuum-removed. All spectra are offset for clarity. For details on library spectra used, see Appendix A.

Spot C on sample 14 (Figs. 15A and 15B, 16A and 16B) is centered on the dark gray cement but also incorporates smaller amounts of the dark red cement and volcanic clasts (Fig. 14). The spectrum has a low reflectance and absorptions at 1.42, 1.91 μm, along with paired absorptions at 2.34 and 2.50 μm. Additional weak absorptions are observed at 1.99 and 2.16 μm, along with a broad absorption at 0.93 μm (0.96 μm with continuum-removed). Compared to library spectra, the paired absorptions at 2.34 and 2.50 μm and weak absorptions at 1.99 and 2.16 μm are consistent with calcite. The absorption at 0.93 μm is consistent with the library spectrum for an iron oxyhydroxide, such as goethite or lepidocrocite (Morris *et al.,* 1985). This is in contrast with the 0.87 μm absorption in the spectra for Spots A and B, respectively, which is consistent with hematite. The 1.4 and 1.9 μm absorptions are due to vibrational overtones of H_2O, most likely from adsorbed water, or a minor hydrated mineral component, with features in the 2.0–2.5 μm being masked by the strong carbonate absorptions. (Note: The shoulder at 2.3 μm, along with the 1.4 and 1.9 μm absorptions, could also be due to the Fe-Mg smectite also found in spots A and B.)

5.2.3.2. X-ray diffraction. High-resolution XRD of representative bulk powder from sample 14 showed strong maximum 2θ intensity peaks for calcite at 29.53°, quartz at 26.68°, and plagioclase feldspar (best fit to albite) at 27.78°. Additional smaller maximum 2θ intensity peaks for hematite are present at 33.19°, goethite at 21.32°, clinochlore at 12.57°, and calcium-sodium zeolite, such as heulandite, or stilbite, at 9.89° (Fig. 17). The 2θ peaks are consistent with both primary volcanic minerals of felsic composition (*e.g.,* quartz and plagioclase feldspar) and secondary, hydration alteration minerals and cements (*e.g.,* calcite, Fe-oxides/oxyhydroxides, clay minerals, and zeolites). The absence of 2θ peaks for Fe-Mg smectite, identified with the SWIR spectrometer, in the X-ray diffractogram indicates the mineral abundance in the sample bulk powder was below the 4% detection limit of the instrument.

5.2.3.3. Thin section petrography. Analysis of petrographic thin sections of sample 14 under plain and crossed-polarized light indicated that clasts in the sample are fine-grained volcanics containing small microlites of quartz

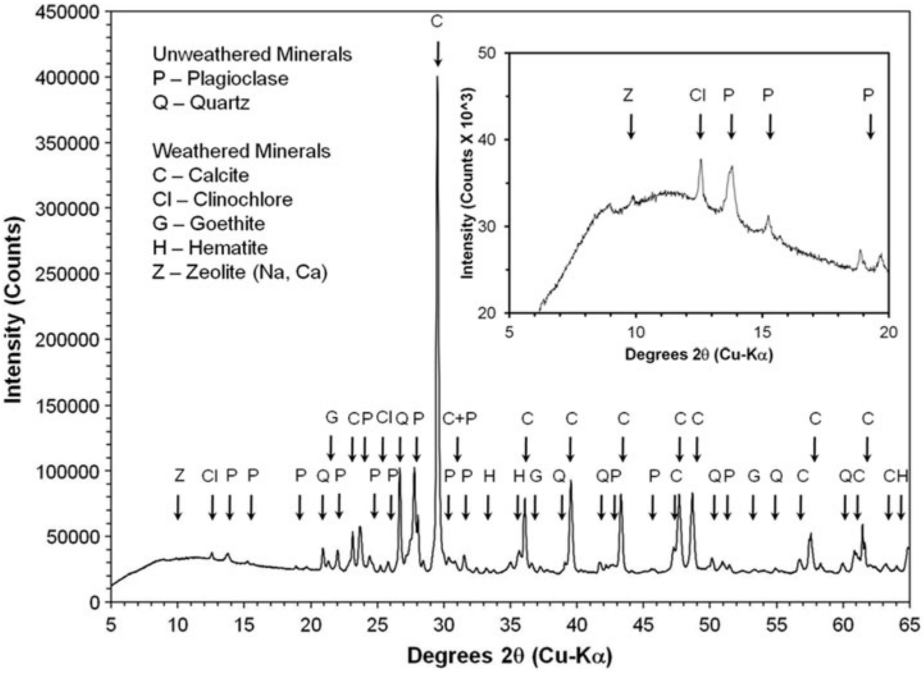

FIG. 17. X-ray powder diffractogram of bulk powder of sample 14. Mineral symbols on the peaks are calcite (C), clinochlore (Cl), goethite (G), hematite (H), plagioclase feldspar (P), quartz (Q), and calcium-sodium zeolite, *e.g.,* heulandite or stilbite (Z). Inset box zooms in on the small peaks within 5–20 degrees 2θ.

and plagioclase feldspar (Fig. 18). The feldspar microlites show a preferred orientation consistent with flow banding observed in hand samples. Volcaniclasts exhibit thin, dark brown to black, opaque coatings of iron oxide (interpreted to be hematite or goethite), which appear to be secondary alteration rinds. In contrast, the pore-filling iron oxide cement is translucent, with reddish brown to orange color, more consistent with lepidocrocite or possibly goethite (Fig. 18E and 18F). However, the color of all these phases in plain light can overlap, thus making it challenging to map specific iron oxides identified by XRD to the thin section.

To summarize, during paragenesis, the alteration history of sample 14 began with the development of dark brown, iron-oxide coatings or alteration rinds on the volcanic clasts following explosive fragmentation and deposition. This was followed by an initial cementation event (Fig. 18E and 18F), which introduced a finely crystalline, low birefringence mineral of low optical relief, probably zeolite(s) (*e.g.,* stilbite, or heulandite, both of which commonly exhibit sheaflike crystal forms, consistent with what is seen in thin section) and calcite microspar (identification based on high optical relief and third-order birefringence) into pore spaces. Finally, this was followed by the introduction of a reddish-brown, translucent iron oxyhydroxide (consistent with either goethite or lepidocrocite), which completely filled the remaining pore spaces. During the period of cementation, volcanic clasts were further altered, with volcanic glass undergoing crystallization (to quartz and feldspar), and feldspars altering to clays (kaolinite and Fe-Mg smectite) and other fine-grained phyllosilicates. This paragenesis is consistent with previously published studies of the Bishop Tuff, the source for sample 14. This formation was deposited as a series of pyroclastic flow eruptions (ignimbrites), which preceded the formation of the Long Valley caldera (Bailey, 1976). Emplacement was followed by significant fumarolic alteration.

5.3. Basaltic volcanic breccia (Sample 10)

Sample 10 was collected (by J.D.F.) from Hlöðufell, a Pleistocene tuya (subglacial) volcano located about 10 km southwest of Langjökull in central Iceland. Analysis with the use of laboratory techniques (see Section 5.3.3) showed that the sample is a palagonitized, basaltic breccia composed of subangular to subrounded basaltic clasts, cemented by Fe oxides, zeolites, and Fe smectite.

5.3.1. MMI images and spectra with comparison to convolved library spectra

Figure 19 shows MMI color composite images of sample 10, along with a corresponding spectral endmember map generated based on ROIs as input parameters. Spectra for these compositional endmembers are shown in Fig. 20 along with matching library spectra (see Table A1 for specific library spectra) convolved to the MMI bandpasses (see Table 1). Table 4 provides a summary of endmember spectral features, along with corresponding rock/mineral library matches.

Analysis of the MMI images showed that the sample consists of a poorly sorted mixture of black, fine-grained clasts, with subangular to rounded clasts (roundness values 0.5–0.9) and clast sphericities ranging from 0.7 to 0.9 (see Powers, 1953). A pervasive cement is present that includes orange, light gray, and white components (visible color image, Fig. 19) having patchy distributions. Clasts are very fine-grained and do not show internal fabrics, such as vesicularity, banding, or other features. All clasts appear to be of similar composition (*i.e.,* monolithologic), ranging in size from medium sand (0.25 mm) to medium pebbles (10 mm), with the small to medium pebble-size fraction dominating the sample. Cements are very fine-grained and were early (precompactional), filling large primary pore spaces between clasts. The light gray cement component appears to line clast surfaces, while the white and orange-colored cements mostly fill the interior pore spaces. The granule-sized dark clast in the

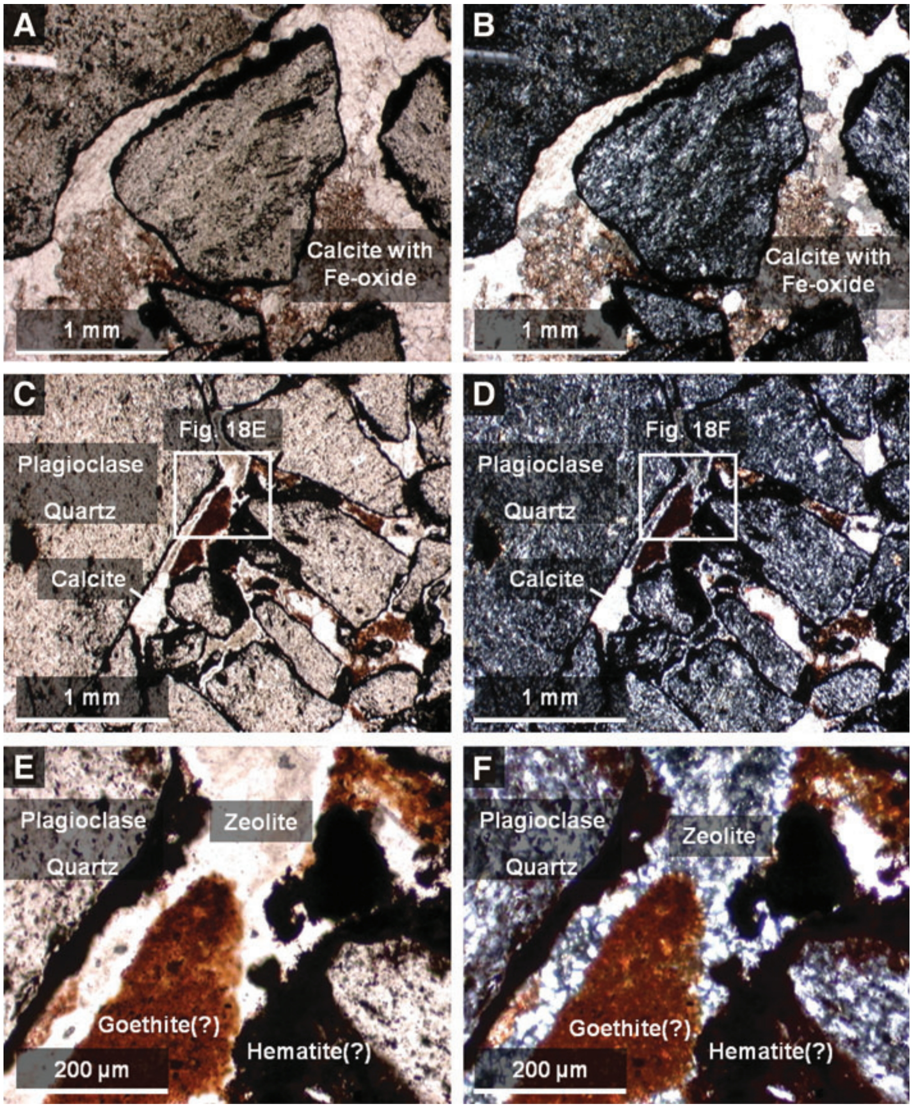

FIG. 18. Plain light (left) and crossed-polarized light (right) images of magnified areas of thin section of sample 14 obtained with a Nikon Eclipse E600 polarizing microscope targeting main elements with matrix components labeled. These include clasts (**A** and **B**) and matrix cements (**C** and **D**). (**E** and **F**) are close-ups of (C and D) to show the cross-cutting relationships of the cements to the clasts in better detail. The crossed-polarized images are slightly overexposed to bring out color variations between the dark Fe-bearing cements. Color images available online at www.liebertonline.com/ast

middle of the sample exhibits a distinctive, gray-colored rind not observed in neighboring clasts (spot B in Fig. 21).

Spectral analysis of the MMI images revealed the presence of eight spectral endmembers associated with sample 10 (Figs. 19 and 20). Two of these spectral endmembers are associated with the clasts and six with the matrix.

The dominant compositional endmember, mapped as blue, is associated with the fine-grained matrix of the clasts. The spectrum exhibits a low reflectance, flat shape, with a weak absorption at 1.05 μm. Compared to library spectra, the spectrum is consistent with basalt. The weak absorption at 1.05 μm may be due to the presence of high-Ca clinopyroxene or olivine.

The spectral endmember mapped as purple is associated with the granule-sized central clast located in the middle of the image (Fig. 19). The spectrum has a broad absorption centered between 0.97 and 1.05 μm with a 0.97 μm shoulder (centered at 1.05 μm, with 0.97 μm shoulder for continuum-removed) and a weak absorption at 1.43 μm. The spectrum compares best with the library spectrum for high-Ca clinopyroxene (best match is with augite). The 1.43 μm absorption is most likely a contribution from a hydrated mineral phase, such as hydrated glass, opaline silica, or zeolite, mixed with the fine-grained pyroxene. The unique alteration rind seen in this clast and apparent compositional differences suggests this clast may be from a different population and experienced a different diagenetic history.

The spectral endmember mapped as magenta is associated with the light gray cement component in the visible-color image (Fig. 19). This endmember primarily occurs as a pore-lining cement between clasts. The spectrum has a positive slope in the visible, a broad peak at 0.76 μm, a negative slope in the infrared, and absorptions centered between 0.97 and 1.05 μm and encompassing the 1.43 and 1.52 μm channels. The absorption including the 0.97 and 1.05 μm channels is consistent with the absorption in the purple spectrum for pyroxene, consistent with augite. The broad 1.43 and 1.52 μm absorption is consistent with a hydrated mineral such as a zeolite, like natrolite, or hydrated sulfate, like gypsum or kieserite.

The spectral endmember mapped as brown is associated with some of the white-colored cement in the visible-color image (Fig. 19). The spectrum has a positive slope in the visible, a broad peak at 0.76 μm, a negative slope in the infrared, and absorptions centered between 0.97 and

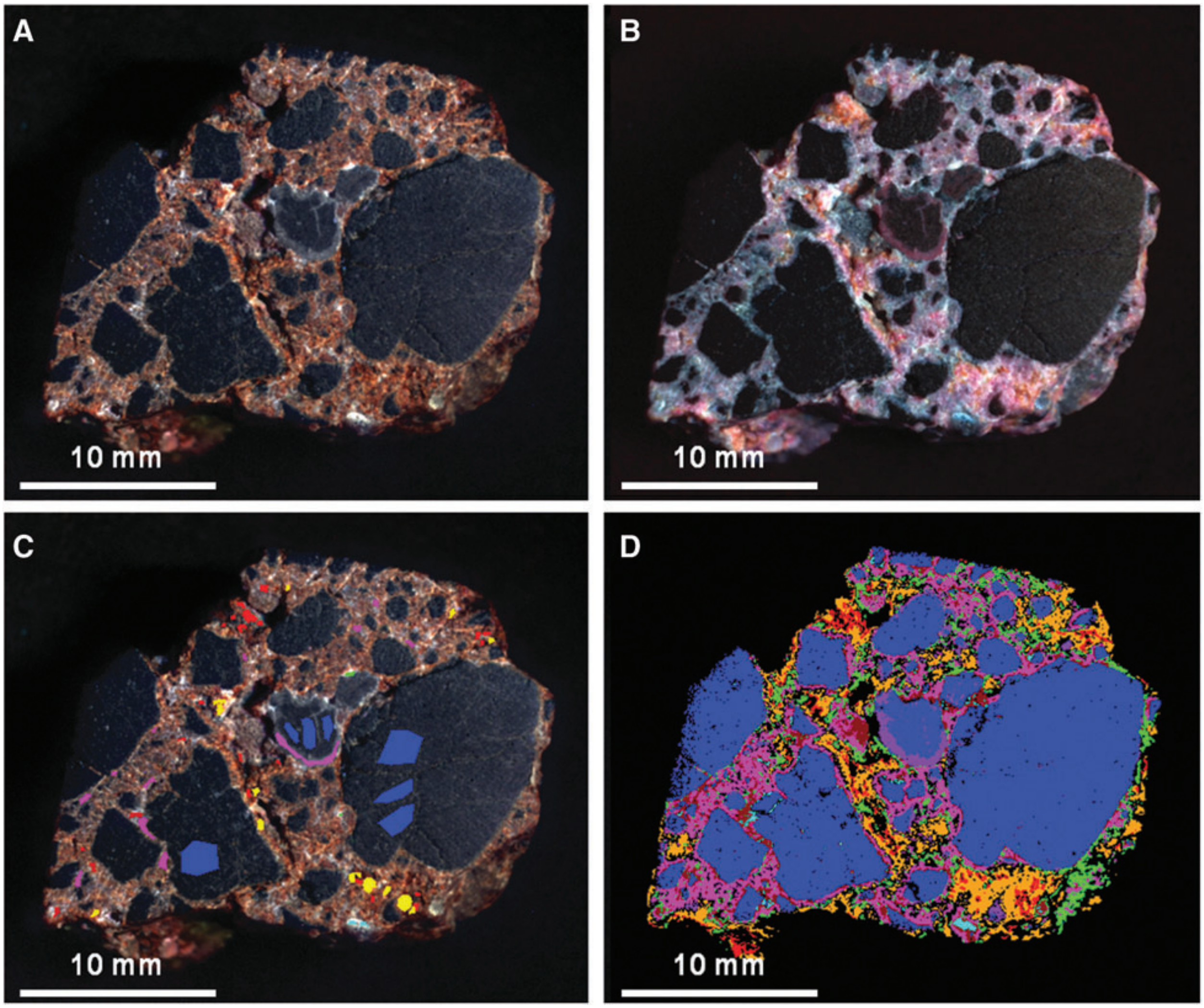

FIG. 19. MMI-generated color composite images and endmember map of sample 10. (**A**) Visible-color RGB composite image composed of MMI bands 0.64, 0.52, and 0.46 μm, respectively, to simulate natural color. (**B**) False-color RGB composite image composed of MMI bands 1.66, 0.97, and 0.76 μm, respectively, to bring out subtle color differences in materials due to variations in composition. (**C**) Visible-color RGB composite similar to (A) with ROIs used to generate endmember map (D) and corresponding endmember spectra (Fig. 19A and 19B). (**D**) Endmember map generated in ENVI by using supervised classification with ROIs as input parameters to map endmember distribution. Each MMI subframe image size is 30×25 mm at 62.5 μm/pixel. (A–C) are linear stretched.

1.05 μm and between the 1.43 and 1.52 μm channels. The spectrum is somewhat similar to the spectrum mapped as magenta (see above) but has a higher reflectance and a deeper absorption at 1.52 μm. Like the magenta spectral endmember, the absorption between the 0.97 and 1.05 μm channels is consistent with the spectrum for pyroxene (as augite). The broad 1.43 and 1.52 μm absorption is also consistent with a zeolite like natrolite or hydrated sulfate like gypsum or kieserite. The higher reflectance curve of the spectrum and shallower band depth of the 0.97 and 1.05 μm absorption suggests a lower pyroxene component.

The spectral endmember mapped in light blue is also associated with the white-colored cement (Fig. 19). The spectrum has a strong positive slope in the visible, a peak at 0.67 μm, a negative slope in the infrared, and absorptions at 0.97, 1.22 μm, and between 1.43 and 1.52 μm. Similar to the magenta and brown endmember spectra, the spectrum is consistent with a zeolite, like natrolite, or hydrated sulfate, like gypsum or kieserite. However, unlike the magenta and brown endmember spectra, the presence of the 0.97 and 1.22 μm absorptions, due to the $(2v1 + v3)$ and $(v1 + v2 + v3)$ combination and overtone bands for water (Herzberg, 1945; Hunt and Salisbury, 1970; Clark *et al.,* 1990), suggests an individual mineral phase with less mixing from other phases. Despite the additional information, it is not possible to distinguish further between these mineral phases within the current spectral range.

The spectral endmember mapped as green is also associated with the white-colored cement in the visible-color image (Fig. 19) but has a distinctly different spectrum from the other endmembers. The spectrum has a high reflectance with positive slope in the visible, a negative slope in the infrared, and absorptions at 0.97 and 1.43 μm. The spectrum is consistent with a hydrated silicate, such as a clay mineral (*e.g.,* montmorillonite), opaline silica, or zeolite (*e.g.,*

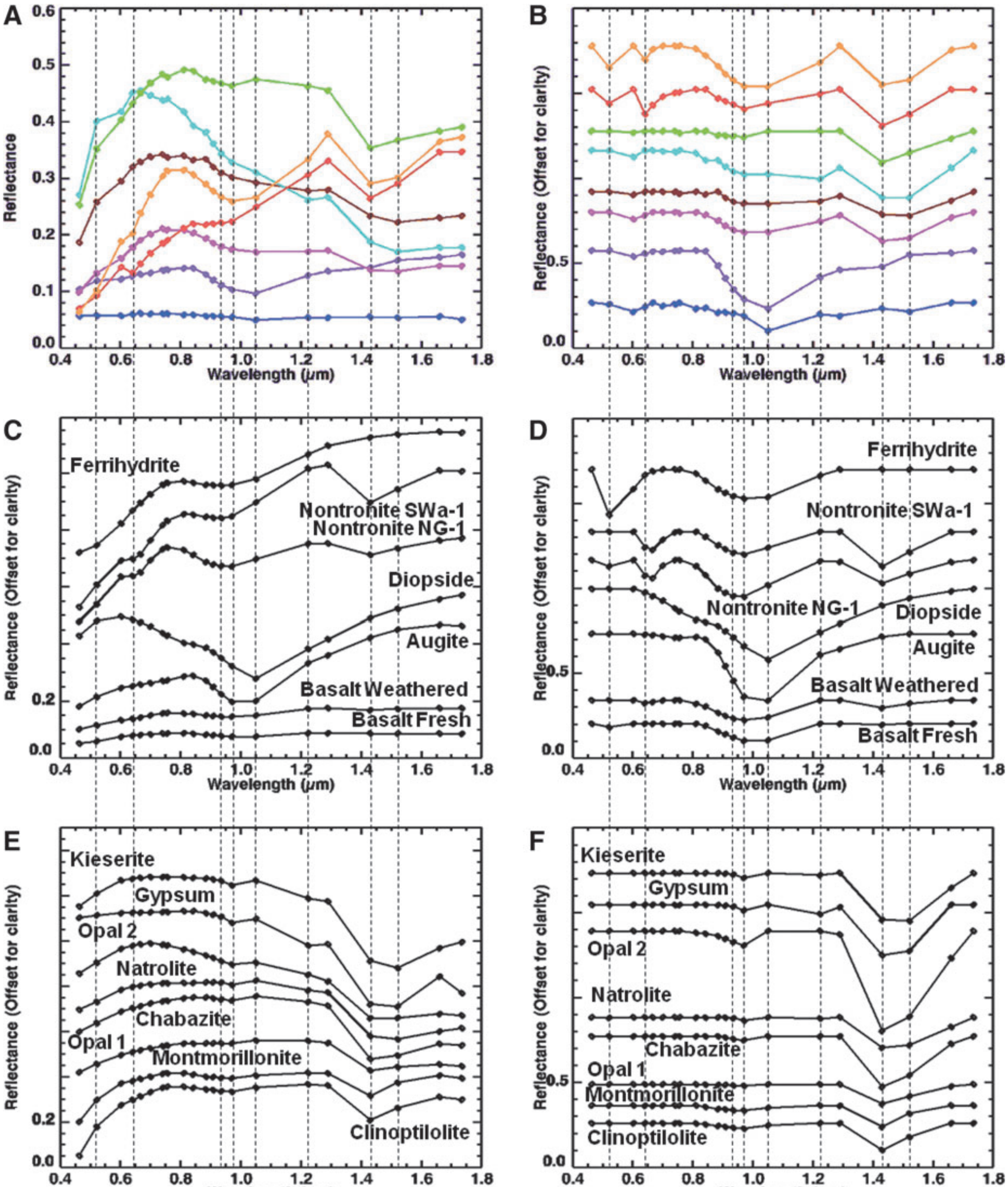

FIG. 20. Comparison of MMI-generated spectra of endmembers (**A** and **B**) from sample 10 (Fig. 19) and representative matching library spectra convolved to MMI bandpasses in Table 1 (**C–F**). Vertical lines correspond to MMI bands 0.52, 0.64, 0.94, 0.97, 1.05, 1.22, 1.43, and 1.52 μm. See text for details on features and discussion. Spectra on the left are normal, while spectra on the right are continuum-removed. Continuum-removed and library spectra are offset for clarity. For details on library spectra used, see Appendix A.

chabazite). Consistent with these minerals, the absorption at 1.43 μm is narrower than those of the other spectral endmembers, which encompass both the 1.43 and 1.52 μm channels. Thus, a match with a zeolite like natrolite or hydrated sulfate is unlikely. However, given that the distinguishing absorptions for phyllosilicates, opaline silica, and zeolites are outside the MMI spectral range, it is not possible to narrow the possibilities further.

The spectral endmember mapped as red is associated with the orange-colored cement in the visible-color image (Fig. 19). The spectrum has a positive slope, an absorption edge at 0.52 μm, peaks at 0.84 and 1.29 μm, and absorptions at 0.64,

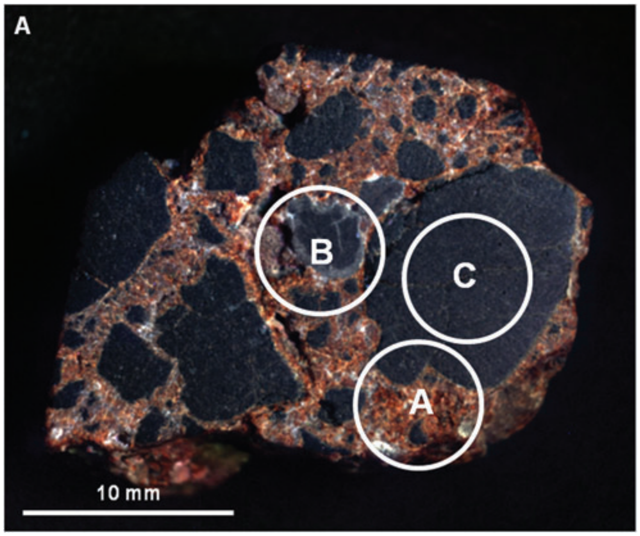

FIG. 21. Areas on sample 10 analyzed with VSWIR spectrometer. Visible-color, subframe image of sample 10 acquired by the MMI composed of bands RGB = 0.64, 0.52, 0.46 μm, respectively, to simulate natural color, with white circles (A–C) marking areas analyzed by the laboratory spectrometer (spectra are shown in Fig. 22). Image size is 30×25 mm at 62.5 μm/pixel. Spot size diameter is ~ 6 mm. Color images available online at www.liebertonline.com/ast

0.94, and 1.43 μm (0.64, 0.97, and 1.43 μm, respectively, for continuum-removed). The spectrum is consistent with the library spectrum for the Fe smectite, nontronite. Within the MMI wavelength range, nontronite exhibits absorptions at ~ 0.64 and ~ 0.95 μm due to Fe^{3+} and ~ 1.43 μm from OH-stretching overtones (Clark *et al.,* 1990; Bishop *et al.,* 2002c). When convolved to MMI bandpasses, nontronite retains all these spectral features, enabling it to be distinguished from other mineral spectra. The absorption edge at 0.52 μm and slope of the curve suggests that an additional minor component of fine-grained Fe oxide/hydroxide may also be present; however, it is possible that nontronite may also account for these features.

The last spectral endmember, mapped as orange, is also associated with the orange-colored cement (Fig. 19). The spectrum has a positive slope, an absorption edge at 0.52 μm, a peak from 0.76 to 0.81 μm, and absorptions at 0.64 μm, between 0.97 and 1.05 μm, and between 1.43 and 1.52 μm. The absorption edge at 0.52 μm and absorption at 0.64 μm are similar to that of the red endmember, while the broad absorptions encompassing the 0.97 and 1.05 μm channels, as well as the 1.43 and 1.52 μm channels, are similar to that of the magenta endmember. As a result, the orange endmember spectrum is interpreted to be a mixture of nontronite and other hydrated minerals, such as natrolite, pyroxene (best fit to augite), and Fe oxide/hydroxide. Compared to spectra in the published literature (*e.g.,* Warner and Farmer, 2010), the spectrum is consistent with palagonitized basalt. Palagonite is a heterogeneous material derived from aqueous alteration of basalt or basaltic glass. It has been defined in various ways in the literature with differing compositions and textures (Peacock, 1926; Moore, 1966; Thorseth *et al.,* 1991). Depending on the stage of alteration, its composition varies from hydrated Fe oxides in the early stages of alteration (typical of lower-temperature weathering) (Thorseth *et al.,* 1991; Bishop *et al.,* 2002c; Drief and Schiffman, 2004; Pokrovsky *et al.,* 2005) to Fe, Mg-rich clay minerals, zeolites, and hydrated silica for more advanced alteration at elevated temperature (Griffith and Shock, 1995; Bishop *et al.,* 2002c; Warner and Farmer, 2010).

5.3.2. Interpretation of MMI results

Analysis of the MMI images and spectra revealed that sample 10 is a basaltic volcanic breccia composed of volcaniclasts that were cemented by Fe oxides/hydroxides, hydrated silica, zeolites, and crystalline clays. The depositional context (subglacial volcanic setting) and composition of cements are consistent with palagonitization under low ($<100°$C) hydrothermal temperatures (*e.g.,* Warner and Farmer, 2010). Rounded-to-subangular clast shapes indicate moderate transport from the source, consistent with brecciation during eruption and subsequent subaqueous transport in the subglacial volcanic environment. The uniformity of clast textures and compositions (monolithologic) is consistent with derivation from a single volcanic source. However, there is evidence of minor mixing of clasts with a second population with alteration rinds enriched in hydrated silica (a common aqueous alteration product of basalt) and pyroxene or perhaps volcanic glass.

5.3.3. Laboratory observations of sample 10

5.3.3.1. Visible to shortwave infrared spectroscopy. Visible/shortwave infrared spectra were collected from three locations (A–C) on the surface of sample 10, targeting major compositional and microtextural components (Fig. 21). The sample and matching library spectra (see Table A1 for specific library spectra) are shown in Fig. 22. As with samples 14 and 17, because the ASD spot size is 6 mm in diameter, the spectra included more than one phase and fabric element.

Spot A on sample 10 (Fig. 22A and 22B) was centered on the orange-colored cement but also included some of the smaller dark-toned clasts. The spectrum exhibits an absorption at 1.0 μm (1.01 μm for continuum-removed), with narrower absorptions at 1.42, 1.91, and 2.29 μm and additional weak absorptions at 1.78 and 2.39 μm. Compared to library spectra, the absorption at 1.0 μm is attributed to augite. The other absorptions are consistent with the Fe smectite, nontronite (a common hydrothermal mineral).

Spot B on sample 10 (Fig. 22A and 22B) is centered on the rind of the central clast. The spectrum exhibits an absorption at 1.0 μm, a shoulder at 1.28 μm, and absorptions at 1.95 and 2.27 μm. Compared to library spectra, the 1.0 μm feature is consistent with the mineral augite. Similar to sample 17, the 1.28 μm feature is attributed to fine-grained olivine in the matrix of the volcanic clasts. The absorptions at 1.95 and 2.27 μm are consistent with hydration features, such as hydrated basaltic glass (Milliken *et al.,* 2008); however, precise mineral identification cannot be made based on the available data. The 2.27 μm absorption may also be consistent with the hydrated iron sulfate, jarosite; however, this absorption is commonly sharper (see Fig. 4) than what is observed in the sample spectrum.

Spot C on sample 10 (Fig. 22A and 22B) was centered on the largest dark-toned clast in the image. The flat spectrum has relatively low reflectance, with a weak absorption at 1.0 μm (1.01 μm for continuum-removed), consistent with

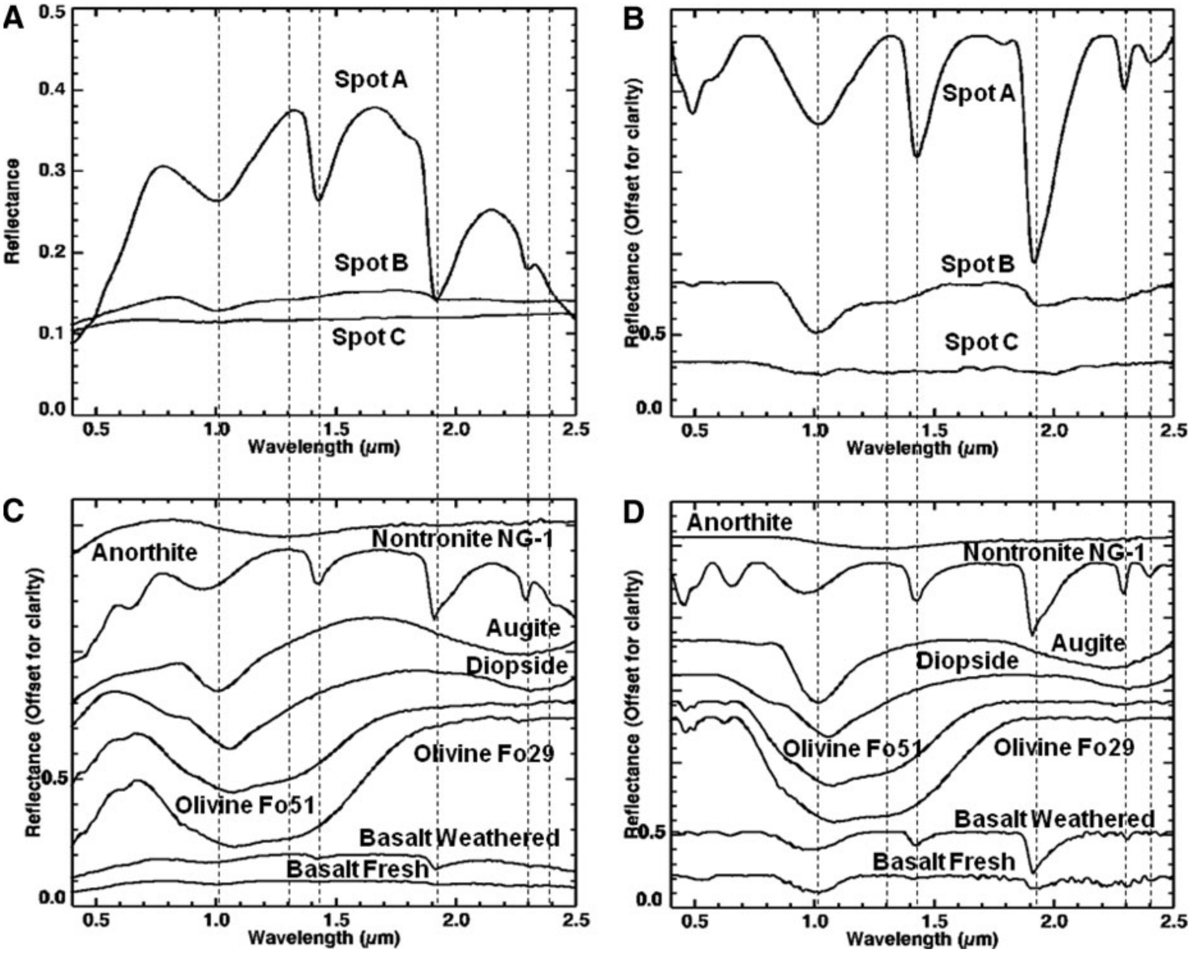

FIG. 22. Comparison of VSWIR spectra (**A** and **B**) collected from spots (A–C) on sample 10 (Fig. 21) with laboratory spectrometer and representative matching library spectra (**C** and **D**). Vertical lines correspond to features at 1.01, 1.28, 1.42, 1.91, 2.29, and 2.39 μm. See text for details on features and discussion. Spectra on the left are normal, while spectra on the right are continuum-removed. Continuum-removed and library spectra are offset for clarity. For details on library spectra used, see Appendix A.

the library spectrum for basalt. The 1.0 μm absorption is best matched with augite.

5.3.3.2. X-ray diffraction. X-ray diffraction of powdered bulk material from sample 10 showed maximum 2θ intensity peaks for the Ca-Na zeolite chabazite at 9.64° and 20.68°, for pyroxene (best fit to high-Ca clinopyroxene) at 29.95°, for olivine at 36.11°, for Ca-rich plagioclase feldspar (best fit to anorthite) at 27.91°, and for nontronite at 6.38° (Fig. 23). There is a significant background intensity attributed to nanophase Fe oxides/hydroxides (Moore and Reynolds, 1997). Such amorphous materials are common alteration products of basaltic glass and are difficult to analyze via standard XRD methods (Bishop *et al.,* 2002c; Warner and Farmer, 2010). The 2θ peaks are consistent with both primary basaltic minerals (*e.g.,* pyroxene, plagioclase feldspar, and olivine), along with secondary alteration minerals and cements (*e.g.,* zeolite and clay minerals).

5.3.3.3. Thin section petrography. Analysis of petrographic thin sections of sample 10 under plain and crossed-polarized light revealed subangular to rounded basaltic clasts, consisting of predominantly small phenocrysts of plagioclase feldspar and pyroxene, in a fine-grained, glassy groundmass containing microlites of plagioclase feldspar and pyroxene (Fig. 24). In thin section, clast surfaces showed a distinctive coloration that was only visible in plain light, due to the glassy matrix being lighter in color. In the case of the small clasts, this distinctive coloration of the matrix encompassed the entire clast (Fig. 24). While the color variations within clasts may be due to alteration, there was no visible evidence for alteration of the plagioclase feldspar or pyroxene phenocrysts (Fig. 24). This suggests that alteration, if it occurred, was limited to the glassy matrix. Alteration of the clasts is evident in thin, but pervasive, coatings of a yellow-green, fibrous mineral herein inferred to be nontronite. The fibrous mineral appears to be encased in a colorless mineral of low optical relief (possibly a zeolite) and in some locations by fine-grained, amorphous iron oxide/hydroxide (Fig. 24). In the areas between the clasts, zeolite-like minerals dominate as void-filling cement, with nontronite being present in central areas of filled pores. The undercompacted texture of the rock, limited clast alteration, and overlapping paragenesis is consistent with very early cementation of clasts

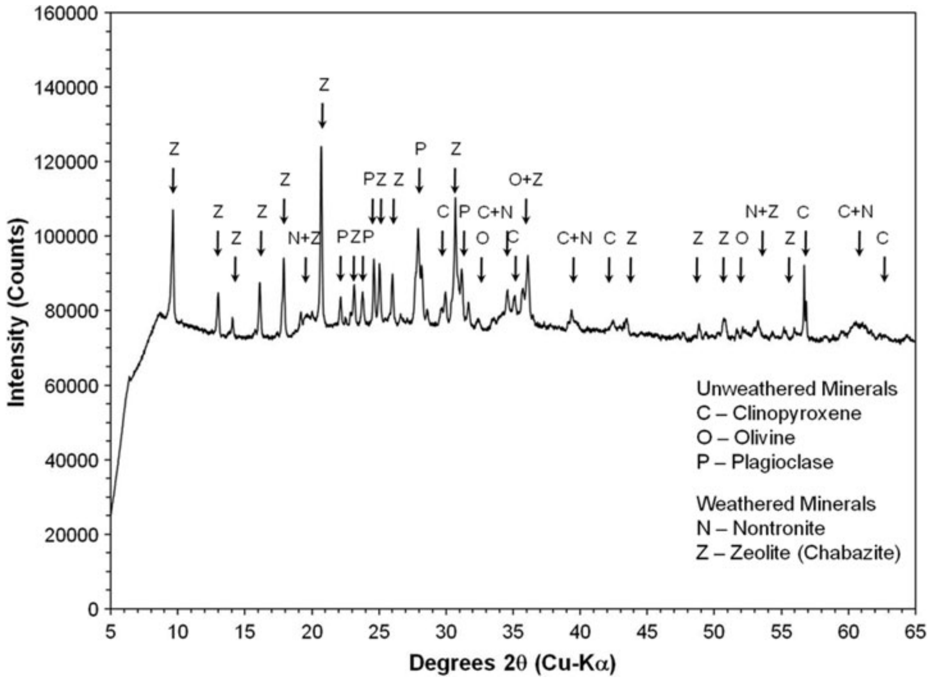

FIG. 23. X-ray powder diffractogram of bulk powder of sample 10. Mineral symbols on the peaks are clinopyroxene (C), nontronite (N), olivine (O), plagioclase feldspar (P), and zeolite, best match to chabazite (Z). Significant background intensity is related to amorphous and/or nanophase Fe hydroxides (Moore and Reynolds, 1997), which are common alteration products of basaltic glass and are difficult to analyze via standard XRD methods (Bishop *et al.,* 2002c).

and rapid cement precipitation from silica- and iron- rich hydrothermal fluids (Warner and Farmer, 2010).

6. Discussion

6.1. Comparison of MMI results to conventional laboratory techniques

6.1.1. Vesicular basalt (sample 17). Sample 17 provided an excellent example for testing the performance of the MMI with Mars-relevant igneous rocks of mafic composition and for identifying the strengths and weaknesses of the instrument configuration used. Overall, MMI results were consistent with the laboratory results. The MMI images faithfully resolved the major microtextural features of the sample (down to 200 μm; *i.e.,* at least 3 pixels), while the application of spectral endmember mapping revealed consistent spatial-temporal (paragenetic) relationships between all major spectral (*i.e.,* mineralogical) components (see Table 5). MMI spectra were most useful in discriminating between major and minor phases with diagnostic absorptions due to Fe^{2+} in pyroxene and olivine, between 0.9 and 1.0 μm, and those associated with plagioclase feldspars, between 1.2 and 1.3 μm (Clark *et al.,* 1990; Burns, 1993). These minerals were also identified in laboratory VSWIR spectra (Fig. 9), by XRD (Fig. 10), and in thin section petrography (Fig. 11), supporting the MMI-based interpretations (see Table 5). In addition, the MMI was also able to detect compositional zonation within some of the larger pyroxene and olivine phenocrysts, indicating the discontinuous reaction of olivine replacement by pyroxene during crystallization (Fig. 6), which seems to be recorded in a change in the curvature and width of the 1.05 μm absorption feature (Fig. 7). Interestingly, while the laboratory VSWIR observation of the largest zoned phenocryst in the MMI image was consistent with olivine (Fig. 9), the pyroxene component identified by the MMI observation, owing to the higher spatial resolution, could not be detected in the laboratory spectrum due to the coarse spatial resolution of the spot spectrometer used. This highlights some of the advantages of the higher spatial resolution of the MMI over traditional methods with coarser spatial resolution.

The identification of the matrix (*i.e.,* groundmass) in sample 17 proved to be challenging because of the fine grain size (each mineral grain < pixel size of 62.5 μm), which resulted in a nonlinear composite spectrum for each pixel. However, the flat spectrum, with a weak absorption at 1.05 μm, was positively matched to the library spectrum for basalt, where the 1.05 μm absorption is consistent with the presence of high-Ca pyroxene and/or olivine microphenocrysts. These phases were identified in thin section and by VSWIR and XRD due to higher spectral resolution. At the moment, the MMI cannot reliably spectrally differentiate between high-Ca clinopyroxene and olivine with the current channel configuration when looking at small, mixed phases, as in the example of the basalt matrix, due to the lack of a 1.0 μm channel. This gap in the instrument's capability would be remedied with the addition of a spectral channel at 1.0 μm in addition to the present channel at 1.05 μm.

6.1.2. Silicic volcanic breccia (sample 14). Sample 14 also provided a good test of MMI performance by highlighting additional strengths and weaknesses of the instrument. Overall, MMI results were consistent with laboratory analyses (see Table 5). The MMI images faithfully resolved the major microtextural features of the sample, while the application of spectral endmember mapping revealed the spatial distribution of most major mineral components (see below for phases not identified). The MMI was most effective in discriminating major and minor phases with diagnostic absorptions due to Fe^{3+} at ~ 0.9 μm (associated with iron oxides and oxyhydroxides such as hematite and goethite) and H_2O at ~ 1.4 μm (due to hydrated minerals). The presence of these phases was confirmed by laboratory VSWIR spectroscopy (Figs. 15 and 16) and by XRD (Fig. 17),

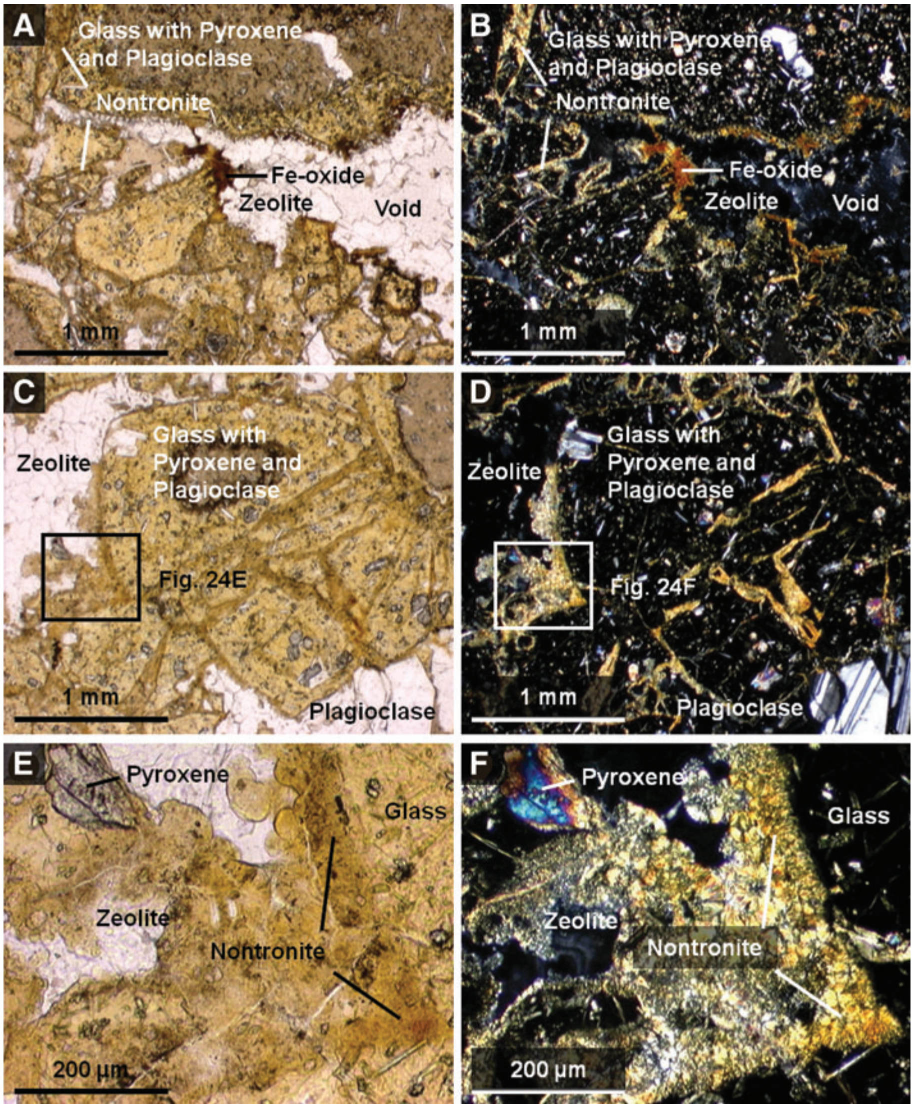

FIG. 24. Plain light (left) and crossed-polarized light (right) images of magnified areas of thin section of sample 10 obtained with a Nikon Eclipse E600 polarizing microscope targeting main elements with matrix components labeled. These include matrix cements and clasts **(A–D)**. (**E** and **F**) are close-ups of (**C** and **D**) to show the cross-cutting relationships of the cements to the clasts. The crossed-polarized images are slightly overexposed to bring out color variations between the first-order colors of zeolites, and clasts' glass matrix. Color images available online at www.liebertonline.com/ast

supporting the MMI results. The MMI also mapped the locations of these minerals in the sample, accurately revealing paragenetic relationships, which were confirmed by petrographic thin section analysis (Fig. 18).

Where spectra lacked diagnostic absorptions, the microtextural information provided by the MMI images and the inferred paragenetic relationships of the spectral endmembers provided useful constraints for inferring the types of minerals that might be present. For example, the paragenesis of the blue spectral endmember clearly indicated it was a pore-filling cement, despite the lack of diagnostic absorptions. However, the lack of an absorption at the 1.43 μm channel, which would be consistent with a hydrated mineral, was useful for narrowing the list of candidate minerals to nonhydrated cements, like carbonates (*e.g.,* calcite), anhydrous evaporites (*e.g.,* anhydrite), or quartz. In the next analytical steps, laboratory analyses (including VSWIR, XRD, and petrography) clearly identified calcite as the cement (also see Table 5). Even though the spectral range of the MMI was unable to capture the paired absorptions at 2.3 and 2.5 μm indicative of calcite (see Figs. 4F, 5F, 15, and 16), the MMI data enabled reasonable hypotheses to be posed for testing at the next level, which were verified with XRD and VSWIR. Extending the spectral range to 2.5 μm and increasing the number of channels would clearly improve such constraints. However, engineering trade-offs would need to be considered for an arm-mounted instrument (see Section 6.2 for more discussion).

Identification of the fine-grained microphenocrysts and volcanic glass composing the groundmass of the clasts in sample 14 posed the greatest challenge for MMI spectral analysis. First, crystallites in the groundmass were smaller than the MMI pixel size of 62.5 μm, which resulted in a nonlinear composite spectrum for each pixel. The second challenge was that the minerals in the groundmass, ultimately identified as quartz and plagioclase feldspar by XRD and petrography, do not exhibit diagnostic absorptions within the VSWIR spectral range, which includes the wavelength range of the MMI (see Fig. 13, Table 5). However, similar to the calcite cement example (blue endmember), the microtextural and spectral information provided by endmember mapping of the clast matrix (yellow endmember) provided sufficient information for hypotheses to be tested at the next level. Comparison of the bulk spectrum for the clasts (yellow

Table 5. Mineral Phases Identified with the MMI and Laboratory Methods

Mineral phases identified	*MMI*	*VNIR/ SWIR*	*XRD*	*Thin section*
Vesicular basalt (sample 17)				
Olivine	+	+	+	+
Plagioclase feldspar	+	+	+	+
Pyroxene	+	+	+	+
Glass	−	−	−	+
Silicic volcanic breccia (sample 14)				
Plagioclase feldspar	−	−	+	+
Quartz	−	−	+	+
Calcite	−	+	+	+
Goethite	+	+	+	FeOx
Hematite	+	+	+	FeOx
Fe/Mg smectite	HM	+	−	−
Clinochlore	HM	+	+	−
Opal-A	HM	+	−	−
Zeolite	HM	+	+	+
Glass	−	−	−	+
Basaltic volcanic breccia (sample 10)				
Olivine	−	+	+	+
Plagioclase feldspar	−	−	+	+
Pyroxene	+	+	+	+
Fe oxides	+	+	−	+
Nontronite	+	+	+	+
Zeolite	HM	HM	+	+
Glass	−	−	−	+

\+ −, mineral phase detected.
HM, hydrated mineral.
FeOx, Fe-oxide mineral.

endmember) with library spectra suggested a potential match with rhyolite, based on the shape of the spectrum (Fig. 13). Also, the light-toned color of the clasts and absence of absorptions associated with Fe-bearing mafic minerals suggested a felsic to intermediate composition. However, in the absence of diagnostic absorption features, this was not a definitive conclusion. The composition of the clasts could only be confirmed later by laboratory analysis with XRD and thin section petrography (Table 5).

6.1.3. Basaltic volcanic breccia (sample 10). Sample 10 had been studied previously as an analogue for potentially habitable hydrothermal environments on Mars (Warner and Farmer, 2010) and was a particularly relevant lithology for testing the performance of the MMI. Overall, the MMI results for sample 10 compared quite favorably with laboratory results (Table 5). The MMI images faithfully resolved all major microtextural features of the sample, while the application of spectral endmember mapping successfully captured most of the major mineral components (except fine-grained olivine and plagioclase feldspar within the clast matrix) and their paragenetic relationships. Similar to samples 17 and 14, the MMI was most effective for detecting ferric and ferrous iron minerals, and hydrated minerals, including nontronite. These minerals were subsequently identified in the laboratory VSWIR spectra (Fig. 22) and by XRD (Fig. 23), directly supporting the MMI results (Table 5). In addition, the position and width of the 1.43 μm absorption in the endmember spectra (for samples 10 and 14) were valuable for constraining the composition of the cements. Thus, hydrated silicates, like chabazite or opal, which exhibit a narrow 1.43 μm absorption, could be distinguished from natrolite or gypsum, which exhibit a broader absorption that encompasses both the 1.43 and 1.52 μm channels.

Thin section petrography of sample 10 (Fig. 24) showed that spectral endmember maps prepared from MMI data provide a reliable basis for an initial interpretation of paragenesis for major microtextural types and mineralogy. At the spatial scale of the MMI (62.5 μm/pixel), interpretations were based predominantly on composite spectral signatures, such as the orange endmember, which was interpreted to be a mixture of nontronite, pyroxene, and zeolites (Fig. 20, Table 4). As a result, more refined relationships between cement types could not be reliably established. Yet the spatial correlation of these endmembers as predominantly pore-lining and/or pore-filling cements proved to be consistent with thin section observations. In some instances, the grain size was large enough that more resolved spectra were possible, as in the case of the red and green endmembers (Figs. 19D and 20), which enabled specific mineral phases, such as nontronite or zeolites, to be detected (Fig. 20, Table 4). Improving the spatial resolution from 62.5 to 30 μm/pixel, extending the spectral range to 2.5 μm, and increasing the number of channels would clearly improve the ability of the MMI to detect individual mineral grains to enable more refined paragenetic relationships between phases to be reliably made.

These observations serve to highlight some of the spatial and spectral limitations of the MMI instrument while also demonstrating the capabilities of the instrument to provide useful mineralogical information and interpretations of paragenesis (Table 5). The microtextural/compositional context provided by the MMI proved very useful in complementing information from the higher spectral resolution mineralogical methods of XRD and spot VSWIR.

6.2. Lessons learned

One of the lessons learned from these analyses involves consideration of the optimal spatial resolution of the MMI. Most geologists would agree that the hand lens analysis of fine-grained rocks poses the greatest challenge to petrogenetic analysis in the field. All samples presented in this paper revealed this grain size limitation for the MMI. At the present spatial resolution of 62.5 μm/pixel, aphanitic volcanic rocks (like basalt and rhyolite) and fine-grained sedimentary rocks (like siltstone or shale) or finely crystalline chemical sedimentary rocks, pose major challenges for the MMI, both in the visualization of microtextures and in the acquisition of interpretable VSWIR spectra. However, this is also an issue for other microimagers with spatial pixel size >5–10 μm. While the first inclination would be to increase the spatial resolution to the maximum attainable within a realistic depth of field and working distance, there are other considerations. Experience suggests that 30–70 μm/pixel resolution represents an optimum range for resolving a majority of microtextural types and lithologies (*i.e.,* fine sand or coarser; see, *e.g.,* Herkenhoff *et al.,* 2003). On the other hand, at a scale of 10 μm/pixel or less, it becomes much harder to define microtextural types, due to the reduced field of view. In essence, at 10 μm, one ''cannot see the forest from the trees.'' Inferring petrogenesis depends heavily on building a robust microtextural context, equivalent to the forest in this analogy. The 30–70 μm/pixel resolution window is considered a ''sweet spot'' for field-based microtextural analysis, building on more than a century of published petrogenetic observations as well as almost a decade of rover-based exploration of Mars (*e.g.,* Herkenhoff *et al.,* 2003). Of course, with variable magnification, a 10 μm capability might be useful for fine-grained rocks, so long as a flattened surface could be produced consistently to accommodate the smaller working distance.

Another lesson learned involves determining the optimum spectral range and resolution of the MMI. Hyperspectral imaging spectrometers such as TES on Mars Global Surveyor (Christensen *et al.,* 2001), OMEGA on Mars Express (Bibring *et al.,* 2004), and CRISM on Mars Reconnaissance Orbiter (Murchie *et al.,* 2007) have facilitated the discovery and mapping of a wide variety of igneous and aqueous minerals on Mars (*e.g.,* Bandfield *et al.,* 2000; Christensen *et al.,* 2001; Bibring *et al.,* 2005, 2006; Mustard *et al.,* 2008; Murchie *et al.,* 2009a, 2009b), owing to their broad range and high spectral resolution. In particular, studies in which OMEGA and CRISM data sets were used have discovered a wide variety of aqueous minerals on Mars from orbit, including carbonates, clays, sulfates, opaline silica, and zeolites, by identifying characteristic absorptions within the 1.0–2.6 μm range. The 2.1–2.5 μm range is especially useful for discriminating between clay minerals and carbonates, which exhibit sharp diagnostic absorptions within this wavelength range. As the examples presented in this paper highlight some of the limitations of the current MMI spectral coverage for detecting certain mineral phases, extending the spectral cutoff of the MMI from 1.8 to 2.5 μm would enable the detection of these minerals, even with a limited number of targeted broadband channels within the 2.1–2.5 μm range targeting specific mineral absorptions (*i.e.,* Swayze *et al.,* 2003). This has been demonstrated with CRISM parameter maps, where only a handful of wavelengths at key inflections or absorptions are used to map different mineral classes (Pelkey *et al.,* 2007). Additionally, future remote multispectral imagers for Mars have been proposed to map these different mineral types by using only 12 or more spectral filters within the 1.0–2.5 μm range (Murchie *et al.,* 2012). Thus, extending the spectral range of the MMI with only a certain number of key wavelengths would significantly enhance science return. However, extending the spectral range to 2.5 μm would require the use of a different detector (such as HgCdTe) and use of a thermoelectric cooler. These additions would increase the instrument mass and power consumption, which may potentially be cost-prohibitive for an arm-mounted instrument (depending on engineering requirements). As a result, scientific capabilities would need to be balanced against costs in mass and power consumption to identify the ''sweet spot.''

6.3. Applications to Mars exploration

Over the past decade of Mars exploration, observations by landed and orbital spacecraft have revealed a diverse mineralogical record of aqueous deposition and alteration, providing strong evidence for past habitable surface environments on Mars (*e.g.,* Christensen *et al.,* 2001, 2005; Squyres *et al.,* 2004, 2008; Bibring *et al.,* 2006; Murchie *et al.,* 2009a, 2009b). These investigations have now identified a number of aqueous mineral groups (*e.g.,* phyllosilicates, sulfates, Fe oxides, carbonates, halides, and hydrated silica) that indicate widespread water/rock interactions over a broad range of environmental conditions that, on Earth, support life (*e.g.,* Christensen *et al.,* 2001, 2005; Langevin *et al.,* 2005; Bibring *et al.,* 2006; Bishop *et al.,* 2008; Milliken *et al.,* 2008; Mustard *et al.,* 2008; Osterloo *et al.,* 2008; Poulet *et al.,* 2008; Ehlmann *et al.,* 2009; Ruff *et al.,* 2011). Many of these environments also appear to be favorable for the capture and long-term preservation of fossil biosignatures (Farmer, 1999; Farmer and Des Marais, 1999). The Planetary Decadal Survey for the decade 2013–2022 has recommended that the next Flagship mission should be a sample return campaign from Mars at the end of the decade (National Research Council, 2011). One concept for Mars sample return involves a three-step process that includes the landing of a caching rover at a high-priority astrobiological site to conduct detailed *in situ* scientific investigations, which could potentially be followed some time later by the return of the sample cache to Earth for analysis in terrestrial labs. A key requirement for mission success will be to identify and cache the best astrobiological samples at a site, where possibly hundreds may be present at a single location. The favored approach will be to employ a suite of rover-mounted (contact and remote sensing) instruments to identify the most favorable targets from a distance and then perform more definitive investigations with arm-mounted contact instruments and/or analyses in which onboard laboratory instruments are used before caching (MEPAG ND-SAG, 2008; MEPAG MRR-SAG, 2009; National Research Council, 2011). Critical capabilities for a caching rover include arm-mounted instruments that are capable of interrogating natural and abraded rock surfaces to create co-registered 2-D maps of microtexture, major element geochemistry, mineralogy, and organic geochemistry (MEPAG ND-SAG, 2008; MEPAG MRR-SAG, 2009; Beaty *et al.,* 2012; Mustard *et al.,* 2013). Such spatially correlated data sets are considered crucial for identifying the best candidate samples for caching, based on *in situ* petrogenetic interpretations for assessing past habitability and the potential for preserving biosignatures. The MMI, with its ability to create multispectral microimages and co-registered high resolution 2-D maps of microtexture with mineralogy as demonstrated with the examples presented in this paper, directly addresses many of the most important measurement requirements for a sample caching mission (MEPAG ND-SAG, 2008; MEPAG MRR-SAG, 2009; Beaty *et al.,* 2012; Mustard *et al.,* 2013); it is also clear that such capabilities would greatly enhance the success of *in situ* missions where sample selection is not for Mars sample return but for analysis with onboard lab instruments.

7. Future Work

Development of the MMI is ongoing. The next improvement will be to extend the spectral range to 2.5 μm and increase the number of spectral bands. As discussed in Section 6.2, these improvements would enhance the ability of the MMI to detect and distinguish between important aqueous mineral groups with diagnostic features in the 1.8–2.5 μm range. However, the added scientific capabilities gained by extending the spectral range will need to be balanced against the added costs arising from required increases in mass, power consumption, and data volume. The addition of a focus mechanism would also improve the spatial sampling from 62.5 μm/pixel to <40 μm/pixel. This improvement would enable the instrument to resolve individual grains and microtextural features as small as ~ 100 μm. At this scale, it will still not be possible to resolve small matrix minerals in fine-grained rocks or individual cellular structures, but this resolution would be sufficient to resolve most biologically mediated microfabrics (see Farmer, 1999). Furthermore, a spatial sampling of <40 μm/pixel would provide a reasonable compromise between fine spatial resolution, field of view, and depth of field. This compromise facilitates the imaging of natural, rough surfaces, while providing enough spatial coverage to recognize discrete microtextural elements for interpreting petrogenesis. At this scale, it is also possible to easily place MMI images within larger context images obtained from a mast-mounted camera. The optimization of scientific capabilities, against mass, power, and cost, will depend on future mission objectives and requirements. Thus, in preparation for future planetary surface missions, we will continue to optimize science-driven MMI performance, within evolving design trade space, budget, and advances in the technology of spectral microimaging.

8. Summary and Conclusions

The Multispectral Microscopic Imager (MMI) is a new microimager developed for future planetary surface missions. The MMI provides multispectral, microscale reflectance images of geological samples, where each image pixel is a VSWIR spectrum. The MMI advances beyond the capabilities of current microscopic imagers by extending the spectral range into the infrared and increasing the number of spectral bands. This paper reports the results of a multi-year study of the MMI capabilities involving the analysis of 20 analog samples, which were selected to represent Mars-relevant environments, including igneous and sedimentary rocks of interest to astrobiology. MMI data sets were used to obtain information about microtexture and mineralogy, and spectral endmembers were mapped to reveal the paragenetic relationships between minerals and microtextural elements composing rock samples. These observations were used as a basis for initial interpretations of petrogenesis. The same sample suite was studied in the laboratory with high-resolution VSWIR point spectroscopy, XRD, and thin section petrography to compare with MMI-based interpretations. The comparative study showed that the MMI can effectively resolve the fine-scale microtextural features of samples in color images down to a grain size of fine sand. In addition, the application of ENVI-based spectral endmember mapping successfully identified the distribution of Fe-bearing minerals (including silicates, oxides, and oxyhydroxides), as well as the identification and placement of hydrated minerals within a microtextural framework. Lab comparisons also served to highlight synergies with other analytical methods (*e.g.,* XRD, spot VSWIR spectroscopy) that lack spatial context and are likely to be included in payloads for future Mars missions. The results of this study demonstrate the value of the MMI for future *in situ*, rover-based exploration of Mars and the down-selection of martian samples for onboard astrobiological analysis and/or potential sample return(s).

Appendix A

Information on the mineral samples whose library spectra were used for identification of mineral phases in the MMI samples is given in Table A1.

Acknowledgments

Development of the MMI and analysis of MMI data sets were carried out at the Jet Propulsion Laboratory (JPL), California Institute of Technology, and at Arizona State University (ASU), under contracts with the National Aeronautics and Space Administration (NASA). Laboratory analysis of test samples was carried out at ASU and the U.S. Geological Survey (USGS) in Denver, Colorado. This research was supported by grants from NASA's Moon and Mars Analog Mission Activities (MMAMA) Program (2008; 2011–2012); the NASA Mars Instrument Development Program (MIDP; 2008–2010); the NASA-JPL Director's Discretionary Fund (2007–2008); and NASA's Astrobiology Science Technology Instrumentation Development (ASTID) Program (2005–2007). Support for J.I. Núñez was provided by a doctoral fellowship from the NASA Earth and Space Science Fellowship (NESSF) program, a Young Explorers Grant from the National Geographic Society (NGS), and a Lewis and Clark Fellowship in Astrobiology from the NASA Astrobiology Institute (NAI) and the American Philosophical Society (AMS). We are grateful to Charles Sarture, Paul Gardner, and Andrew Kieta at JPL for their assistance with development of the MMI, and Vicki Mills at ASU for assistance with preparation of test samples and preliminary analysis of XRD results. We also thank Neil Pearson and an anonymous reviewer for helpful reviews and comments that improved this manuscript.

Author Disclosure Statement

No competing financial interests exist.

Abbreviations

ASTER, Advanced Spaceborne Thermal Emission and Reflection Radiometer.
ENVI, Environment for Visualizing Images.
FOV, field of view.
FPA, focal plane array.
FWHM, full width at half maximum.
InGaAs, indium gallium arsenide.
LED, light-emitting diode.
MAHLI, Mars Hand Lens Imager.
MECA, Microscopy, Electrochemistry, and Conductivity Analyzer.
MERs, Mars Exploration Rovers.
MI, Microscopic Imager.
MMI, Multispectral Microscopic Imager.
MNF, Minimum Noise Fraction Transformation.
MSL, Mars Science Laboratory.

NIST, National Institute of Standards and Technology.
OM, Optical Microscope.
Pancam, Panoramic Camera.
PPI, Pixel Purity Index.
RAC, Robotic Arm Camera.
RELAB, Reflectance Experiment Laboratory.
ROIs, regions of interest.
SWIR, shortwave infrared.
USGS, U.S. Geological Survey.
VNIR, visible and near-infrared.
VSWIR, visible/shortwave infrared.
XRD, X-ray diffraction.

References

Adams, J.B. (1974) Visible and near-infrared diffuse reflectance spectra of pyroxenes as applied to remote sensing of solid objects in the Solar System. *J Geophys Res* 79:4829–4836.

Bailey, R.A., Dalrymple, G.B., and Lanphere, M.A. (1976) Volcanism, structure, and geochronology of Long Valley Caldera, Mono County, California. *J Geophys Res* 81:725–744.

Baldridge, A.M., Hook, S.J., Grove, C.I., and Rivera, G. (2009) The ASTER spectral library Version 2.0. *Remote Sens Environ* 113:711–715.

Bandfield, J.L., Hamilton, V.E., and Christensen, P.R. (2000) A global view of martian surface compositions from MGS-TES. *Science* 287:1626–1630.

Beaty, D.W., Allwood, A.C., Bass, D.S., Feldman, S., and the 2011 NASA-ESA JSWG Team. (2012) An analysis of the instruments needed to carry out the function of identifying and documenting the samples for potential return to Earth via MSR [abstract 1147]. In *International Workshop on Instrumentation for Planetary Missions,* Goddard Space Flight Center, Greenbelt, MD.

Bell, J.F., III, McCord, T.B., and Owensby, P.D. (1990) Observational evidence of crystalline iron oxides on Mars. *J Geophys Res* 95:14447–14461.

Bell, J.F., III, McSween, H.Y., Jr., Crisp, J.A., Morris, R.V., Murchie, S.L., Bridges, N.T., Johnson, J.R., Britt, D.T., Golombek, M.P., Moore, H.J., Ghosh, A., Bishop, J.L., Anderson, R.C., Brückner, J., Economou, T., Greenwood, J.P., Gunnlaugsson, H.P., Hargraves, R.M., Hviid, M.S., Knudsen, J.M., Madsen, M.B., Reid, R., Rieder, R., and Soderblom, L. (2000) Mineralogic and compositional properties of martian soil and dust: results from Mars Pathfinder. *J Geophys Res* 105:1721–1755.

Bell, J.F., III, Squyres, S.W., Herkenhoff, K.E., Maki, J.N., Arneson, H.M., Brown, D., Collins, S.A., Dingizian, A., Elliot, S.T., Hagerott, E.C., Hayes, A.G., Johnson, M.J., Johnson, J.R., Joseph, J., Kinch, K., Lemmon, M.T., Morris, R.V., Scherr, L., Schwochert, M., Shepard, M.K., Smith, G.H., Sohl-Dickstein, J.N., Sullivan, R.J., Sullivan, W.T., and Wadsworth, M. (2003) Mars Exploration Rover Athena Panoramic Camera (Pancam) investigation. *J Geophys Res* 108, doi:10.1029/2003JE002070.

Bell, J.F., III, Malin, M.C., Caplinger, M.A., Ravine, M.A., Godber, A.S., Jungers, M.C., Rice, M.S., and Anderson, R.B. (2012) Mastcam multispectral imaging on the Mars Science Laboratory Rover: wavelength coverage and imaging strategies at the Gale Crater field site [abstract 2541]. In *43rd Lunar and Planetary Science Conference Abstracts,* Lunar and Planetary Institute, Houston.

Bibring, J.-P., Soufflot, A., Berthé, M., Langevin, Y., Gondet, B., Drossart, P., Bouyé, M., Combes, M., Puget, P., Semery, A., Bellucci, G., Formisano, V., Moroz, V., Kottsov, V., and the OMEGA Co-I Team. (2004) OMEGA: Observatoire pour la Mineralogie, l'Eau, les Glaces et l'Activité. In *Mars Express: The Scientific Payload,* edited by A. Wilson, ESA-SP 1240, ESA Publications Division, Noordwijk, the Netherlands, pp 37–49.

Bibring, J.-P., Langevin, Y., Gendrin, A., Gondet, B., Poulet, F., Berthé, M., Soufflot, A., Arvidson, R., Mangold, N., Mustard, J., Drossart, P., and the OMEGA Team. (2005) Mars surface diversity as revealed by the OMEGA/Mars Express observations. *Science* 307:1576–1581.

Bibring, J.-P., Langevin, Y., Mustard, J.F., Poulet, F., Arvidson, R., Gendrin, A., Gondet, B., Mangold, N., Pinet, P., Forget, F., and the OMEGA Team. (2006) Global mineralogical and aqueous Mars history derived from OMEGA/Mars Express data. *Science* 312:400–404.

Bishop, J.L., Pieters, C.M., and Edwards, J.O. (1994) Infrared spectroscopic analyses on the nature of water in montmorillonite. *Clays Clay Miner* 42:701–715.

Bishop, J., Madejova, J., Komadel, P., and Froschl, H. (2002a) The influence of structural Fe, Al, and Mg on the infrared OH bands in spectra of dioctahedral 37 smectites. *Clay Miner* 37:607–616.

Bishop, J., Murad, E., and Dyar, M.D. (2002b) The influence of octahedral and tetrahedral cation substitution on the structure of smectites and serpentines as observed through infrared spectroscopy. *Clay Miner* 37:617–628.

Bishop, J.L., Schiffman, P., and Southard, R. (2002c) Geochemical and mineralogical analyses of palagonitic tuffs and altered rinds of pillow basalts in Iceland and applications to Mars. In *Volcano-Ice Interaction on Earth and Mars,* Geological Society of London Special Publication 202, edited by J.L. Smellie and M.G. Chapman, Geological Society, London, pp 371–392.

Bishop, J.L., Lane, M.D., Dyar, M.D., and Brown, A.J. (2008) Reflectance and emission spectroscopy study of four groups of phyllosilicates: smectites, kaolinite-serpentines, chlorites and micas. *Clay Miner* 43:35–54.

Burns, R.G. (1970) Crystal field spectra and evidence of cation ordering in olivine minerals. *American Mineralogist* 55:1608–1632.

Burns, R.G. (1993) *Mineralogical Applications of Crystal Field Theory,* Cambridge University Press, New York.

Christensen, P.R., Bandfield, J.L., Smith, M.D., Hamilton, V.E., and Clark, R.N. (2000) Identification of a basaltic component on the martian surface from Thermal Emission Spectrometer data. *J Geophys Res* 105:9609–9621.

Christensen, P.R., Bandfield, J.L., Hamilton, V.E., Ruff, S.W., Kieffer, H.H., Titus, T.N., Malin, M.C., Morris, R.V., Lane, M.D., Clark, R.L., Jakosky, B.M., Mellon, M.T., Pearl, J.C., Conrath, B.J., Smith, M.D., Clancy, R.T., Kuzmin, R.O., Roush, T., Mehall, G.L., Gorelick, N., Bender, K., Murray, K., Dason, S., Greene, E., Silverman, S., and Greenfield, M. (2001) Mars Global Surveyor Thermal Emission Spectrometer experiment: investigation, description, and surface science results. *J Geophys Res* 106:23823–23871.

Christensen, P.R., Ruff, S.W., Fergason, R., Gorelick, N., Jakosky, B.M., Lane, M.D., McEwen, A.S., McSween, H.Y., Mehall, G.L., Milam, K., Moersch, J.E., Pelkey, S.M., Rogers, A.D., and Wyatt, M.B. (2005) Mars Exploration Rover candidate landing sites as viewed by THEMIS. *Icarus* 176:12–43.

Clark, R.N. (1999) Spectroscopy of rocks and minerals and principles of spectroscopy. In *Remote Sensing for the Earth*

Sciences, Vol. 3, edited by A.N. Rencz and R.R. Ryerson, John Wiley, New York, pp 3–58.

Clark, R.N. and Roush, T.L. (1984) Reflectance spectroscopy: quantitative analysis techniques for remote sensing applications. *J Geophys Res* 89:6329–6340.

Clark, R.N., King, T.V.V., Klejwa, M., and Swayze, G.A. (1990) High spectral resolution reflectance spectroscopy of minerals. *J Geophys Res* 95:12653–12680.

Clark, R.N., Swayze, G.A., Livo, K.E., Kokaly, R.F., Sutley, S.J., Dalton, J.B., McDougal, R.R., and Gent, C.A. (2003) Imaging spectroscopy: Earth and planetary remote sensing with the USGS Tetracorder and expert systems. *J Geophys Res* 108, doi:10.1029/2002JE001847.

Clark, R.N., Swayze, G.A., Wise, R., Livo, E., Hoefen, T., Kokaly, R., and Sutley, S.J. (2007) *USGS Digital Spectral Library splib06a,* Digital Data Series 231, U.S. Geological Survey, Reston, VA.

Cloutis, E.A., Gaffey, M.J., Jackowski, T.L., and Reed, K.L. (1986) Calibrations of phase abundance, composition, and particle size distribution for olivine-orthopyroxene mixtures from reflectance spectra. *J Geophys Res* 91:11641–11653.

Cloutis, E.A., Asher, P.M., and Mertzman, S.A. (2002) Spectral reflectance properties of zeolites and remote sensing implications. *J Geophys Res* 107, doi:10.1029/2000JE001467.

Cloutis, E.A., Hawthorne, F.C., Mertzman, S.A., Krenn, K., Craig, M.A., Marcino, D., Methot, M., Strong, J., Mustard, J.F., Blaney, D.L., Bell, J.F., III, and Vilas, F. (2006) Detection and discrimination of sulfate minerals using reflectance spectroscopy. *Icarus* 184:121–157.

Cornell, R.M. and Schwertmann, U. (1996) *The Iron Oxides,* John Wiley, Hoboken, NJ.

Des Marais, D.J., Nuth, J.A., III, Allanmandola, L.J., Boss, A.P., Farmer, J.D., Hoehler, T.M., Jakosky, B.M., Meadows, V.S., Pohorille, A., Runnegar, B., and Spormann, A.M. (2008) The NASA Astrobiology Roadmap. *Astrobiology* 8:715–730.

Drief, A. and Schiffman, P. (2004) Very low-temperature alteration of sideromelane in hyaloclastites and hyalotuffs from Kilauea and Mauna Kea volcanoes: implications for the mechanism of palagonite formation. *Clays Clay Miner* 52:622–634.

Edgett, K.S., Ravine, M.A., Caplinger, M.A., Ghaemi, F.T., Schaffner, J.A., Malin, M.C., Baker, J.M., DiBiase, D.R., Laramee, J., Maki, J.N., Willson, R.G., Bell, J.F., III, Cameron, J.F., Dietrich, W.E., Edwards, L.J., Hallet, B., Herkenhoff, K.E., Heydari, E., Kah, L.C., Lemmon, M.T., Minitti, M.E., Olson, T.S., Parker, T.J., Rowland, S.K., Schieber, J., Sullivan, R.J., Sumner, D.Y., Thomas, P.C., and Yingst, R.A. (2009) The Mars Science Laboratory (MSL) Mars Hand Lens Imager (MAHLI) Flight Instrument [abstract 1197]. In *40th Lunar and Planetary Science Conference Abstracts,* Lunar and Planetary Institute, Houston.

Ehlmann, B.L., Mustard, J.F., Swayze, G.A., Clark, R.N., Bishop, J.L., Poulet, F., Des Marais, D.J., Roach, L.H., Milliken, R.E., Wray, J.J., Barnouin-Jha, O., and Murchie, S.L. (2009) Identification of hydrated silicate minerals on Mars using MRO-CRISM: geologic context near Nili Fossae and implications for aqueous alteration. *J Geophys Res* 114, doi:10.1029/2009JE003339.

Farmer, J.D. (1999) Taphonomic modes in microbial fossilization. In *Size Limits of Very Small Microorganisms: Proceedings of a Workshop,* National Research Council, The National Academies Press, Washington, DC, pp 94–102.

Farmer, J.D. and Des Marais, D.J. (1999) Exploring for a record of ancient martian life. *J Geophys Res* 104:26977–26995.

Farrand, W.H., Bell, J.F., III, Johnson, J.R., Squyres, S.W., Soderblom, J., and Ming, D.W. (2006) Spectral variability among rocks in visible and near-infrared multispectral Pancam data collected at Gusev Crater: examinations using spectral mixture analysis and related techniques. *J Geophys Res* 111, doi:10.1029/2005JE002495.

Farrand, W.H., Bell, J.F., III, Johnson, J.R., Jolliff, B.L., Knoll, A.H., McLennan, S.M., Squyres, S.W., Calvin, W.M., Grotzinger, J.P., Morris, R.V., Soderblom, J., Thompson, S.D., Watters, W.A., and Yen, A.S. (2007) Visible and near-infrared multispectral analysis of rocks at Meridiani Planum, Mars, by the Mars Exploration Rover Opportunity. *J Geophys Res* 112, doi:10.1029/2006JE002773.

Gaffey, S.J. (1987) Spectral reflectance of carbonate minerals in the visible and near infrared (0.35–2.55 um): anhydrous carbonate minerals. *J Geophys Res* 92:1429–1440.

Gillespie, A.R., Kahle, A.B., and Walker, R.E. (1986) Color enhancement of highly correlated images. Part I. Decorrelation and HSI contrast stretches. *Remote Sens Environ* 20:209–235.

Gorevan, S.P., Myrick, T., Davis, K., Chau, J.J., Bartlett, P., Mukherjee, S., Anderson, R., Squyres, S.W., Arvidson, R.E., Madsen, M.B., Bertelsen, P., Goetz, W., Binau, C.S., and Richter, L. (2003) Rock Abrasion Tool: Mars Exploration Rover mission. *J Geophys Res* 108, doi:10.1029/2003JE002061.

Goryniuk, M.C., Rivard, B.A., and Jones, B. (2004) The reflectance spectra of opal-A (0.5–25 μm) from the Taupo Volcanic Zone: spectra that may identify hydrothermal systems on planetary surfaces. *Geophys Res Lett* 31, doi:10.1029/2004GL021481.

Green, A.A., Berman, M., Switzer, P., and Craig, M.D. (1988) A transformation for ordering multispectral data in terms of image quality with implications for noise removal. *IEEE Trans Geosci Remote Sens* 26:65–74.

Griffith, L.L. and Shock, E.L. (1995) A geochemical model for the formation of hydrothermal carbonates on Mars. *Nature* 377:406–408.

Hamilton, V.E. and Christensen, P.R. (2005) Evidence for extensive, olivine-rich bedrock on Mars. *Geology* 33:433–436.

Hapke, B. (1993) *Introduction to the Theory of Reflectance and Emittance Spectroscopy,* Cambridge University Press, New York.

Haskin, L.A., Wang, A., Jolliff, B.L., McSween, H.Y., Clark, B.C., Des Marais, D.J., McLennan, S.M., Tosca, N.J., Hurowitz, J.A., Farmer, J.D., Yen, A., Squyres, S.W., Arvidson, R.E., Klingelhöfer, G., Schröder, C., de Souza, P.A., Jr., Ming, D.W., Gellert, R., Zipfel, J., Brückner, J., Bell, J.F., III, Herkenhoff, K., Christensen, P.R., Ruff, S., Blaney, D., Gorevan, S., Cabrol, N.A., Crumpler, L., Grant, J., and Soderblom, L. (2005) Water alteration of rocks and soils on Mars at the Spirit rover site in Gusev Crater. *Nature* 436:66–69.

Hecht, M.H., Marshall, J., Pike, W.T., Staufer, U., Blaney, D., Braendlin, D., Gautsch, S., Goetz, W., Hidber, H.R., Keller, H.U., Markiewicz, W.J., Mazer, A., Meloy, T.P., Morookian, J.M., Mogensen, C., Parrat, D., Smith, P., Sykulska, H., Tanner, R.J., Reynolds, R.O., Tonin, A., Vijendran, S., Weilert, M., and Woida, P.M. (2008) Microscopy capabilities of the Microscopy, Electrochemistry, and Conductivity Analyzer. *J Geophys Res* 113, doi:10.1029/2008JE003077.

Herkenhoff, K.E., Squyres, S.W., Bell, J.F., III, Maki, J.N., Arneson, H.M., Bertelsen, P., Brown, D.I., Collins, S.A., Dingizian, A., Elliott, S.T., Goetz, W., Hagerott, E.C., Hayes, A.G., Johnson, M.J., Kirk, R.L., McLennan, S., Morris, R.V., Scherr, L.M., Schwochert, M.A., Shiraishi, L.R., Smith, G.H., Soderblom, L.A., Sohl-Dickstein, J.N., and Wadsworth, M.V. (2003) Athena Microscopic Imager investigation. *J Geophys Res* 108, doi:10.1029/2003JE002076.

Herkenhoff, K.E., Squyres, S.W., Arvidson, R., Bass, D.S., Bell, J.F., III, Bertelsen, P., Ehlmann, B.L., Farrand, W., Gaddis, L., Greeley, R., Grotzinger, J., Hayes, A.G., Hviid, S.F., Johnson, J.R., Jolliff, B., Kinch, K.M., Knoll, A.H., Madsen, M.B., Maki, J.N., McLennan, S.M., McSween, H.Y., Ming, D.W., Rice, J.W., Jr., Richter, L., Sims, M., Smith, P.H., Soderblom, L.A., Spanovich, N., Sullivan, R., Thompson, S., Wdowiak, T., Weitz, C., and Whelley, P. (2004) Evidence from Opportunity's Microscopic Imager for water on Meridiani Planum. *Science* 306:1727–1730.

Herkenhoff, K.E., Squyres, S.W., Anderson, R., Archinal, B.A., Arvidson, R.E., Barrett, J.M., Becker, K.J., Bell, J.F., III, Budney, C., Cabrol, N.A., Chapman, M.G., Cook, D., Ehlmann, B.L., Farmer, J., Franklin, B., Gaddis, L.R., Galuszka, D.M., Garcia, P.A., Hare, T.M., Howington-Kraus, E., Johnson, J.R., Johnson, S., Kinch, K., Kirk, R.L., Lee, E.M., Leff, C., Lemmon, M., Madsen, M.B., Maki, J.N., Mullins, K.F., Redding, B.L., Richter, L., Rosiek, M.R., Sims, M.H., Soderblom, L.A., Spanovich, N., Springer, R., Sucharski, R.M., Sucharski, T., Sullivan, R., Torson, J.M., and Yen, A. (2006) Overview of the Microscopic Imager investigation during Spirit's first 450 sols in Gusev Crater. *J Geophys Res* 111, doi:10.1029/2005JE002574.

Herkenhoff, K.E., Grotzinger, J., Knoll, A.H., McLennan, S.M., Weitz, C., Yingst, A., Anderson, R., Archinal, B.A., Arvidson, R.E., Barrett, J.M., Becker, K.J., Bell, J.F., III, Budney, C., Chapman, M.G., Cook, D., Ehlmann, B., Franklin, B., Gaddis, L.R., Galuszka, D.M., Garcia, P.A., Geissler, P., Hare, T.M., Howington-Kraus, E., Johnson, J.R., Keszthelyi, L., Kirk, R.L., Lanagan, P., Lee, E.M., Leff, C., Maki, J.N., Mullins, K.F., Parker, T.J., Redding, B.L., Rosiek, M.R., Sims, M.H., Soderblom, L.A., Spanovich, N., Springer, R., Squyres, S.W., Stolper, D., Sucharski, R.M., Sucharski, T., and Sullivan, R. (2008) The surface processes recorded by rocks and soils on Meridiani Planum, Mars: Microscopic Imager observations during Opportunity's first three extended missions. *J Geophys Res* 113, doi: 10.1029/2008JE003100.

Herzberg, G. (1945) *Infrared and Raman Spectroscopy,* Von Nostrand Reinhold Company, Inc., New York.

Hunt, G.R. and Salisbury, J.W. (1970) Visible and near infrared spectra of minerals and rocks. I. Silicate minerals. *Modern Geology* 1:283–300.

Hunt, G.R. and Salisbury, J.W. (1971) Visible and near-infrared spectra of minerals and rocks. II. Carbonates. *Modern Geology* 2:23–30.

Hunt, G.R., Salisbury, J.W., and Lenhoff, C.J. (1971) Visible and near infrared spectra of minerals and rocks. IV. Sulphides and sulphates. *Modern Geology* 3:1–14.

Hunt, G.R., Salisbury, J.W., and Lenhoff, C.J. (1973) Visible and near infrared spectra of minerals and rocks. VI. Additional silicates. *Modern Geology* 4:85–106.

Isaacson, P.J. and Pieters, C.M. (2010) Deconvolution of lunar olivine reflectance spectra: implications for remote compositional assessment. *Icarus* 210:8–13.

Keller, H.U., Goetz, W., Hartwig, H., Hviid, S.F., Kramm, R., Markiewicz, W.J., Reynolds, R., Shinohara, C., Smith, P., Tanner, R., Woida, P., Woida, R., Bos, B.J., and Lemmon, M.T. (2008) Phoenix Robotic Arm Camera. *J Geophys Res* 113, doi:10.1029/2007JE003044.

King, T.V.V. and Clark, R.N. (1989) Spectral characteristics of chlorites and Mg-serpentines using high-resolution reflectance spectroscopy. *J Geophys Res* 94:13997–14008.

King, T.V.V. and Ridley, W.I. (1987) Relation of the spectroscopic reflectance of olivine to mineral chemistry and some remote sensing implications. *J Geophys Res* 92:11457–11469.

Kruse, F.A., Lefkoff, A.B., Boardman, J.B., Heidebreicht, K.B., Shapiro, A.T., Barloon, P.J., and Goetz, A.F.H. (1993) The spectral image processing system (SIPS)—interactive visualization and analysis of imaging spectrometer data. *Remote Sens Environ* 44:145–163.

Langevin, Y., Poulet, F., Bibring, J., and Gondet, B. (2005) Sulfates in the north polar region of Mars detected by OMEGA/Mars Express. *Science* 307:1584–1586.

Malin, M.C., Caplinger, M.A., Edgett, K.S., Ghaemi, F.T., Ravine, M.A., Schaffner, J.A., Baker, J.M., Bardis, J.D., DiBiase, D.R., Maki, J.N., Willson, R.G., Bell, J.F., III, Dietrich, W.E., Edwards, L.J., Hallet, B., Herkenhoff, K.E., Heydari, E., Kah, L.C., Lemmon, M.T., Minitti, M.E., Olson, T.S., Parker, T.J., Rowland, S.K., Schieber, J., Sullivan, R.J., Sumner, D.Y., Thomas, P.C., and Yingst, R.A. (2010) The Mars Science Laboratory (MSL) Mast-Mounted Cameras (Mastcams) flight instruments [abstract 1123]. In *41st Lunar and Planetary Science Conference Abstracts,* Lunar and Planetary Institute, Houston.

McSween, H.Y., Jr., Grove, T.L., and Wyatt, M.B. (2003) Constraints on the composition and petrogenesis of the martian crust. *J Geophys Res* 108, doi:10.1029/2003JE002175.

McSween, H.Y., Ruff, S.W., Morris, R.V., Bell, J.F., III, Herkenhoff, K., Gellert, R., Stockstill, K.R., Tornabene, L.L., Squyres, S.W., Crisp, J.A., Christensen, P.R., McCoy, T.J., Mittlefehldt, D.W., and Schmidt, M. (2006a) Alkaline volcanic rocks from the Columbia Hills, Gusev Crater, Mars. *J Geophys Res* 111, doi:10.1029/2006JE002698.

McSween, H.Y., Wyatt, M.B., Gellert, R., Bell, J.F., III, Morris, R.V., Herkenhoff, K.E., Crumpler, L.S., Milam, K.A., Stockstill, K.R., Tornabene, L.L., Arvidson, R.E., Bartlett, P., Blaney, D., Cabrol, N.A., Christensen, P.R., Clark, B.C., Crisp, J.A., Des Marais, D.J., Economou, T., Farmer, J.D., Farrand, W., Ghosh, A., Golombek, M., and Gorevan, S. (2006b) Characterization and petrologic interpretation of olivine-rich basalts at Gusev Crater, Mars. *J Geophys Res* 111, doi:10.1029/2005JE002477.

MEPAG. (2010) *Mars Scientific Goals, Objectives, Investigations, and Priorities,* edited by J.R. Johnson, white paper posted September 2010 by the Mars Exploration Program Analysis Group (MEPAG). Available online at http://mepag.jpl.nasa.gov/reports.cfm

MEPAG MRR-SAG. (2009) *Mars Astrobiology Explorer-Cacher: A Potential Rover Mission for 2018. Final Report from the Mid-Range Rover Science Analysis Group (MRR-SAG),* white paper posted November 2009 by the Mars Exploration Program Analysis Group (MEPAG). Available online at http://mepag.jpl.nasa.gov/reports.cfm

MEPAG ND-SAG. (2008) *Science Priorities for Mars Sample Return,* white paper posted March 2008 by the Mars Exploration Program Analysis Group (MEPAG). Available online at http://mepag.jpl.nasa.gov/reports.cfm

Milliken, R.E., Swayze, G.A., Arvidson, R.E., Bishop, J.L., Clark, R.N., Ehlmann, B.L., Green, R.O., Grotzinger, J.P., Morris, R.V., Murchie, S.L., Mustard, J.F., and Weitz, C. (2008) Opaline silica in young deposits on Mars. *Geology* 36:847–850.

Moore, D.M. and Reynolds, R.C., Jr. (1997) Identification of clay minerals and associated minerals. In *X-ray Diffraction and the Identification and Analysis of Clay Minerals,* Oxford University Press, New York, pp 203–240.

Moore, J.G. (1966) *Rate of Palagonitization of Submarine Basalt Adjacent to Hawaii,* U.S. Geological Survey Professional Paper 550-D:163–171, U.S. Geological Survey, Reston, VA.

Morris, R.V., Lauer, H.V., Jr., Lawson, C.A., Gibson, E.K., Jr., Nace, G.A., and Stewart, C. (1985) Spectral and other physiochemical properties of submicron powders of hematite (α-Fe_2O_3), maghemite (γ-Fe_2O_3), magnetite (Fe_3O_4), goethite (α-FeOOH), and lepidocrocite (γ-FeOOH). *J Geophys Res* 90:3126–3144.

Morris, R.V., Golden, D.C., Bell, J.F., III, Lauer, H.V., Jr., and Adams, J.B. (1993) Pigmenting agents in martian soils: inferences from spectral, Mössbauer, and magnetic properties of nanophase and other iron oxides in Hawaiian palagonitic soil PN-9. *Geochim Cosmochim Acta* 57:4597–4609.

Morris, R.V., Golden, D.C., Bell, J.F., III, Shelfer, T.D., Scheinost, A.C., Hinman, N.W., Furniss, G., Mertzman, S.A., Bishop, J.L., Ming, D.W., Allen, C.C., and Britt, D.T. (2000) Mineralogy, composition, and alteration of Mars Pathfinder rocks and soils: evidence from multispectral, elemental, and magnetic data on terrestrial analogue, SNC meteorite, and Pathfinder samples. *J Geophys Res* 105:1757–1817.

Mottola, S., Arnold, G., Grothues, H.G., Jaumann, R., Michaelis, H., Neukum, G., and Bibring, J.P. (2007) The ROLIS experiment on the Rosetta lander. *Space Sci Rev* 128:241–255.

Mouroulis, P., van Gorp, B., Blaney, D., and Green, R.O. (2008) Reflectance microspectroscopy of natural rock samples in the visible and near infrared. *Appl Spectrosc* 62:1370–1377.

Murchie, S., Arvidson, R., Bedini, P., Beisser, K., Bibring, J.-P., Bishop, J., Boldt, J., Cavender, P., Choo, T., Clancy, R.T., Darlington, E.H., Des Marais, D., Espiritu, R., Fort, D., Green, R., Guinness, E., Hayes, J., Hash, C., Heffernan, K., Hemmler, J., Heyler, G., Humm, D., Hutcheson, J., Izenberg, N., Lee, R., Lees, J., Lohr, D., Malaret, E., Martin, T., McGovern, J.A., McGuire, P., Morris, R., Mustard, J., Pelkey, S., Rhodes, E., Robinson, M., Roush, T., Schaefer, E., Seagrave, G., Seelos, F., Silverglate, P., Slavney, S., Smith, M., Shyong, W.-J., Strohbehn, K., Taylor, H., Thompson, P., Tossman, B., Wirzburger, M., and Wolff, M. (2007) Compact Reconnaissance Imaging Spectrometer for Mars (CRISM) on Mars Reconnaissance Orbiter (MRO). *J Geophys Res* 112, doi:10.1029/2006JE002682.

Murchie, S.L., Mustard, J.F., Ehlmann, B.L., Milliken, R.E., Bishop, J.L., McKeown, N.K., Noe Dobrea, E.Z., Seelos, F.P., Buczkowski, D.L., Wiseman, S.M., Arvidson, R.E., Wray, J.J., Swayze, G., Clark, R.N., Des Marais, D.J., McEwen, A.S., and Bibring, J.P. (2009a) A synthesis of martian aqueous mineralogy after one Mars year of observations from the Mars Reconnaissance Orbiter. *J Geophys Res* 114, doi:10.1029/2009JE003342.

Murchie, S.L., Seelos, F.P., Hash, C.D., Humm, D.C., Malaret, E., McGovern, J.A., Choo, T.H., Seelos, K.D., Buczkowski, D.L., Morgan, M.F., Barnouin- Jha, O.S., Nair, H., Taylor, H.W., Patterson, G.W., Harvel, C.A., Mustard, J.F., Arvidson, R.E., McGuire, P., Smith, M.D., Wolff, M.J., Titus, T.N., Bibring, J.-P., and Poulet, F. (2009b) Compact Reconnaissance Imaging Spectrometer investigation and data set from the Mars Reconnaissance Orbiter's primary science phase. *J Geophys Res* 114, doi:10.1029/2009JE003344.

Murchie, S.L., Mustard, J.F., Bridges, N.T., Smith, M.D., Wolff, M.J., Clancy, R.T., Arvidson, R.E., Ehlmann, B.L., Grant, J.A., Milliken, R.E., Pratt, L.M., Titus, T.N., Becker, K.J., McGovern, J.A., Malaret, E., and Winters, H. (2012) Beyond MRO/CRISM: a high resolution compositional imager for Mars [abstract 1047]. In *International Workshop on Instrumentation for Planetary Missions,* Goddard Space Flight Center, Greenbelt, MD.

Mustard, J.F., Murchie, S.L., Pelkey, S.M., Ehlmann, B.L., Milliken, R.E., Grant, J.A., Bibring, J.P., Poulet, F., Bishop, J., Noe Dobrea, E., Roach, L., Seelos, F., Arvidson, R.E., Wiseman, S., Green, R., Hash, C., Humm, D., Malaret, E., McGovern, J.A., Seelos, K., Clancy, T., Clark, R., Des Marais, D., Izenberg, N., Knudson, A., Langevin, Y., Martin, T., McGuire, P., Morris, R., Robinson, M., Roush, T., Smith, M., Swayze, G., Taylor, H., Titus, T., and Wolff, M. (2008) Hydrated silicate minerals on Mars observed by the CRISM instrument on MRO. *Nature* 454:305–309.

Mustard, J.F., Adler, M., Allwood, A., Bass, D.S., Beaty, D.W., Bell, J.F., III, Brinckerhoff, W.B., Carr, M., Des Marais, D.J., Drake, B., Edgett, K.S., Eigenbrode, J., Elkins-Tanton, L.T., Grant, J.A., Milkovich, S.M., Ming, D., Moore, C., Murchie, S., Onstott, T.C., Ruff, S.W., Sephton, M.A., Steele, A., and Treiman, A. (2013) *Report of the Mars 2020 Science Definition Team,* white paper posted July 2013 by the Mars Exploration Program Analysis Group (MEPAG). Available online at http://mepag.jpl.nasa.gov/reports/MEP/Mars_2020_SDT_Report_Final.pdf.

National Research Council. (2007) *An Astrobiology Strategy for the Exploration of Mars,* The National Academies Press, Washington, DC.

National Research Council. (2011) *Vision and Voyages for Planetary Science in the Decade 2013–2022,* The National Academies Press, Washington, DC.

Nuñez, J.I., Farmer, J.D., Sellar, R.G., and Gardner, P.B. (2009a) Multispectral Microscopic Imager (MMI) with improved spectral range and resolution [abstract 1830]. In *40th Lunar and Planetary Science Conference Abstracts,* Lunar and Planetary Institute, Houston.

Nuñez, J.I., Farmer, J.D., Sellar, R.G., and Allen, C.C. (2009b) Exploring the Moon at the microscale: analysis of Apollo samples with the Multispectral Microscopic Imager (MMI) [abstract P23C-1280]. In *2009 AGU Fall Meeting,* American Geophysical Union, Washington, DC.

Osterloo, M.M., Hamilton, V.E., Bandfield, J.L., Glotch, T.D., Baldridge, A.M., Christensen, P.R., Tornabene, L.L., and Anderson, F.S. (2008) Chloride-bearing materials in the southern highlands of Mars. *Science* 319:1651–1654.

Peacock, M.A. (1926) The petrology of Iceland. Part I, the basic tuffs. *Transactions of the Royal Society of Edinburgh* 55: 51–76.

Pelkey, S. M., Mustard, J.F., Murchie, S., Clancy, R.T., Wolff, M., Smith, M., Milliken, R., Bibring, J.-P., Gendrin, A., Poulet, F., Langevin, Y., and Gondet, B. (2007) CRISM multispectral summary products: Parameterizing mineral diversity on Mars from reflectance. *J Geophys Res* 112, E08S14, doi:10.1029/2006JE002831.

Pieters, C.M. and Hiroi, T. (2004) RELAB (Reflectance Experiment Laboratory): a NASA multiuser spectroscopy facility [abstract 1720]. In *35th Lunar and Planetary Science Conference Abstracts,* Lunar and Planetary Institute, Houston.

Pokrovsky, O.S., Schott, J., Kudryavtzev, D.I., and Dupre, B. (2005) Basalt weathering in Central Siberia under permafrost conditions. *Geochim Cosmochim Acta* 69:5659–5680.

Poulet, F., Mangold, N., Loizeau, D., Bibring, J.P., Langevin, Y., Michalski, J., and Gondet, B. (2008) Abundance of minerals in the phyllosilicate-rich units on Mars. *Astron Astrophys* 487:L41–L44.

Powers, M. (1953) A new roundness scale for sedimentary particles. *J Sediment Petrol* 25:117–119.

Rowan, L.C., Simpson, C.J., and Mars, J.C. (2004) Hyperspectral analysis of the ultramafic complex and adjacent lithologies at Mordor, NT, Australia. *Remote Sens Environ* 91:419–431.

Ruff, S.W., Farmer, J.D., Calvin, W.M., Herkenhoff, K.E., Johnson, J.R., Morris, R.V., Rice, M.S., Arvidson, R.E., Bell, J.F., III, Christensen, P.R., and Squyres, S.W. (2011) Characteristics, distribution, origin, and significance of opaline silica observed by the Spirit rover in Gusev Crater, Mars. *J Geophys Res* 116, doi:10.1029/2010JE003767.

Sellar, R.G., Farmer, J.D., Kieta, A., and Huang, J. (2006) Multispectral microimager for astrobiology. *Proc SPIE* 6309, doi:10.1117/12.682272.

Sellar, R.G., Farmer, J.D., Robinson, M.S., and Nuñez, J.I. (2008) Multispectral hand lens and field microscope [abstract 4075]. In *Joint Annual Meeting of LEAG-ICEUM-SRR,* Lunar and Planetary Institute, Houston.

Sherman, D.M., Burns, R.G., and Burns, V.M. (1982) Spectral characteristics of the iron oxides with application to the martian bright region mineralogy. *J Geophys Res* 87:10169–10180.

Smith, P.H., Tomasko, M.G., Britt, D., Crowe, D.G., Reid, R., Keller, H.U., Thomas, N., Gliem, F., Rueffer, P., Sullivan, R., Greeley, R., Knudsen, J.M., Madsen, M.B., Gunnlaugsson, H.P., Hviid, S.F., Goetz, W., Soderblom, L.A., Gaddis, L., and Kirk, R. (1997) The imager for Mars Pathfinder experiment. *J Geophys Res* 102:4003–4025.

Smith, P.H., Reynolds, R., Weinberg, J., Friedman, T., Lemmon, M.T., Tanner, R., Reid, R.J., Marcialis, R.L., Bos, B.J., Oquest, C., Keller, H.U., Markiewicz, W.J., Kramm, R., Gliem, F., and Rueffer, P. (2001) The MVACS Surface Stereo Imager on Mars Polar Lander. *J Geophys Res* 106:17589–17607.

Smith, P.H., Tamppari, L., Arvidson, R.E., Bass, D., Blaney, D., Boynton, W., Carswell, A., Catling, D., Clark, B., Duck, T., DeJong, E., Fisher, D., Goetz, W., Gunnlaugsson, P., Hecht, M., Hipkin, V., Hoffman, J., Hviid, S., Keller, H., Kounaves, S., Lange, C.F., Lemmon, M., Madsen, M., Malin, M., Markiewicz, W., Marshall, J., McKay, C., Mellon, M., Michelangeli, D., Ming, D., Morris, R., Renno, N., Pike, W.T., Staufer, U., Stoker, C., Taylor, P., Whiteway, J., Young, S., and Zent, A. (2008) Introduction to special section on the Phoenix mission: landing site characterization experiments, mission overviews, and expected science. *J Geophys Res* 113, doi:10.1029/2008JE003083.

Squyres, S. W., Grotzinger, J.P., Arvidson, R.E., Bell, J.F., III, Calvin, W., Christensen, P.R., Clark, B.C., Crisp, J.A., Farrand, W.H., Herkenhoff, K.E., Johnson, J.R., Klingelhofer, G., Knoll, A.H., McLennan, S.M., McSween Jr., H.Y., Morris, R.V., Rice Jr., J.W., Rieder, R., and Soderblom, L.A. (2004) In-situ evidence for an ancient aqueous environment at Meridiani Planum, Mars. *Science* 306:1709–1714.

Squyres, S.W., Arvidson, R.E., Ruff, S., Gellert, R., Morris, R.V., Ming, D.W., Crumpler, L., Farmer, J.D., Des Marais, D.J., Yen, A., McLennan, S.M., Calvin, W., Bell, J.F., Clark, B.C., Wang, A., McCoy, T.J., Schmidt, M.E., and de Souza, P.A. (2008) Detection of silica-rich deposits on Mars. *Science* 320:1063–1067.

Sunshine, J.M. and Pieters, C.M. (1998) Determining the composition of olivine from reflectance spectroscopy. *J Geophys Res* 103:13675–13688.

Swayze, G.A., Clark, R.N., Goetz, A.F.H., Chrien, T.G., and Gorelick, N.S. (2003) Effects of spectrometer bandpass, sampling, and signal-to-noise ratio on spectral identification using the Tetracorder algorithm. *J Geophys Res* 108, doi:10.1029/2002JE001975.

Thorseth, I.H., Furnes, H., and Tumyr, O. (1991) A textural and chemical study of Icelandic palagonite of varied composition and its bearing on the mechanism of the glass-palagonite transformation. *Geochim Cosmochim Acta* 55:731–749.

Warner, N.H. and Farmer, J.D. (2010) Subglacial hydrothermal alteration minerals in Jökulhlaup deposits of southern Iceland, with implications for detecting past or present habitable environments on Mars. *Astrobiology* 10:523–547.

Weitz, C.M., Farrand, W.H., Johnson, J.R., Fleischer, I., Schröder, C., Yingst, A., Jolliff, B., Gellert, R., Bell, J., Herkenhoff, K.E., Klingelhöfer, G., Cohen, B., Calvin, W., Rutherford, M., and Ashley, J. (2010) Visible and near-infrared multispectral analysis of geochemically measured rock fragments at the Opportunity landing site in Meridiani Planum. *J Geophys Res* 115, doi:10.1029/2010JE003660.

Address correspondence to:
Jorge I. Núñez, PhD
Johns Hopkins University
Applied Physics Laboratory
11100 Johns Hopkins Road
Laurel, MD 20723-6099

E-mail: jorge.nunez@jhuapl.edu

Submitted 23 July 2013
Accepted 15 January 2014

(*Appendix follows*→)

Table A1. Source and Full Sample Identifier for the Library Spectra Shown in Figures 4–5, 7, 9, 13, 15–16, 20, and 22

Label in figure	*Source*	*Source sample ID*	*Notes*
Figures 4A and 5A			
Augite	Clark *et al.*, 2007	Augite NMNH120049	Figure 5 spectra convolved to MMI bandpasses.
Diopside	Clark *et al.*, 2007	Diopside NMNHR18685	Figure 5 spectra convolved to MMI bandpasses.
Hypersthene	Clark *et al.*, 2007	Hypersthene NMNHC2368	Figure 5 spectra convolved to MMI bandpasses.
Olivine Fo11	Clark *et al.*, 2007	Olivine KI3005 Fo11	Figure 5 spectra convolved to MMI bandpasses.
Olivine Fo89	Clark *et al.*, 2007	Olivine GDS70.b Fo89	Figure 5 spectra convolved to MMI bandpasses.
Figures 4B and 5B			
Ferrihydrite	Clark *et al.*, 2007	Ferrihydrite GDS75	Figure 5 spectra convolved to MMI bandpasses.
Goethite	Clark *et al.*, 2007	Goethite WS220	Figure 5 spectra convolved to MMI bandpasses.
Hematite	Clark *et al.*, 2007	Hematite GDS27	Figure 5 spectra convolved to MMI bandpasses.
Jarosite	Clark *et al.*, 2007	Jarosite GDS24 Na	Figure 5 spectra convolved to MMI bandpasses.
Nontronite	Clark *et al.*, 2007	Nontronite NG-1.a	Figure 5 spectra convolved to MMI bandpasses.
Figures 4C and 5C			
Kaolinite	Clark *et al.*, 2007	Kaolinite KGa-1 (wxl)	Figure 5 spectra convolved to MMI bandpasses.
Montmorillonite	Clark *et al.*, 2007	Montmorillonite STx-1	Figure 5 spectra convolved to MMI bandpasses.
Nontronite	Clark *et al.*, 2007	Nontronite NG-1.a	Figure 5 spectra convolved to MMI bandpasses.
Saponite	Clark *et al.*, 2007	Saponite SapCa-1	Figure 5 spectra convolved to MMI bandpasses.
Figures 4D and 5D			
Analcime	Clark *et al.*, 2007	Analcime GDS1 Zeolite	Figure 5 spectra convolved to MMI bandpasses.
Illite	Clark *et al.*, 2007	Illite IMt-1.a	Figure 5 spectra convolved to MMI bandpasses.
Muscovite	Clark *et al.*, 2007	Muscovite GDS111	Figure 5 spectra convolved to MMI bandpasses
Opal	Clark *et al.*, 2007	Opal TM8896 (Hyalite)	Figure 5 spectra convolved to MMI bandpasses.
Figures 4E and 5E			
Alunite	Clark *et al.*, 2007	Alunite AL706 Na	Figure 5 spectra convolved to MMI bandpasses.
Epsomite	Clark *et al.*, 2007	Epsomite GDS149	Figure 5 spectra convolved to MMI bandpasses.
Gypsum	Clark *et al.*, 2007	Gypsum HS333.3B (Selenite)	Figure 5 spectra convolved to MMI bandpasses.
Jarosite	Clark *et al.*, 2007	Jarosite GDS24 Na	Figure 5 spectra convolved to MMI bandpasses.
Figures 4F and 5F			
Calcite	Baldridge *et al.*, 2009	Calcite C-3D	Figure 5 spectra convolved to MMI bandpasses.
Dolomite	Baldridge *et al.*, 2009	Dolomite C-5C	Figure 5 spectra convolved to MMI bandpasses.
Magnesite	Baldridge *et al.*, 2009	Magnesite C-6A	Figure 5 spectra convolved to MMI bandpasses.
Siderite	Baldridge *et al.*, 2009	Siderite C-9A	Figure 5 spectra convolved to MMI bandpasses.
Figures 7C, 7D, 9C, and 9D			
Anorthite	Clark *et al.*, 2007	Anorthite HS201.3B	Figure 7 spectra convolved to MMI bandpasses.
Augite	Clark *et al.*, 2007	Augite NMNH120049	Figure 7 spectra convolved to MMI bandpasses.
Basalt fresh	Clark *et al.*, 2007	Basalt_fresh BR93-46B	Figure 7 spectra convolved to MMI bandpasses.
Bytownite	Clark *et al.*, 2007	Bytownite HS105.3B	Figure 7 spectra convolved to MMI bandpasses.
Diopside	Clark *et al.*, 2007	Diopside NMNHR18685	Figure 7 spectra convolved to MMI bandpasses.
Olivine Fo29	Clark *et al.*, 2007	Olivine KI3291 Fo29 < 60 um	Figure 7 spectra convolved to MMI bandpasses.
Olivine Fo51	Clark *et al.*, 2007	Olivine KI3188 Fo51 < 60 um	Figure 7 spectra convolved to MMI bandpasses.
Olivine Fo91	Clark *et al.*, 2007	Olivine GDS71.a Fo91 65 um	Figure 7 spectra convolved to MMI bandpasses.
Figures 13C and 13D			
Ferrihydrite	Clark *et al.*, 2007	Ferrihydrite GDS75 Syn	Spectra convolved to MMI bandpasses.
Goethite WS220	Clark *et al.*, 2007	Goethite WS220	Spectra convolved to MMI bandpasses.
Goethite WS222	Clark *et al.*, 2007	Goethite WS222 Medium Gr.	Spectra convolved to MMI bandpasses.
Hematite	Clark *et al.*, 2007	Hematite GDS27	Spectra convolved to MMI bandpasses.
Lepidocrocite	Clark *et al.*, 2007	Lepidocrocite GDS80 (Syn)	Spectra convolved to MMI bandpasses.
Limonite	Clark *et al.*, 2007	Limonite HS41.3	Spectra convolved to MMI bandpasses.
Rhyolite	Baldridge *et al.*, 2009	Rhyolite (Felsic Rhyolite.H1)	Spectra convolved to MMI bandpasses.
Figures 13E and 13F			
Calcite	Clark *et al.*, 2007	Calcite HS48.3B	Spectra convolved to MMI bandpasses.
Clinoptilolite	Clark *et al.*, 2007	Clinoptilolite GDS152	Spectra convolved to MMI bandpasses.

(*continued*)

Table A1. (Continued)

Label in figure	*Source*	*Source sample ID*	*Notes*
		Zeolit	
Erionite	RELAB	Erionite ZE-EAC-025 C1ZE25	Spectra convolved to MMI bandpasses.
Gypsum	Clark *et al.,* 2007	Gypsum HS333.3B (Selenite)	Spectra convolved to MMI bandpasses.
Kaolinite	Clark *et al.,* 2007	Kaolinite CM7	Spectra convolved to MMI bandpasses.
Montmorillonite	Clark *et al.,* 2007	Montmorillonite CM26	Spectra convolved to MMI bandpasses.
Opal	Clark *et al.,* 2007	Opal TM8896 (Hyalite)	Spectra convolved to MMI bandpasses.
Quartz	Clark *et al.,* 2007	Quartz HS32.4B	Spectra convolved to MMI bandpasses.
Figures 15C and 15D			
Goethite	Clark *et al.,* 2007	Goethite WS222 Medium Gr.	
Hematite	Clark *et al.,* 2007	Hematite GDS27	
Lepidocrosite	Clark *et al.,* 2007	Lepidocrosite GDS80 (Syn)	
Rhyolite	Baldridge *et al.,* 2009	Rhyolite (Felsic Rhyolite.H1)	
Figures 15E, 15F, 16C, and 16D			
Calcite	Clark *et al.,* 2007	Calcite WS272	
Celadonite	RELAB	Celadonite JB-JLB-727 C1JB727	
Clinochlore	Clark *et al.,* 2007	Clinochlore_Fe SC-CCa-1.c	
Hectorite	Clark *et al.,* 2007	Hectorite SHCa-1	
Montmorillonite	Clark *et al.,* 2007	Montmorillonite SAz-1	
Nontronite	Clark *et al.,* 2007	Nontronite NG-1.a	
Opal	Clark *et al.,* 2007	Opal TM8896 (Hyalite)	
Saponite	Clark *et al.,* 2007	Saponite SapCa-1	
Figures 20C and 20D			
Augite	Clark *et al.,* 2007	Augite NMNH120049	Spectra convolved to MMI bandpasses.
Basalt fresh	Clark *et al.,* 2007	Basalt_fresh BR93-46B	Spectra convolved to MMI bandpasses.
Basalt weathered	Clark *et al.,* 2007	Basalt_weathered BR93-43	Spectra convolved to MMI bandpasses.
Diopside	Clark *et al.,* 2007	Diopside NMNHR18685	Spectra convolved to MMI bandpasses.
Ferrihydrite	Clark *et al.,* 2007	Ferrihydrite JB-CMP-045 C1JB45	Spectra convolved to MMI bandpasses.
Nontronite NG-1	Clark *et al.,* 2007	Nontronite NG-1.b	Spectra convolved to MMI bandpasses.
Nontronite SWa-1	Clark *et al.,* 2007	Nontronite SWa-1.a	Spectra convolved to MMI bandpasses.
Figures 20E and 20F			
Chabazite	Clark *et al.,* 2007	Chabazite HS193.3B	Spectra convolved to MMI bandpasses.
Clinoptilolite	Clark *et al.,* 2007	Clinoptilolite GDS152 Zeolit	Spectra convolved to MMI bandpasses.
Gypsum	Clark *et al.,* 2007	Gypsum HS333.3B (Selenite)	Spectra convolved to MMI bandpasses.
Kieserite	RELAB	Kieserite JB-JLB-734 C1JB734	Spectra convolved to MMI bandpasses.
Montmorillonite	Clark *et al.,* 2007	Montmorillonite CM26	Spectra convolved to MMI bandpasses.
Natrolite	Clark *et al.,* 2007	Natrolite NMNH83380 Zeolite	Spectra convolved to MMI bandpasses.
Opal 1	Clark *et al.,* 2007	Opal TM8896 (Hyalite)	Spectra convolved to MMI bandpasses.
Opal 2	Clark *et al.,* 2007	Opal WS732	Spectra convolved to MMI bandpasses.
Figures 22C and 22D			
Anorthite	Clark *et al.,* 2007	Anorthite HS201.3B	
Augite	Clark *et al.,* 2007	Augite NMNH120049	
Basalt fresh	Clark *et al.,* 2007	Basalt_fresh BR93-46B	
Basalt weathered	Clark *et al.,* 2007	Basalt_weathered BR93-43	
Diopside	Clark *et al.,* 2007	Diopside NMNHR18685	
Nontronite NG-1	Clark *et al.,* 2007	Nontronite NG-1.a	
Olivine Fo29	Clark *et al.,* 2007	Olivine KI3291 Fo29 < 60 um	
Olivine Fo51	Clark *et al.,* 2007	Olivine KI3188 Fo51 < 60 um	